Design of Biomaterials Towards Endogenous Bone Regeneration

by

Mengqian Liu

Department of Mechanical Engineering and Materials Science
Duke University

Date:_____
Approved:

_____
Kenneth A. Gall, Advisor

_____
John E. Dolbow

_____
Jennifer L. West

_____
Stefan Zauscher

Dissertation submitted in partial fulfillment of
the requirements for the degree of Doctor
of Philosophy in the Department of
Mechanical Engineering and Materials Science in the Graduate School
of Duke University

2020

ABSTRACT

Design of Biomaterials Towards Endogenous Bone Regeneration

by

Mengqian Liu

Department of Mechanical Engineering and Materials Science
Duke University

Date:_____
Approved:

_____
Kenneth A. Gall, Advisor

_____
John E. Dolbow

_____
Jennifer L. West

_____
Stefan Zauscher

An abstract of a dissertation submitted in partial
fulfillment of the requirements for the degree
of Doctor of Philosophy in the Department of
Mechanical Engineering and Materials Science in the Graduate School of
Duke University

2020

Abstract

Bone grafting is one of the most commonly used surgical methods to augment bone regeneration in orthopedic procedure. While using natural bones, such as autograft and allograft are considered as the gold standard techniques, they suffer from numerous drawbacks including scarcity, donor site complications, and potential disease transmission. To overcome these limitations, mineralized poly (ethylene glycol) diacrylate-co-N-acryloyl 6-aminocaproic acid (PEGDA-co-A6ACA) composed of an organic phase and an inorganic, biomineralized phase that recapitulates certain aspects of dynamic mineral environment of native has been developed. The real-world application this biomineralized material in treating bone defects *in vivo* depends upon a myriad of parameters including scaffold structural parameters (e.g. pore size), mechanical properties (e.g. strength and toughness), and host environments (e.g. age of the recipient). In this dissertation, I explored these biomaterial and biological parameters for biomaterials mediated bone regeneration through leveraging endogenous healing mechanism.

First of all, I evaluated the potential of mineralized biomaterials to induce bone repair of a critical-sized cranial defect in the absence of exogenous cells and growth factors. I demonstrated that the mineralized biomaterial alone can support complete bone formation within critical-sized bone defects through recruitment of endogenous

cells and neo-bone tissue formation in mice. By providing a bone-specific mineral environment, these biomaterials induce osteogenic commitment of recruited host progenitor cells and support the maintenance of cells relevant for the formation and function of bone tissues, including vascularization of the implant during repair. Based on these findings, I further investigated the effect of the scaffold pore size on *in vivo* ectopic bone formation. Biomineralized PEGDA-co-A6ACA hydrogels were made to have an interconnected macroporous network with different pore size ranges (45-53 μm, 90-106 μm, 160-180 μm, 212-250 μm or 300-355 μm) and similar overall porosity between 65% to 70%. Using these scaffolds, I evaluated their abilities to promote ectopic bone formation upon subcutaneous implantation in wild-type mice as a function of time. I found that scaffolds with pore sizes larger than 100 μm showed similar bone formation abilities, whereas in scaffolds with pore sizes 45-53 μm, cell infiltration only happened at the peripheral region of the scaffolds. Results from this study revealed that pore size of the scaffolds had a prominent influence on the extent of cell infiltration and bone ingrowth.

While such biomaterial-mediated *in situ* tissue engineering is highly attractive, success of this approach relies largely on the regenerative potential of the recruited endogenous cells, which is anticipated to vary with age of the host. To this end, I investigated the effect of the age of the host on mineralized biomaterial-mediated bone tissue repair using critical-sized cranial defects as a model system. Mice of varying ages,

1-month-old (juvenile), 2-month-old (young-adult), 6-month-old (middle-aged), and 14-month-old (elderly), were used as recipients. I showed that the biomineralized scaffolds support bone tissue formation by recruiting endogenous cells for all groups albeit with differences in an age-related manner. The age of the recipient mice had a significant influence on the quantity and quality of the neo-bone tissues characterized in terms of bone mineral deposition and bone tissue-specific markers, where delayed bone formation and decreased quantity of neo-bone tissue formation were observed in older mice.

The real-world applications of the biomineralized materials for aiding bone tissue regeneration are greatly limited by the lack of mechanical strength and toughness of the materials. To enhance the mechanical property of the biomineralized scaffold, I further proposed a double network (DN) hydrogel system with an asymmetric network structure, where the first network is tightly cross-linked by A6ACA with crosslinker N, N'-Methylenebisacrylamide (bisacrylamide), and the second network is loosely crosslinked PEGDA. The effects of bisacrylamide crosslinker concentration (2 mol.%, 4 mol.% and 6 mol.%), and molecular weight (Mn: 3.4 kDa, 6 kDa, 10 kDa, and 20 kDa) of 20 w/v % PEGDA on mechanical properties of the resultant DN-hydrogels were investigated and compared to those of single network (SN) hydrogels of the same composition. Findings from this study showed that increase in crosslinker concentration of the first network was correlated with lower ultimate compressive strain, higher

compressive strength, toughness and elastic modulus. Furthermore, DN-hydrogels prepared in this work displayed swelling ratios ranging from 569 ± 20% to 1948 ± 12%. Among all compositions, DN-hydrogel with 6 mol.% bisacrylamide and PEGDA 10 kDa demonstrated the highest compressive strength (3.47 ± 0.35 MPa), highest toughness (0.60 ± 0.03 MJ/m^3), and elastic modulus (1.04 ± 0.09 MPa). Using this composition, porous DN-hydrogels with interconnected pore architecture were fabricated through polymethylmethacrylate (PMMA) bead leaching method. Resultant porous hydrogels demonstrated potent biomineralization capabilities, and the matrix-bounded CaP minerals were able to undergo dissolutions. Given the high strength and biomineralization capacity, DN-hydrogels reported here could be useful for developments of tissue engineering scaffolds for bone tissue regenerations.

Overall, this dissertation explores different biomaterial designs and biological factors in biomaterial-mediated *in vivo* bone tissue repair, providing materials insights that are useful to researchers and engineers in designs of biomaterials to leverage endogenous healing mechanism for tissue regeneration and repair.

Dedication

To the fond and loving memory of my grandmother.

Contents

Abstract iv

Dedication viii

List of Tables xiv

List of Figures xv

1. Chapter 1: Introduction 1

1.1 Bone Tissue: a dynamic and highly mineralized tissue with hierarchical structure 1

1.2 Biomaterials for Bone Tissue Repair 4

1.3 Biomineralized Materials for Bone Tissue Repair 6

1.4 Overview 8

1.4.1 Chapter 2 8

1.4.2 Chapter 3 9

1.4.3 Chapter 4 9

1.4.4 Chapter 5 10

1.4.5 Chapter 6 10

2. Chapter 2: Design of Biomaterials to Guide Cell Behaviors in Regenerative Engineering Literature Review 1

2.1 Design of Biomaterials to Guide Stem Cell Behaviors 1

2.1.1 Introduction 1

2.1.2 Design of Biomaterials to Control Cell Functions 3

2.1.2.1 Functionalizing synthetic materials with cell-adhesive moieties 4

2.1.2.2 Biomaterial Design to Regulate Growth Factor Signaling.....5

2.1.2.3 Biomaterial-Chemistry Mediated Cellular Responses 7

2.1.3 Tuning Matrix Stiffness to Guide Cell Behavior.....10

2.1.4 Designing Synthetic Substrate to Provide Topographical Cues 13

3. Chapter 3: Investigate Effects of Mineralized Materials to Support *in vivo* Bone Tissue Formation.....17

3.1 Introduction 17

3.2 Materials and Method 21

3.2.1 Graft synthesis and mineralization 21

3.2.2 Calcium Phosphate Assay 23

3.2.3 Scanning electron microscopy (SEM) and energy dispersive spectra (EDS) 24

3.2.4 Surgical procedures and biomaterial implantation 24

3.2.5 Mercury intrusion porosimetry (MIP).....26

3.2.6 Micro-computed tomography (μCT).....26

3.2.7 Histology and immunohistological staining 27

3.2.8 Mechanical testing 30

3.3 Results.....31

3.3.1 Characterization of Macroporous Hydrogels 31

3.3.2 Mechanical properties 33

3.3.3 *In vivo* hard tissue formation 37

3.3.4 Histological assessment of bone formation and cell recruitment 41

3.3.5 Vascularization of implanted grafts 45

3.3.6 Histology and Immunostaining 48

3.4 Discussions 54

3.5 Conclusions 59

4. Chapter 4: Elucidate Effects of Host Age on Endogenous Cell Mediated Bone Tissue Formation 61

4.1 Introduction 61

4.2 Materials and Methods 63

4.2.1 Graft synthesis and mineralization 63

4.2.2 Calcium and phosphate assays 64

4.2.3 Scanning electron microscopy (SEM) and energy dispersive spectra (EDS) 65

4.2.4 Surgical procedures and biomaterial implantation 66

4.2.5 Micro-computed tomography (μCT) 67

4.2.6 Histology and immunohistological staining 67

4.2.7 Statistical Methods 70

4.3 Results 71

4.3.1 Fabrication and Characterization of mineralized biomaterials 71

4.3.2 Evaluation of hard tissue formation 73

4.3.3 Bone tissue formation 76

4.3.4 Vascularization and Recruitment of cells 83

4.4 Discussion 88

4.5 Conclusion 92

5. Chapter 5: Develop a Tough Hydrogel Network to Enhance the Mechanical Property of Mineralized Scaffolds 94

5.1 Introduction 94

5.2 Materials and Methods.....97

5.2.1 Material synthesis and characterization 97

5.2.2 Single and double-network hydrogel synthesis 99

5.2.3 Porous hydrogel Synthesis and Mineralization of Hydrogels 100

5.2.4 Scanning electron microscopy (SEM).....102

5.2.5 Mechanical testing 102

5.2.6 Calcium and phosphate assays 102

5.2.7 Swelling ratio measurement.....104

5.2.8 Statistical analysis 104

5.3 Results and Discussions 104

5.3.1 Mechanical testing 104

5.3.2 Swelling ratios of DN-hydrogels 109

5.3.3 Surface topography and mineral dissolution kinetics 111

5.3.4 Mechanical properties of (non)mineralized (non)porous DN/SN- hydrogels 114

5.4 Conclusions 116

6. Chapter 6: Future Directions 118

6.1 Evaluation of biomineralized scaffolds 119

6.2 Investigation of cellular mechanisms underlying age-related osteogenic differentiation and tissue formation.....120

6.3 Development of degradable biomineralized scaffolds.....122

6.4 Development of injectable biomineralized scaffolds 123

7. Chapter 7: Conclusions 125

References 127

Biography 163

List of Tables

Table 1: Polymer network compositions of DN-hydrogels 100

Table 2: Summary of mechanical property of SN and DN-hydrogel of $PEGDA_{10K}$ and 6 mol.% bisacrylamide 106

List of Figures

Figure 1: Hierarchical organization of bone from macro-to the nanoscale. 2

Figure 2: Gene expression profiles of aggrecan, CBFa-1, PPAR® for hMSCs seeded on surfaces modified with various functional groups. 9

Figure 3: Tissue Stiffness and modulus of poly(acrylamide) substrates influences lineage-specific differentiation. 12

Figure 4: Biomineralized matrix characterization. 32

Figure 5: SEM/EDS and Calcium Phosphate Dissolution of mineralized PEGDA-co-A6ACA macroporous hydrogel. 33

Figure 6: Stress-strain curves of mineralized nonporous and porous (Groups 1-5) scaffolds. 34

Figure 7: Calcium Phosphate content and dissolution and mercury intrusion porosimetry (MIP) measurement of the PEGDA-co-A6ACA scaffold. 36

Figure 8: Calcified bone tissue formation within critical-sized cranial defects. 37

Figure 9: Growth images and Micro-computed tomography (μCT) images and quantification of excised scaffolds. 40

Figure 10: Morphological assessment of bone formation within critical-sized cranial defects. 42

Figure 11: H&E staining of cranial sections following 2 weeks of implantation. 43

Figure 12: Morphological assessment of bone formation within critical-sized cranial defects. 45

Figure 13: Vascularization of the defect following 2 weeks of implantation. 46

Figure 14: Vascularization of the defect following 8 weeks of implantation. 47

Figure 15: Vascularization of mineralized scaffold 2- and 8-week post-implantation. 48

Figure 16: Bone-specific markers in newly formed tissue within cranial defects at 8 weeks after implantation. 50

Figure 17: Bone specific marker evaluation at 2 weeks after implantation. 51

Figure 18: Bone-specific markers in newly formed tissue within cranial defects 8-week post-implantation. 53

Figure 19: SEM/EDS and calcium phosphate dissolution of mineralized PEGDA-co-A6ACA macroporous hydrogel.....72

Figure 20: Calcified hard tissue formation within critical-sized cranial defects. 74

Figure 21: Histological assessment of the sham group. 77

Figure 22: Morphological assessment of bone formation within critical-sized cranial defects at 8 weeks post-implantation.....79

Figure 23: Bone-specific markers in newly formed tissue within cranial defects of biomineralized scaffold-treated groups at 8 weeks post-implantation. 80

Figure 24: Bone-specific markers in newly formed tissue within cranial defects of biomineralized scaffold-treated groups at 2 weeks post-implantation. 82

Figure 25: Vascularization of biomineralized scaffolds showing red blood cells. 85

Figure 26: Vascularization of cranial defects treated with biomineralized scaffolds at 2 weeks post-implantation 86

Figure 27: Vascularization of cranial defects treated with biomineralized scaffolds at 8 weeks post-implantation. 87

Figure 28: Schematics of single and double-network hydrogel synthesis. 99

Figure 29: Summary mechanical property of SN and DN-hydrogels based on compositions.....105

Figure 30: Stress-strain curve of SN and DN-hydrogel with 6 mol. % Bisacrylamide and $PEGDA_{10k}$ 107

Figure 31: Swelling ratios of DN-hydrogels of varying compositions.....109

Figure 32: SEM images of non-mineralize/mineralized porous DN-hydrogels. 111

Figure 33: Mineral contents and dissolution kinetics of A6ACA-PEGDA DN-hydrogels. 112

Figure 34: Mechanical properties of (non)mineralized (non)porous DN and SN hydrogels.....115

1. Chapter 1: Introduction

Bone and its associated diseases remain a considerable clinical challenge worldwide as they account for half of all chronic diseases in people over 50 years old [1,2]. Among these bone diseases, severe bone defects due to trauma, bone tumor resection, congenital diseases, degenerative and inflammatory conditions often require surgical interventions such as bone grafting to promote bone healing and repair.

Bone grafting is widely used to augment bone regeneration in orthopedic procedures [3], where over 2 million bone grafting procedures were performed annually worldwide [4]. Unfortunately, however, there are no ideal solutions for bone grafts available because of the unmet reparative potential of bone defects and the limited efficacy of treatment options. The research present in this dissertation aims to demonstrate a novel biomaterial-based tissue engineering strategy for bone grafting and reconstruction.

1.1 Bone Tissue: a dynamic and highly mineralized tissue with hierarchical structure

Bone is a highly mineralized tissue with hierarchical structures. It is mainly composed of two phases: inorganic calcium phosphate mineral phase and organic collagen substrate (osteoid). The inorganic mineralized phase of the bone provides support for its mechanical and chemical functions. The organic phase, consists of mainly type I collagen fibrils and other non-collagenous proteins including osteocalcin and bone

sialoproteins, provides essential cellular functions such as mediating bone tissue mineralization[5,6], and mechanical functions such as supporting structural integrity of bones.

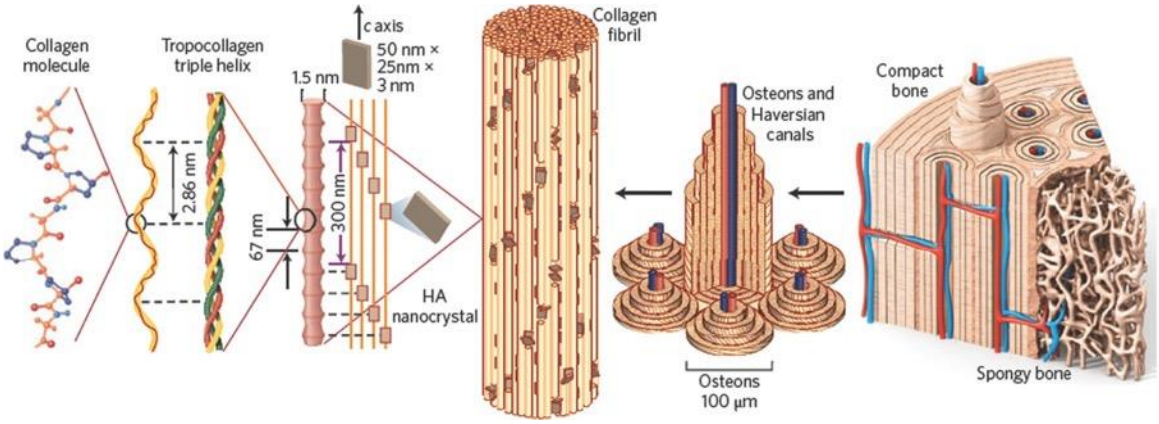

Figure 1: Hierarchical organization of bone from macro-to the nanoscale. Reproduced with permission from[7]. Copyright 2015, Nature Publishing Group.

Bone is hierarchically structured in a variety of scales ranging from nanoscopic to macroscopic (Figure 1), and all of these scales play crucial roles in mechanical and biological functions of bones. Figure 1 illustrates different bone components at these scales [7]. At nanoscopic level, carbonate apatite nanocrystals (plate-shaped, tens of nm in length and width 1.5-4 nm in thickness) deposit periodically on the gap zone of collagen fibrils and other non-collagenous proteins.[5,6] The mineralized collagen fibrils (~300 nm in length and 1.5 nm in diameter) further assemble into a 3-dimensional heterogenous and anisotropic structure which makes up the lamella of bone. The lamella structure (several μm in thickness) is considered as the basic building block of the macroscopic structure of

bone. The hierarchical structure and precise arrangements of the inorganic and organic phases give rise to the unique mechanical properties of the bone. Due to the heterogenous nanoscopic arrangement of collage fibrils and apatite crystal mentioned above, nanomechanical heterogeneities were produced and ultimately endow bone with high energy dissipation and resistance to fracture.

Bone is a highly dynamic tissue that undergoes constant remodeling process of being simultaneously destroyed and reconstructed. This dynamism and homeostasis of bone are maintained through coordination of several bone cells including osteoblasts, osteocytes, and osteoclasts. Originated from mesenchymal progenitor cells, osteoblasts secrete organic collagen matrix, and into this matrix hydroxyapatite mineral was deposited through biomineralization process. As bone tissue matures, this structure further organized into a more sophisticated composite through a series of cellular activities [8]. After the completion of bone osteogenesis, osteoblasts embedded in the mineralized matrix transform into osteocytes and reside within the matrix. Osteocytes, as the most abundant cell in mature bone, maintain bone mineral environments through enzymatic regulations. In contrast to bones-forming cell, osteoclast, multinucleated cells originated from mononuclear progenitors, degrade bones by secretion of proteolytic enzymes (e.g., cathepsin K) and acid to hydrolyze bone components during bone remodeling [9].

1.2 Biomaterials for Bone Tissue Repair

Unlike most organs in human body, bone has great capacity to regenerate and repair itself upon injury or damage. However, this ability may be impaired depending on the severity of bone defects. For instance, critical-sized bone defects caused by trauma, tumor excision or chronic diseases may often require surgical interventions and one of them being bone grafting.

Materials that are osteoinductive and osteoconductive are usually regarded as excellent candidates for bone grafts. Osteoinduction refers to the ability of a material to recruit osteoprogenitor cells from host to the site of defect and promote the subsequent cell differentiation to form bone tissues. On the other hand, osteoconduction is the ability of a material to support osteoblasts for continuous bone ingrowth across a scaffold. So far, native bone tissues and their derivatives have been touted as the most effective strategies to treat bone defects because of their inherent abilities to provide many cues relevant for bone regeneration. This led to the developments of several commercially available natural bone derived products, including ALLOPURE®, AlloWedge®, alloOss® and CANCELLO-PURETM Wedges. Although nature bone derived grafts are considered as ideal candidates to augment bone healing and tissue repair, they suffer from various drawbacks such as limited sources, donor site complications, and potential for disease transmission [10-12].

To overcome these limitations, tissue engineering strategies of using biomaterials in combination with osteoinductive molecules and/or exogenous cells, have been widely studied [13,14]. Although conventional tissue engineering strategies that use biomaterials and exogenous cells are promising, activating endogenous cells to regenerate the compromised bone tissue or assist bone tissue repair are more clinically attractive. Towards this, potent osteoinductive biomolecules, such as bone morphogenetic proteins (BMPs), have been extensively used. In fact, BMP-2 and BMP-7 (or osteogenic protein-1, BMP-7) are approved for clinical use in treating non-union bone fractures and spinal fusion[15]. While BMPs are very effective in promoting bone tissue regeneration, their widespread clinical use is hampered by various side effects such as inflammatory complications, osteolysis and unwanted ectopic bone formation[16-18].

Another approach is the use of osteoinductive biomaterials such as bioglasses, which emulate certain aspects of the mineral phase of native bone. *In vitro*, these materials have demonstrated the abilities to direct osteogenic differentiation of progenitor cells [19-22]. Bioactive ceramics, including bioglasses and calcium phosphate-based materials, were able to form a surface layer of apatite-like mineral in simulated body fluid, a solution with pH and ionic composition close to human plasma [23,24]. These materials, when implanted *in vivo*, were able to assist repair of bone defects [25-27] through recruiting endogenous osteoprogenitor cells and directing their osteogenic

differentiation [28]. However, a drawback of these systems is a weak adherent bond between the newly-formed apatite-like mineral layer and the ceramic, which usually leads to ultimate delamination of these two layers [29]. This could cause serious problems and result in implant failures. Biomineralized materials comprised of both the organic and inorganic phases could be an alternative solution for promoting bone tissue repair *in vivo*. The crystalline phase of the mineral component could be a key parameter in determining the osteoinductive function of calcium phosphate-based materials or ceramics [30]. Development of mineralized materials through biomineralization can be used to control the crystalline nature of the mineral phase and thereby their osteoinductivity [31-34].

1.3 Biomineralized Materials for Bone Tissue Repair

Biomineralization refers to modifications of organic matrices by incorporation of crystalline/semi-crystalline inorganic minerals, such as calcium phosphate (CaP), to emulate the mineralization processes that occur in nature[35,36]. A popular method to achieve this is by introducing polymeric substrates with anionic polar groups[35,37-40] to CaP-rich environments, such as simulated body fluid (SBF). Upon exposure to such environments, these substrates are able to bind calcium ions to mediate potential apatite nucleation and growth. Consequently, such materials tend to exhibit better integration

between the inorganic and organic components compared to organic matrices that are physically loaded CaP minerals within [40-43].

Biomineralized materials are also well established for their ability to adsorb and regulate growth factor signaling. For instance, CaP minerals are known to adsorb osteoinductive growth factors such as bone morphogenic proteins (BMPs) both *in vitro* and *in vivo*[19,44], suggesting their potential use as delivery vehicles for such growth factors. An illustrative example was provided in a recent study by Lee *et al*., in which multiple proteins were adsorbed and delivered from CaP multi-layers in a controllable manner[45]. In addition to the inherent growth factor adsorption capacity, dissolution and reprecipitation of matrix bound CaP can also sequester and release osteoinductive growth factors[46,47]. A recent work by Suarez *et al*. showed that release kinetics of BMP-2 was highly dictated by the dissolution of CaP moieties[48,49]. Dissolution of matrix bound minerals leads to release of adsorbed growth factor that could stimulate osteogenic differentiation of stem cells.

Several studies have indicated that biomaterials containing CaP moieties are able to promote *in vitro* osteogenic differentiation of stem and progenitor cells [26,50,51]. Recently, biomineralized poly (ethylene glycol) diacrylate-co-N-acryloyl 6-aminocaproic acid (PEGDA-co-A6ACA) exhibiting dynamic dissolution-reprecipitation of CaP minerals was developed. This material was shown to induce osteogenic differentiation of hMSCs,

hESCs, and hiPSCs exclusively via the cues arising from the biomaterial- both *in vitro* [52-56]. More interestingly, the biomineralized matrices induced osteogenic differentiation of hMSCs was observed even in the presence of media components that are known to induce adipogenic differentiation[57].

In this dissertation, I evaluated the *in vivo* functionalities of biomineralized PEGDA-co-A6ACA for bone regeneration by studying the effects of structural parameters (i.e. pore size) and biological parameters (i.e. age of the host) on biomaterials-mediated bone repair. Furthermore, I proposed a double network hydrogel to enhance the mechanical properties of the biomineralized materials.

1.4 Overview

The reminder of the document is organized in the following manner:

1.4.1 Chapter 2

This chapter provides a literature review of major research pertaining to design of biomaterials to guide cell behaviors and achieve regenerative functionalities. Specific focus is applied to the design of extracellular matrix analogues to guide stem cell responses and subsets of tunable materials properties that are shown to affect cellular phenotype and functions. As the first author of the review manuscript serving as basis for this chapter, I was involved in all aspects of writing, figure preparation and editing in conjunction with my co-author Shyni Varghese.

Chapter 2 is a slightly modified version of "Substrate Guided Cell Behavior in Regenerative Engineering" published in *Regenerative Engineering: Advanced Materials Science Principles*. Copyright (2017) From *Regenerative Engineering: Advanced Materials Science Principles* by Yusuf Khan, Cato T. Laurencin. Reproduced by permission of Taylor and Francis Group, LLC, a division of Informa plc.

1.4.2 Chapter 3

The work of Chapter 3 identifies and establishes the effect of mineralized PEGDA-co-A6ACA to support *in vivo* bone tissue formation. Furthermore, by using scaffolds with varying pore sizes, I investigated the effects of scaffold pore size on the *in vivo* ectopic bone tissue formation. As the co-author and first author of the two manuscripts serving as the basis for this chapter, I oversaw and was heavily involved in all aspects of this research, including experimental planning, writing, figure preparation, and editing in collaboration with my co-authors Eva C. Gonzalez Diaz, Yu-Ru V. Shih, Manando Nakasaki, Alina Kirillova, Shyni Varghese and Ken Gall.

1.4.3 Chapter 4

Building from the work of Chapter 3, I focus on understanding the effect of host environments on bone regeneration effectiveness of the biomineralized material. Specifically, the work of Chapter 4 studies the effect of physiological age of host on the biomineralized materials-mediated bone tissue formation and reveals important age-

related differences in bone regenerations. As the first author of the manuscript serving as the basis for this chapter, I oversaw and was involved in all aspects of this research, including experimental planning, writing, figure preparation, and editing in conjunction with my co-authors Yu-Ru V. Shih, Manando Nakasaki and Shyni Varghese.

1.4.4 Chapter 5

The work of Chapter 5 describes a new hydrogel system to enhance the mechanical properties of biomineralized PEGDA-co-A6ACA. Specifically, I describe a double network hydrogel with unique contrasting network structure, where the first network is tightly cross-linked by a rigid and brittle polyelectrolyte (A6ACA) while the second network is loosely cross-linked by a soft and ductile neutral polymer (PEGDA). The mechanical property, mineralization capacity and mineral dissolution kinetics of the double network hydrogels are studied and compared with single network hydrogels used in Chapter 3-4. As the first author of the manuscript serving as the basis for this chapter, I oversaw and was involved in all aspects of this research, including experimental planning, writing, figure preparation, and editing in conjunction with my co-authors Alina Kirillova and Ken Gall.

1.4.5 Chapter 6

This chapter summarizes the conclusions and future directions of work described in this dissertation

2. Chapter 2: Design of Biomaterials to Guide Cell Behaviors in Regenerative Engineering Literature Review

In Chapter 2, I discuss current research findings in the design of extracellular matrix analogues to guide stem cell responses and review the subsets of tunable materials properties that are shown to affect cellular phenotype and functions.

Chapter 2 is a slightly modified version of "Substrate Guided Cell Behavior in Regenerative Engineering" published in *Regenerative Engineering: Advanced Materials Science Principles*. Copyright (2017) From *Regenerative Engineering: Advanced Materials Science Principles* by Yusuf Khan, Cato T. Laurencin. Reproduced by permission of Taylor and Francis Group, LLC, a division of Informa plc.

2.1 Design of Biomaterials to Guide Stem Cell Behaviors

2.1.1 Introduction

Stem cells hold enormous potential for a broad spectrum of applications in regenerative engineering - from *in vitro* technological platforms and model systems to cell-based therapies - owing to their ability to self-renew and differentiate into a wide range of specialized cell types. The interaction of stem cells with their surrounding microenvironment is fundamental to multiple cellular processes such as cell migration, proliferation, differentiation, and tissue homeostasis. [58-61] Historically, considerable

emphasis has been placed on using soluble regulators to control stem cell fate and commitment, but studies over the last two decades have shown that the "insoluble" component, the extracellular matrix (ECM), plays an equally important role in regulating various cellular functions, including stem cell growth and differentiation. The ECM has been recognized as a reservoir of biochemical and biophysical signals that actively mediates various cellular processes, contributing to tissue morphogenesis, homeostasis, and regeneration.[62] When the ECM is perturbed, those same interactions could contribute to many diseases like cancer[63-65] and fibrosis.[66]

Biomaterials have been widely used as artificial ECM to study stem cell behaviors. Recent research has established that material-specific properties, including biochemical signals (e.g., immobilized growth factors or functional groups),[67-71] mechanical stimuli (e.g., elastic modulus and viscoelastic properties),[52,72-74] and topographical signals (e.g., pores, geometry, and fibrils),[75-78] have a profound impact on stem cell growth and differentiation. In short, stem cells in contact with biomaterials can sense their surrounding and initiate elaborate intracellular signaling, which eventually translates into coherent information that regulates downstream gene and protein expression. Successful manipulation of these biomaterial-based cues has been used as a promising approach to control stem cell differentiation and facilitate the application of

stem cells in regenerative engineering and generation of functional three-dimensional (3D) tissues.

2.1.2 Design of Biomaterials to Control Cell Functions

Both natural and synthetic biomaterials have been extensively studied as artificial ECMs to guide adhesion, shape, proliferation, and differentiation of stem cells. In general, native ECM-derived materials like collagen, fibronectin, and gelatin are obvious choices because of their intrinsic ability to interact with cells through features such as the presence of cell surface receptor-binding ligands, growth factors, fibrils (in the case of collagen), and susceptibility to proteolytic degradation. Despite these advantages, natural materials often suffer from issues including weak mechanical properties, high cost, potential immunogenicity, short shelf life, and batch-to-batch variability. In contrast, synthetic biomaterials can be easily processed, and their physical and biochemical properties can be tailored to achieve the desired features in a spatiotemporal manner.[79,80] Synthetic materials also elicit minimal immunogenicity. Hence, hybrid materials possessing the biochemical functions of native materials and tunable physical properties of synthetic materials could be ideal candidates for cell culture.

2.1.2.1 Functionalizing synthetic materials with cell-adhesive moieties

Given the propensity of ECM proteins to promote cell-matrix interactions, the functionalization of synthetic biomaterials with proteins or peptides, through either physical blending or chemical conjugation, has been widely used to promote attachment, proliferation, and even differentiation of stem cells.[67-70,81,82] For instance, synthetic matrices modified with several ECM-derived proteins such as laminin (and their isoforms) and vitronectin have been shown to support human pluripotent stem cell expansion *in vitro*.[81,82] Although ECM proteins are ideal for improving cell-matrix interactions, they can be easily denatured when exposed to the non-physiological environment. To circumvent these limitations, peptides instead of proteins can be used to achieve similar functions.[83] Many studies have reported the use of peptide-modified biomaterials to support stem cell phenotypes.[84-86] For instance, Melkoumian *et al.* reported synthetic peptide-acrylate surfaces (PAS) as supporting self-renewal of human embryonic stem cells (hESCs) without karyotypic instability in a chemically defined, xenofree medium condition.[85] In a similar approach, Klim *et al.* identified that a vitronectin-derived peptide sequence, GKKQRFRHRNRKG, could sustain pluripotency and self-renewal of hESCs, where the peptide sequence is shown to engage with the cells through cell surface glycans.[84] Similar strategies have also been applied to guide stem cell differentiation. Incorporation of peptide sequence KLER (lysine-leucine- glutamic

acid-arginine), a collagen II binding domain derived from decorin, was shown to promote chondrogenic differentiation of human mesenchymal stem cells (hMSCs) in polyethylene glycol (PEG) hydrogels.[87]Specifically, incorporation of KLER was found to inhibit collagenase-mediated degradation of cartilage matrices and regulate transforming growth factor- β (TGF-β) signaling by stabilizing the triple-helical structure of collagen type II. The biological activity of immobilized peptides depends on their accessibility, suggesting that optimal orientation and distribution of the tethered ligands are necessary to achieve the desired functions.[88-91]Hyaluronic acid (HA), an ECM polysaccharide known to interact with cell surface receptors such as CD44, has also been extensively studied for cartilage tissue engineering from stem cells.[92-94]

2.1.2.2 Biomaterial Design to Regulate Growth Factor Signaling

Native ECM serves as a reservoir for various growth factors. The extent of growth factor sequestration varies and could have a significant influence on maintaining tissue-specific growth factor signaling. The establishment of a well-controlled growth factor milieu within a synthetic environment is crucial for controlling various cellular functions, including pluripotency and differentiation.[75]

Studies have used the inherent ability of ECM glycosaminoglycans (GAGs) to sequester growth factors through noncovalent interactions. In this regard, biomaterials were either functionalized with GAG molecules[95] or GAG mimetics.[96,97] GAG moieties

strongly and reversibly bind to various morphogens, including fibroblast growth factors (FGFs), vascular endothelial growth factor (VEGF), wingless-type MMTV integration site family, member 3a, TGF-βs and insulin-like growth factors.[98-102] Moreover, the binding of proteins to GAGs increases growth factors' half-lives both *in vitro* and *in vivo* by protecting them from enzymatic degradation and environmental denaturation agents.[103-105] Several studies have used the immobilization of heparin molecules, such as PEG-heparin hydrogels, to promote differentiation of stem cells.[100] Biomaterials that sequester growth factors have also been shown to promote *in vivo* survival and engraftment of transplanted cells.[106,107] Kabra *et al.* reported that the use of HA molecules grafted with 6-aminocaproic acid (6ACA) moieties (HA-6ACA) not only improves the survival of the transplanted hESC-derived cells in skeletal muscle but also promotes their differentiation into tissue-specific cells *in vivo*.[106] It was hypothesized that the HA-6ACA molecules effectively sequester endogenous basic fibroblast growth factors (bFGFs), a key biomolecule involved in postnatal myogenesis and skeletal muscle homeostasis, and regulate their *in vivo* signaling. Immobilization of 6ACA molecules facilitates sequestration of growth factor via electrostatic interactions between the terminal carboxyl group of the 6ACA and the positively charged amino acid domain on the bFGF surface.

2.1.2.3 Biomaterial-Chemistry Mediated Cellular Responses

Besides incorporating molecular recognition elements such as peptides, proteins, or growth factors into biomaterials, studies have also used chemical functional groups to regulate various cellular behaviors. In the absence of active adhesive moieties, interfacial or chemical properties of biomaterials play a crucial role in cell-matrix interaction by mediating nonspecific adsorption of proteins. Both the functional groups and hydrophobicity of the interface have been shown to play key roles in the distribution and binding of proteins, and consequently, the attachment, growth, and differentiation of stem cells.[68,76]

Early evidence has shown that simple functional groups (e.g., OH, CH_3, NH_2, SH, and COOH) tethered on substrate surfaces appear sufficient to elicit preferential differentiation of stem cells. Curran *et al.* showed that chondrogenesis of hMSC was enhanced on OH and COOH-modified glass surfaces, whereas NH_2 and SH-modified surfaces were found to upregulate osteogenesis, and untreated and CH_3-modified surfaces supported the maintenance of undifferentiated states of MSCs.[108] In a similar study, enhanced osteogenic differentiation of MC3T3-E1 cells was observed on self-assembled monolayer surfaces modified with OH and NH_2 functional groups, compared to those functionalized with COOH and CH_3 groups.[109] The authors demonstrated a functional group's dependent activity of cell surface integrins. Specifically, selective

engagement of cell surface $\alpha_5\beta_1$ integrins was present on surfaces displaying OH and NH_2 groups, an engagement of both $\alpha_5\beta_1$ and $\alpha_v\beta_3$ integrins on surfaces with COOH groups, whereas minimal engagement of either integrin on CH_3 surface was observed. Notably, the latter is due to the surface chemistry-mediated exposure of integrin binding sites of the fibronectin at the biomaterial surface. [109] These surface chemistry-dependent differences in integrin activation differentially regulated focal adhesion and subsequent intracellular signaling.[110] Interestingly, mineralization (and, hence, osteogenesis) was observed only on NH_2 and OH-modified surfaces. The β_1-blocking antibody greatly inhibited mineralization on both OH and NH_2 surfaces, while treatment with β_3-blocking antibody on COOH and NH_2 surfaces instead promoted mineralization. These findings suggest that binding of integrin $\alpha_5\beta_1$ upregulates osteogenic differentiation of the cells while $\alpha_V\beta_3$ downregulates it. [109]

In another study, Benoit *et al.* have utilized chemical functional groups of the hydrogel matrices to promote differentiation of encapsulated MSCs in a 3D culture.[111] Incorporation of small chemical groups (carboxyl, phosphate, and t-butyl groups) into PEG hydrogels preferentially drove encapsulated MSCs to differentiate via osteogenic, adipogenic, or chondrogenic pathways. Specifically, MSCs in PEG hydrogel with phosphate groups showed increased expressions of *RUNX2* and *CBFA1*, produced a collagen-rich pericellular matrix, and synthesized more osteopontin, while those

exposed to *t*-butyl groups became adipogenic instead, manifested by upregulation of peroxisome proliferator-activated receptor- gamma (PPARγ) (an adipogenic marker) and intracellular lipid deposition(Figure 2).

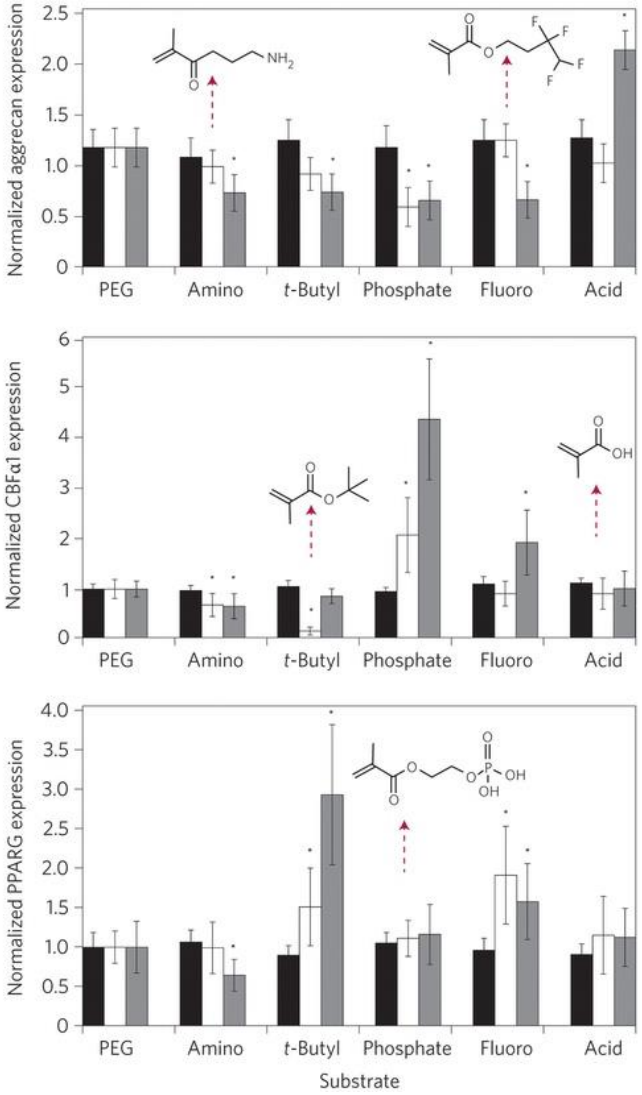

Figure 2: Gene expression profiles of aggrecan, CBFa-1, PPAR✤ for hMSCs seeded on surfaces modified with various functional groups. Data normalized to expression on control surface of unmodified PEG at days 0 (black bars), 4 (white bars)

and 10 (grey bars) of culture[111]. Adapted from [111] with permission, copyright Nature publishing group, 2008)

2.1.3 Tuning Matrix Stiffness to Guide Cell Behavior

In addition to the effects of biochemical cues, mechanical properties of the biomaterials are shown to influence a wide range of biological processes, including embryonic development,[112] tissue homeostasis,[113] and disease pathogenesis.[63-65,114] The most often characterized and reported of the mechanical properties is matrix elasticity (or stiffness). Adhesion of cells to a material triggers signaling transduction cascades that allow for translation of extracellular mechanical cues into intracellular events.[115] The nature of these cascades varies with material elasticity, and controls several cell behaviors such as adhesion, spreading, migration, and cell shape through a variety of mechanosensors, which include integrins,[116-118] stretch-responsive ion channels,[118] and actomyosin cytoskeleton.[119] Signaling activities of focal adhesion kinase (FAK), Rho kinase (ROCK), and steroid receptor coactivator (SRC) family kinase are subsequently regulated to influence stem cell phenotypes.[120-122]

As such, hydrogels with different Young's modulus can be generated typically via varying cross-linking density,[123] precursor concentration,[124,125] or chemistry.[86,126,127] The results from studies investigating the effect of matrix stiffness on stem cell phenotype suggest that, in general, hydrogels with low (soft) and high (stiffer) Young's modulus regulate stem cell differentiation in unique ways with unique outcomes. For example,

human MSCs were found to undergo neurogenesis on soft matrices (E = 0.1−1 kPa), myogenesis on moderately stiff matrices (E = 8−17 kPa), and osteogenesis on stiff matrices (E = 25−40 kPa), respectively (Figure 3).[72] Other stem cell populations, including skeletal muscle stem cells,[128] neural progenitor cells,[129] and embryonic stem cells (ESCs),[129,130] have also been shown to exhibit substrate stiffness-dependent differentiation and function.

The effects of matrix stiffness have been further assessed in 3D cultures.[131-134] Similar to 2D cultures, MSCs were directed to differentiate into osteogenic or adipogenic lineage according to the substrate properties in which they were cultured; in this context, adhesion ligand presentation and local traction force were found to play pivotal roles. [131,132] As stem cells interact with their anchoring matrix through focal adhesion complexes, the integrin binding sites allow force balance transmission across the mechanical continuum of ECM- integrin-cytoskeleton, such that increased resistance to deformation in the matrix is correlated with strengthening of focal adhesions through activities of actomyosin network.

Such changes were found to have a significant effect on several kinase signaling pathways, including those of the FAK and SRC family,[122,135] as well as nuclear translocation of yes-associated protein,[136,137] all of which play key roles in stem cell fate determination.

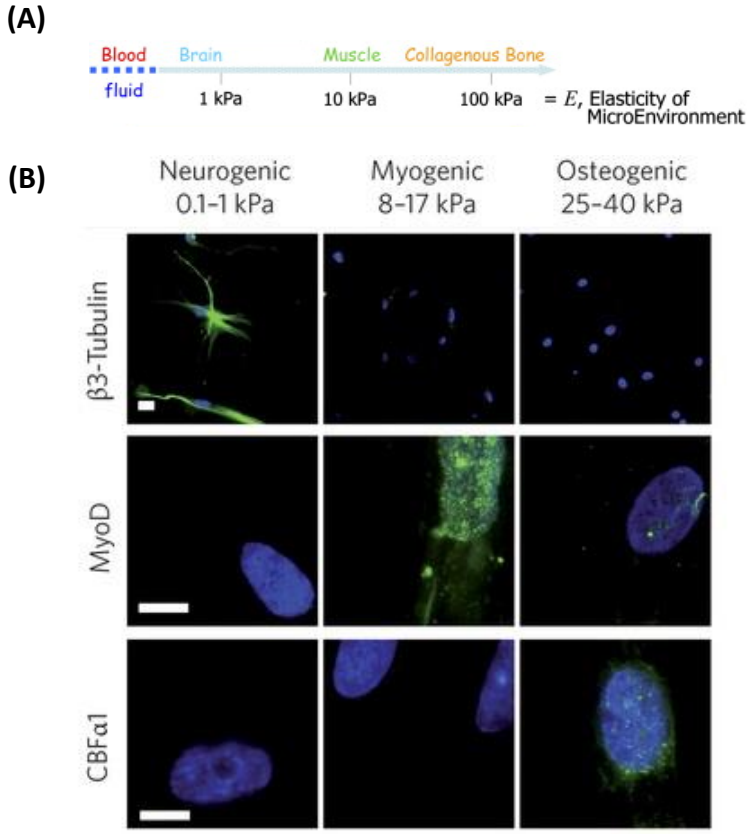

Figure 3: Tissue Stiffness and modulus of poly(acrylamide) substrates influences lineage-specific differentiation. (A) Tissue stiffness: different tissues exhibit a range of stiffness, as measured by the elastic modulus, E. (B)The modulus of poly(acrylamide) substrates influences lineage-specific (neurogenic, myogenic or osteogenic) differentiation, as indicated by immunostaining for the appropriate markers (β3-tubulin, MyoD and CBFα1, respectively, shown in green; cell nucleus in blue)[72]. Adapted from [72] with permission, Copyright 2006 Elsevier

Native ECM molecules such as collagen are nonlinear and viscoelastic in nature; however, the impact of nonlinear viscoelastic characteristics of ECM on cell functions remain relatively underexplored. This time-dependent, nonlinear characteristic of the ECM stems from the intricate interplays among cytoskeletal proteins, adhesion

complexes, and extracellular environments,[138] further increasing the complexity of the mechanical environment. In a recent study, Chaudhuri *et al.* used 3D alginate hydrogels exhibiting stress relaxation properties to investigate the effects of nonlinear mechanical properties on stem cell behaviors.[74] Hydrogels with a faster rate of stress relaxation improved spreading, proliferation, and osteogenic differentiation of MSCs.[74] In a similar effort, Guvendiren and Burdick have used a methacrylated HA-based hydrogel with time-dependent matrix stiffening characteristics to probe the effects of dynamic mechanical properties on MSC differentiation.[139] Their results demonstrated that time-dependent changes in substrate stiffness evoked changes in stem cell phenotypes. In 2D culture, adipogenic differentiation of hMSCs was promoted with later matrix stiffening, while osteogenic differentiation was encouraged through earlier matrix stiffening.[139]

2.1.4 Designing Synthetic Substrate to Provide Topographical Cues

Paralleling the importance of ECM mechanics in regulating cellular functions, ECM proteins exhibit enormous nano/micrometer-scale features, which have been shown to profoundly impact cell signaling. For example, collagen fibers (diameter of several micrometers) are built from ordered collagen fibrils (diameter, 20–200 nm), which in turn are composed of triple helical collagen molecules (diameter, 1–10 nm).[140] Such hierarchical architectures and topographical features of native ECM (e.g., fibrillary structures) have been shown to contribute to various cellular functions.[141] Similarly, the

basement membrane, a ubiquitous ECM component, displays unique nano-topographical characteristics that were found to modulate adhesion, migration, proliferation, and differentiation of the overlying epithelium.[142] Different approaches such as micropatterning, electrospinning, and photolithography have been used to create substrates with topographical features.[111,143-145] These advancements have enabled the investigation of cellular behaviors in response to a broad range of topographical features (e.g., lines, gratings, circles, and pillars) from single cell level to cell clusters in a systematic manner. Many of these techniques have been well reviewed by Théry.[145] In this section, we focus our discussion on the applications of substrate topography in regulating stem cell differentiation.

Development of cell substrates with topographical cues have been touted to provide reproducible and inexpensive systems for *in vitro* stem cell research.[146-150] For example, Ultra-WebTM, a commercially available 3D nanofibrillar scaffold formed by depositing electrospun polyamine nanofibers onto the surface of the conventional cell culture plastics, was found to promote proliferation and self-renewal of ESCs compared to conventional tissue culture dishes.[148] In another study by Ji *et al*., substrates with highly ordered topographical features formed by organized arrangements of silica colloidal crystal microspheres demonstrated capacity for *in vitro* retention of pluripotency and restricted differentiation toward endoderm lineages.[149] A notable

parallel can be found in topographically regulated MSC multipotency retentions on highly ordered arrays of nanopit surfaces. [150]

Substrates with topographical features have also been used to control *in vitro* differentiation of stem cells toward multiple lineages, including osteogenic,[151,152] myogenic,[153] and chondrogenic.[154] There is accumulating evidence that the size,[155] order,[151] and geometry[156] play critical roles in lineage differentiation of stem cells. For instance, hMSCs cultured on disordered nanopits were shown to undergo osteogenic differentiation in the absence of osteogenic induction media,[151] while MSCs maintained their multipotency on highly ordered nanopit surfaces.[150] Lovmand *et al.* utilized a combinatorial approach to identify optimal combinations of size, gap, and height of structures which enhance osteogenic differentiation by MC3T3-E1 (a pre-osteoblastic murine cell line).[157] Following the same approach, Markert *et al.* screened more than 500 topographically distinct micro-structured surfaces with murine ESCs, and they were able to assort the topographies sup- porting undifferentiated murine ESCs phenotypes and those inducing differentiation.[146] Topography at the nanoscale level has been found to change focal adhesion arrangement,[152,158] leading to changes in cytoskeletal configuration and mechanotransduction of the cells,[159,160] which results in differential gene expression and cell function. In addition, the influence of nanotopographical features may be mediated through secondary effects, such as differences in protein

adsorption due to the structural features of the substrate. While most studies involving topographical cues were focused on 2D cultures, pore architecture and size of scaffolds have been demonstrated to influence chondrogenic and osteogenic differentiation of stem cells in 3D cultures.[77,161]

3. Chapter 3: Investigate Effects of Mineralized Materials to Support *in vivo* Bone Tissue Formation

The work of Chapter 3 identifies and establishes the effects of mineralized materials to support *in vivo* bone tissue formation using a mouse critical sized defect model. Biomineralized macroporous scaffolds are able to promote orthotopic bone formation by recruiting endogenous cells and directing their differentiation to form bone tissue. After establishing the *in vivo* functionality of the materials, I further studied the effects of pore size of the scaffold on the bone tissue formation efficiency. Specifically, biomineralized scaffolds with different pore sizes were subcutaneously implanted into wild-type mouse, and neo-bone tissue quality and quantity were compared among scaffolds with different pore sizes. Findings from the work in this chapter shows that pores size greater than 100 μm is greater essential for cell infiltration and bone ingrowth.

As the co-author and first author of the two manuscripts serving as the basis for this chapter, I oversaw and was heavily involved in all aspects of this research, including experimental planning, writing, figure preparation, and editing in collaboration with my co-authors Eva C. Gonzalez Diaz, Alina Kirillova, Yu-Ru V. Shih, Manando Nakasaki, Heemin Kang, Shyni Varghese and Ken Gall.

3.1 Introduction

Bone is a highly dynamic tissue with an intrinsic ability to regenerate or repair in response to traumatic injury. Despite this regenerative ability, extensive bone loss due to

severe trauma, infection, tumor excision, and degenerative disease may lead to bone defects that often require surgical intervention and the use of bone grafts to assist healing. In the United States alone, around 1.6 million bone grafts are needed on an annual basis, resulting in a cost of over 27 billion dollars.[162] For decades, autografts and allografts have remained the standard of care for the treatment of non-healing bone defects.[12] These methodologies, however, suffer from major drawbacks such as donor site morbidity and pain, scarcity, immune-rejection, and risk of disease transmission.[10-12]In addition, a secondary surgery is required for graft harvest, increasing the cost of care and lengthening the treatment process.

Recent efforts have thus focused on developing alternative treatment strategies like tissue engineering, wherein a biomaterial is used in conjunction with exogenous cells or osteoinductive growth factors, such as bone morphogenetic proteins (BMPs).[13,14] Although these biological-dependent therapies have shown great efficacy in promoting bone regeneration, they suffer from numerous drawbacks. The use of high BMP doses to expedite bone formation has been correlated with an increased risk of tumorigenesis and other side effects, such as local bone resorption and ectopic bone formation.[17,18] In addition, the effectiveness of exogenous cell-based therapies is often limited by their scarcity and heterogeneity.[163,164] Biomaterials that possess intrinsic osteoconductivity, osteoinductivity, and osteogenicity and exploit the bone-forming potential of endogenous cells could provide a widely accessible method for treating critical bone

defects. In the recent studies, researchers have developed biomineralized macroporous scaffolds of poly (ethylene glycol) diacrylate-co-N-acryloyl 6-aminocaproic acid (PEGDA-co-A6ACA) capable of providing osteogenic microenvironment with a dynamic CaP mineral dissolution. *In vitro*, these materials promoted osteogenic differentiation of human mesenchymal, embryonic stem cells, and induced pluripotent stem cells in growth medium devoid of any osteogenic-inducing factors[52-56,77].

While chemical properties (e.g. CaP moieties) of the scaffold play a key role in recruitment of endogenous cells and their function (including osteogenic differentiation), emerging studies clearly indicated the role of extracellular cues arising from the physical properties of scaffolds on directing osteogenic commitment of osteoprogenitor cells. In particular, the structural properties such as pore size of the scaffold play a critical role in bone tissue formation [165] by affecting cell adhesion, proliferation, and distribution, as well as nutrient and oxygen availability [166-168]. Although previous studies had demonstrated the effect of bone tissue engineering scaffold pore size on the in-growth of engineered bone tissue within the scaffolds [169-173], the relationship between scaffold pore size and *in vivo* bone formation ability within tissue engineered constructs is not fully understood as is evident from the conflicting reports on the optimal pore size found within the literature. Scaffolds with mean pore sizes ranging from 10–2250 μm have been used in bone tissue engineering resulting in varying degrees of tissue in-growth [174-178]. The optimal pore size for different materials

systems and animal models varied. For example, for hydroxyapatite, pore sizes between 100 and 400 μm are proposed as optimal for osteoconduction [179], and pore sizes greater than 300 μm are shown to have high levels of vascularization which enhances bone tissue formation [165,180]. Moreover, pore sizes smaller than 100 μm may not be sufficient in terms of mass transport and cell migration [174], resulting in the formation of a cellular capsule around the edges of the scaffold. This in turn can limit diffusion of nutrients and removal of waste resulting in necrotic regions within the construct. Conversely, with larger pores size, cell adhesion to the scaffold could be limited due to the decrease in total surface area [181]. Moreover, larger pore sizes may result in excessive void space that may compromise the mechanical properties of the scaffold and decreased total surface area for cell attachment. This change in cellular behaviors are mediated through specific integrin–ligand interactions between cells and the surrounding ECM [61,182-185]. Therefore, maintaining a balance between the optimal pore size for cell migration and specific surface area for cell attachment is essential [165].

In this chapter, I evaluated the potential of biomineralized PEGDA-co-A6ACA scaffolds to direct orthotopic bone formation in a critical-sized cranial defect in mice. I demonstrated that treatment with these mineralized biomaterials results in bone formation of the defect through the formation of mature, vascularized bone tissues from recruited host cells. Furthermore, I investigated the role of the scaffold pore size on *in vivo* ectopic bone formation using biomineralized macroporous scaffolds with different

pore sizes, while having similar porosity. Specifically, I used biomineralized PEGDA-*co*-A6ACA scaffolds with five different pore size ranges: 45-53 μm, 90-106 μm, 160-180 μm, 212-250 μm and 300-355 μm. These scaffolds were subcutaneously implanted into wild type mice. Cell infiltration, bone formation, and vascularization of the scaffolds were analyzed after 2 weeks and 8 weeks post-implantation. The findings from this work suggests that pore size greater than 100 μm is essential for cell in filtration and subsequent bone ingrowth.

3.2 Materials and Method

3.2.1 Graft synthesis and mineralization

Macroporous poly(ethylene glycol)-diacrylate-co-N-acryloyl 6-aminocaproic acid (PEGDA-co-A6ACA) hydrogels were prepared by using a cryogelation method detailed previously.[186] PEGDA and A6ACA were synthesized as described elsewhere.[127,187] A precursor solution consisting of 20% (w/v) PEGDA (Mn = 3.4 kDa) and 0.5 M A6ACA were prepared in 0.5 M NaOH. The precursor solution was mixed with 0.5% (w/v) ammonium persulfate and 0.2% (v/v) N, N, N′-N′-tetramethylethylenediamine (TEMED). Approximately 75 μL of the above solution was placed onto a chilled polystyrene dish. A chilled 15 mm coverslip was placed over the precursor solution and the solution was left to polymerize for 24 h at -20°C. Phosphate-buffered solution (PBS) maintained at room temperature was added to the gel to thaw ice crystals within the crosslinked structures and form macroporous hydrogels. The macroporous hydrogels

(i.e., cryogels) were subsequently punched into 4 mm diameter disks of 0.7 mm thickness.

To make hydrogels with different pore sizes, macroporous hydrogels were prepared by poly (methyl methacrylate) (PMMA) leaching method. Briefly, cylindrical polypropylene molds (5 mm in diameter) were packed with 30 mg of five different PMMA microspheres with diameters of 45~53 μm, 90~106 μm, 160~180 μm, 212~250 μm or 300~355 μm. Approximately, 18 mL of precursor solution containing 20% (w/v) PEGDA, 0.5 M A6ACA in 0.5 N NaOH, and 0.3% (w/v) Irgacure was added into the PMMA-packed mold and photopolymerized by using ultraviolet light (l = 365 nm) for 10 min. PMMA beads were leached out by using acetone for 3 days and hydrated in deionized (DI) water to yield macroporous hydrogels with 5 distinguished pore sizes. The resulting hydrogels were punch into cylinders measuring 6 mm in diameter and 2 mm in thickness.

Mineralization of the cryogels and PMMA-based hydrogel were achieved by immersing the constructs in simulated body fluid (m-SBF), prepared as previously described[35], for 12 h, and subsequently in 40 mM Ca^{2+}/24 mM PO_4^{3-} (pH 5.2) under vacuum for 1 h. The cryogels were briefly rinsed in ultrapure water and immersed in fresh m-SBF for 48 h at 37°C. The mineralized cryogels were then briefly washed with PBS to remove excess m-SBF, sterilized by immersion in 70% ethanol for 3 h, and washed in sterile PBS.

3.2.2 Calcium Phosphate Assay

Calcium and phosphate assays were performed to determine the amount of Ca^{2+} and PO_4^{3-} in the biomineralized scaffolds and their release to the surrounding medium. The scaffolds were rinsed and homogenized in ultrapure water. The homogenized scaffolds were freeze-dried, and their dry weights were recorded. Dried scaffolds were incubated in 0.5 M HCl at 25 °C. Incubation medium was collected after 3 days, which was sufficient to dissolve all the minerals from the scaffolds, and the amount of $Ca^{2+}$and PO_4^{3-} was measured.

To assess dissolution of Ca^{2+} and PO_4^{3-} from the mineralized scaffolds and their release to the surrounding medium, dried scaffolds were rehydrated and equilibrated in ultrapure water. After reaching the equilibrium swollen state, the scaffolds were incubated in 1 M Tris-HCl (pH = 7.4), free of these ions, at 37 °C for 7 days. Incubation solution was collected and replaced with fresh medium daily. The collected incubation solution was used to determine the release of Ca^{2+} and PO_4^{3-} ions from the scaffolds.

A calcium assay was conducted based on the manufacturer's protocol (Calcium reagent set, Pointe Scientific, catalog number: C7503) as described previously [52]. Briefly, 20 μL of the sample solution was mixed with 1 mL of assay solution containing o-Cresolphthalein complexone (CPC). The absorbance of the mixture solution was measured at 570 nm by a UV/Vis spectrophotometer (Beckman Coulter, DU 730). The

Ca^{2+}concentration was computed from a standard curve generated for a concentration range of 0-4 mM Ca^{2+}.

A phosphate assay was conducted as detailed elsewhere [188]. Briefly, an assay solution was prepared by mixing 1 volume of 10 mM ammonium molybdate, 2 volumes of acetone, and 1 volume of 5 N H_2SO_4. One mL of this assay solution was mixed with 125 μL of the sample solution. To this, 100 μL of 1M citric acid was added. The absorbance at 380 nm of the resultant product was determined by a UV/Vis spectrophotometer. The PO_4^{3-} concentration was computed from a standard curve generated for a concentration range of 0–4 mM H_2SO_4.

3.2.3 Scanning electron microscopy (SEM) and energy dispersive spectra (EDS)

Scanning electron microscopy (SEM) was used to examine the pore structures of the mineralized scaffolds. The scaffolds were cut into thin slices, followed by freeze-drying for 24 h. These samples were sputter coated (Emitech, K575X) with iridium for 7 s and imaged using SEM (Philips XL30 ESEM). The mineral composition of the scaffolds was determined through EDS analysis. ICA software was used to quantify the calcium to phosphate atomic ratio (Ca/P) from the resulting elemental spectra.

3.2.4 Surgical procedures and biomaterial implantation

In vivo function of the implants was performed in C57BL6/J mice (2 months old) following the approval of the Institutional Animal Care and Use Committee (IACUC) at the University of California, San Diego and were performed in accordance with national

and international guidelines for laboratory animal care. In preparation for surgery, mice were anesthetized using ketamine (Ketaset, 100 mg/kg) and xylazine (AnaSed, 10 mg/kg) buprenorphine (0.05 mg/kg) via intraperitoneal injection.

For the cranial defect, a skin incision was made along the length of the calvaria to expose the parietal region and a 4 mm-diameter defect was made in both the left and right parietal bones with a 4-mm biopsy punch [187]. A sterile cryogel (mineralized and non-mineralized) was transplanted onto each defect site. Following implantation, the skin was sutured, and mice were kept on a warm heating pad until wakening. Mice were kept in separate housing cages. The ability of the mineralized biomaterials to support neo-bone tissue formation to repair critical bone defects were compared against groups treated with corresponding non-mineralized materials and groups with sham surgeries (untreated defects). The bone tissue formation and healing of the critical bone defects were analyzed as a function of time at 2- and 8-week post-procedure.

For subcutaneous implantation, the mice were placed into a prone position and prepared in a standard surgical fashion. A single midline incision (1.5 mm) on the back of the mouse was made, and four subcutaneous pouches (cranial-left and -right and caudal-left and -right) were constructed by blunt dissection using a 1 cm wide spatula. Four mineralized macroporous scaffold of same porous size (fabricated from leaching PMMA microsphere of five diameters of either 45~53 μm, 90~106 μm, 160~180 μm,

212~250 μm or 300~355 μm) were inserted into the pouches. Three mice were implanted with the same materials, and five different materials groups were used.

Following implantation, the skin was sutured, and mice were kept on a warm heating pad until wakening. After the surgery, all the mice were kept in separate housing cages. The ability of the mineralized scaffolds to support ectopic bone tissue formation were compared among different groups of macroporous scaffolds. The ectopic bone formations were analyzed as a function of time at 2- and 8-week post-implantation.

3.2.5 Mercury intrusion porosimetry (MIP)

MIP measurement was carried out by using a mercury porosimeter (Micromeritics, AutoPore IV) to determine pore diameter, pore area, and porosity of the non-mineralized and mineralized macroporous hydrogels. The porous samples were briefly rinsed with deionized water and then subject to lyophilization. The dried samples were loaded into penetrometer into which mercury was intruded at the pressure ranging from 0.2 to 48.2 psia. The volume of the intruded mercury into the porous samples at each pressure was acquired and utilized for the analysis by using the software (AutoPore IV 9500 v1.09.01).

3.2.6 Micro-computed tomography (μCT)

Micro-computed tomography (μCT) was performed to assess hard tissue formation within the cranial defect at 2- and 8-week post-implantation. The entire skull

of each mouse was harvested and fixed in paraformaldehyde (PFA) by immersing the specimens in 4% PFA for 4 days at 4°C. The retrieved samples were rinsed with PBS and secured tightly between styrofoam disks within a conical tube. Scanning was performed using SkyScan 1076 (Bruker: 9 μm/pixel, 50 kV, 0.5 mm Al filter). Scan reconstruction was performed using the NRecon software (SkyScan, Bruker). Using CT Analyzer software (SkyScan, Bruker), cranial bone tissues were segmented using a threshold of 90-255. The reconstructed images were used to generate 3-D models by using CT Analyzer software (SkyScan, Bruker). Bone mineral density (Bone volume/Total volume, BV/TV) was quantified from the reconstructed images.

3.2.7 Histology and immunohistological staining

The PFA fixed samples were decalcified by using 10% ethylenediaminetetraacetic acid (EDTA, pH 7.4), where the samples were incubated in the solution for 2 weeks at 4°C. The decalcified samples were gradually dehydrated with increasing concentration of ethanol and equilibrated in CitriSolv. Following dehydration, samples were incubated in a mixture of 50% (v/v) CitriSolv, 50% (v/v) paraffin for 30 min at 70°C. The samples were then embedded in paraffin and sliced into sections of 10-μm thickness using a rotary microtome (Leica, RM2255). Before staining, the sections were deparaffinized using CitriSolv and subsequently rehydrated with decreasing concentration of ethanol until the samples were equilibrated with deionized (DI) water.

Hematoxylin and eosin (H&E) staining was performed by incubating the rehydrated samples in hematoxylin solution for 2 mins (Ricca, catalog no. 3536-16), followed by eosin-Y solution (Richard-Allan Scientific, catalog no. 7111) for 20 seconds. The stained sections were dehydrated, mounted and imaged using a Keyence microscope (BZ-X700).

Histomorphometric analysis was conducted to evaluate the quantity of the neo-bone tissue. Six H&E images of each defect were randomly selected and areas of the newly formed bone tissues resembling the morphology of native bone were identified. The total area of the newly formed bone tissue, as well as the total defect area, were analyzed using ImageJ. The mean areal density of the newly formed bone was presented as the fraction of bone area per defect area.

Osteoclasts were detected by the tartrate-resistant acidic phosphatase (TRAP) staining. Briefly, The TRAP incubating solution was prepared by first mixing 50 μL of Fast Garnet GBC base solution with 50 μL of sodium nitrite solution. This mixture was added to 4.5 mL of pre-warmed DI water at 37°C. After mixing, 50 μL of Naphthol AS-BI phosphate solution, 200 μL of acetate solution, and 100 μL of tartrate solution were added and mixed to generate a working solution. Rehydrated sections were immersed in the working solution, incubated at 37°C for 1 h in dark, and rinsed with DI water. After staining, the sections were dehydrated with increasing concentration of ethanol and finally with CitriSolv until equilibrium was reached. Slides were mounted with

glycerol and imaged immediately. Quantification of TRAP-positive staining was performed using ImageJ. The mean areal density of TRAP-positive area was presented as the percentage of total TRAP-positive area over total tissue area.

For immunohistochemical and immunofluorescent staining, rehydrated sections were immersed in a solution of proteinase K (20 μg/mL; Invitrogen, catalog #1000005393) in 95% (v/v) TE buffer (50 mM Tris-HCl, 1mM EDTA, and 0.5% [v/v] Triton X-100; pH 8) with 5% (v/v) glycerol and incubated for 15 min at 37°C. For immunohistochemical staining, sections were incubated in a blocking buffer containing 3% (w/v) bovine serum albumin (BSA) for 1 h at 25°C. Samples were incubated with primary antibody against osteocalcin (OCN) (1:100, rabbit polyclonal, Abcam, catalog#ab93876), or BMP-2 (1:100, rabbit polyclonal, Abcam, catalog #ab1493) in blocking solution for 9 h at 4°C. Sections were rinsed with PBS and treated with 3% (v/v) hydrogen peroxide for 7 min at 25°C. The samples were then incubated with secondary antibody (1:100, horseradish peroxidase-conjugated donkey anti-rabbit, Jackson ImmunoResearch, catalog #711-035-152) in a blocking solution for 1 h at 25°C. The treated sections were rinsed with PBS and developed by immersion in 3,3'-diaminobenzidine (DAB) substrate solution (Vector Laboratories, catalog #SK-4100) for 1 min at 25°C. The sections were washed with PBS and gradually dehydrated using increasing concentrations of ethanol and incubated in CitriSolv until equilibrium was reached. Slides were mounted and imaged immediately. For immunofluorescent

staining, sections were washed with PBS and permeabilized using 0.1% Triton X-100 for 10 min at 25°C, which were then treated with sodium borohydride solution (2.5 mg/mL in 50% [v/v] ethanol) for 30 min at room temperature. The sections were immersed in a blocking solution (3% [w/v] BSA and 0.1% [v/v] Triton X-100) and incubated for 1 h at 25°C. Sections were then incubated with primary antibody against CD31 (Platelet endothelial cell adhesion molecule [PECAM-1], 1:100, goat Santa Cruz Biotechnology, catalog #sc-1506) in a blocking buffer for 12 h at 4°C and rinsed with PBS.

The immunohistochemical (IHC) and immunofluorescent staining were analyzed using ImageJ. For IHC staining, the expression of the markers was represented using mean histogram intensity as described earlier [189]. Histogram intensity ranges from 0-255, with 255 representing white (lightest) and 0 representing black (darkest), indicating that the higher the histogram intensity, the lower the expression of the marker. For immunofluorescent staining, the mean areal percentage of the CD31-positive region was presented as percentage of total CD31-positive area over total defect area.

3.2.8 Mechanical testing

Monotonic compression tests were conducted on all porous groups ($n = 4$/group) and a nonporous scaffold group (n=4) at a displacement rate of 1 mm/min until mechanical failure using a Test Resources 910LX25 servohydraulic test machine (max capacity of 25kN). Elastic modulus was calculated using the tangent method from the

initial linear region of the stress-strain curve. Mechanical properties including compressive modulus and strength were fitted by power-law.

3.3 Results

3.3.1 Characterization of Macroporous Hydrogels

The macroporous structure of non-mineralized and mineralized cryogels was confirmed through SEM (Figure 4A). In addition to the interconnected macroporous structures, SEM imaging also revealed the presence of bound minerals within the mineralized matrices, which exhibited a flat, plate-shaped morphology (Figure 4A).

For scaffolds with different pore sizes, SEM characterization confirmed that the grafts exhibited interconnected pore structure (Figure 5A) with different pore size for each group. The mean diameters of the pores in each group were calculated based on the SEM images and shown in (Figure 5C). Elemental analysis further confirmed the presence of CaP minerals within the mineralized cryogels and the calcium (Ca^{2+}) to phosphate (PO_4^{3-}), (Ca/P), ratio was estimated to be 1.5 (Figure 5B).

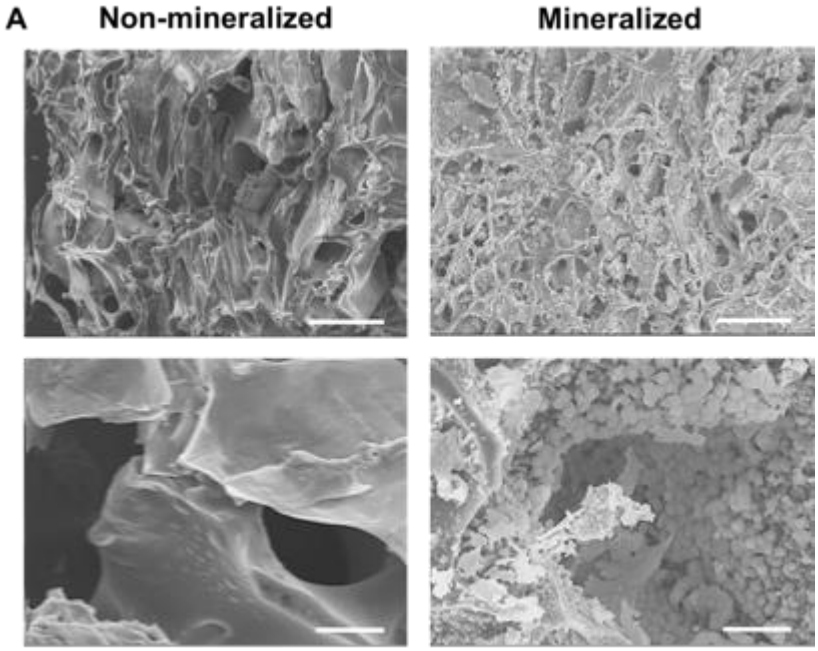

Figure 4: Biomineralized matrix characterization. (A) SEM images of non-mineralized and mineralized macroporous cryogels. Scale bars: 100 μm (top panels) and 10 μm (lower panels). (B) EDS showing presence of calcium and phosphate ions within mineralized hydrogels. EDS, energy-dispersive spectra; SEM, scanning electron microscopy.

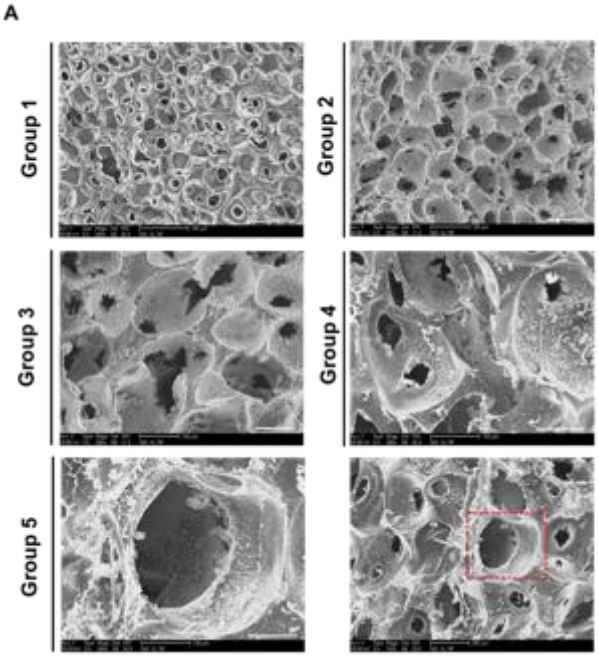

B

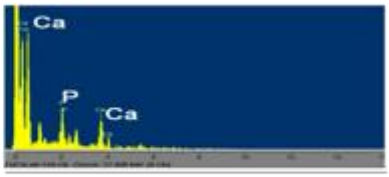

Element	Weight%	Atomic%
P	34.04	40.04
Ca	65.96	59.96
Totals	100.00	100.00

C

Group	PMMA bead size (um)	Pore Diameter (μm)
1	45-53	58.5 ± 6.8
2	90-106	88.1 ± 17.4
3	150-180	141.4 ± 25.0
4	212-250	233.5 ± 25.1
5	300-355	312.4 ± 39.4

Figure 5: SEM/EDS and Calcium Phosphate Dissolution of mineralized PEGDA-co-A6ACA macroporous hydrogel. (A) Scanning electron microscopy image of mineralized PEGDA-co-A6ACA macroporous hydrogel of different groups. (B) Elemental Dispersive Spectroscopy (EDS) spectrum, indicating presence of calcium and phosphate in the mineralized phase with Ca/P ratio of 1.5. (C) Group number with corresponding PMMA leaching particle size, and pore size quantified from SEM images

3.3.2 Mechanical properties

Representative compressive stress-strain curves are shown in Figure 6. The porous scaffolds demonstrated significantly lower ultimate compressive strength than the nonporous scaffolds. For all the porous samples, the stress-strain curves were convex and exhibited similar values of stress and strain in the low-strain region (strain < 0.5; see inset in Figure 6) indicating minimal measurable changes in stiffness as a function of pore size. This result is expected as stiffness depends strongly on pore volume fraction but typically not pore size in this size range. The slope of the curves increase

significantly at high strain (strain > 0.6). Failure strain generally increased as pore size increased, and ultimate compressive strength decreased significantly as the pore size increased above 200 μm (Groups 4 and 5). This is result expected based on the inherent difference in large strain collapse of pores with varying wall structures. For example, large pores have walls with higher aspect ratios that more readily collapse under compression which is why large pore groups collapse more easily at large strains.

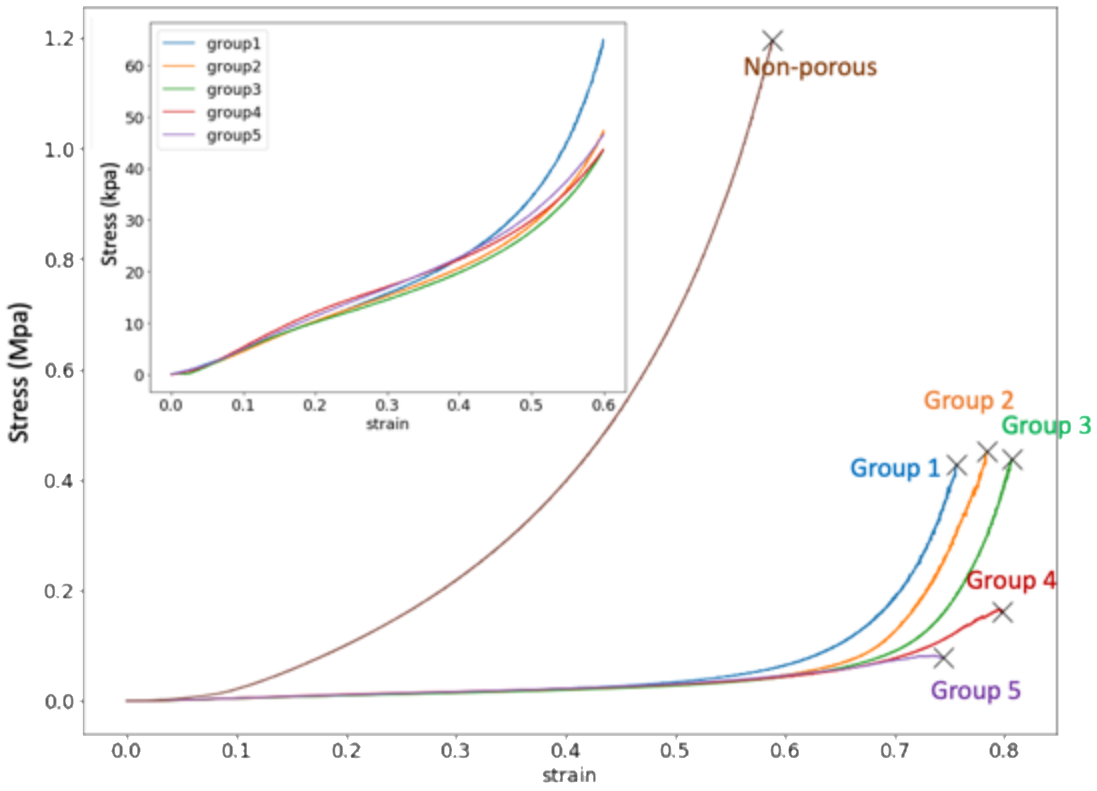

Figure 6: Stress-strain curves of mineralized nonporous and porous (Groups 1-5) scaffolds. Inset: stress-strain curves at the lower strain region (< 0.6) for Groups 1-5 (n = 4 /group).

The total content of Ca and PO_4^{3-} the different scaffold group were shown in (Figure 7A). Amongst all group, there was no significant difference in the total content of CaP minerals on the scaffold (Figure 7B). These CaP minerals of the mineralized matrix undergo a dynamic dissolution-precipitation responding to the Ca^{2+} and PO_4^{3-} in the milieu. Shown in (Figure 5B), both Ca^{2+} and PO_4^{3-} were released from the mineralized scaffolds and showed similar release profiles (Figure 7B). The molar ratio between the released Ca^{2+} and PO_4^{3-} was estimated to be ~1.6 ± 0.2 (averaged over 7 days). This is very close to the stoichiometric Ca/P ratio in hydroxyapatite (1.67) suggesting that the Ca^{2+} and PO_4^{3-} release could be due to the dissolution of an apatite-like calcium phosphate phase from the mineralized hydrogel. Moreover, despite vast difference in pore size, all groups demonstrated similar release profiles of profile of Ca^{2+} and PO_4^{3-} ions.

Mercury intrusion porosimetry suggested similar porosity among the different groups of hydrogels shown in Figure 7C for both non-mineralized and mineralized scaffolds. Total pore area per unit mass of scaffolds. Figure 7C suggested that the area decreased as pore size increased. Mineralized scaffolds have higher pore surface area than their non-mineralized counterpart, suggesting that the presence of mineral crystals on the materials contributes to the increases in total surface area.

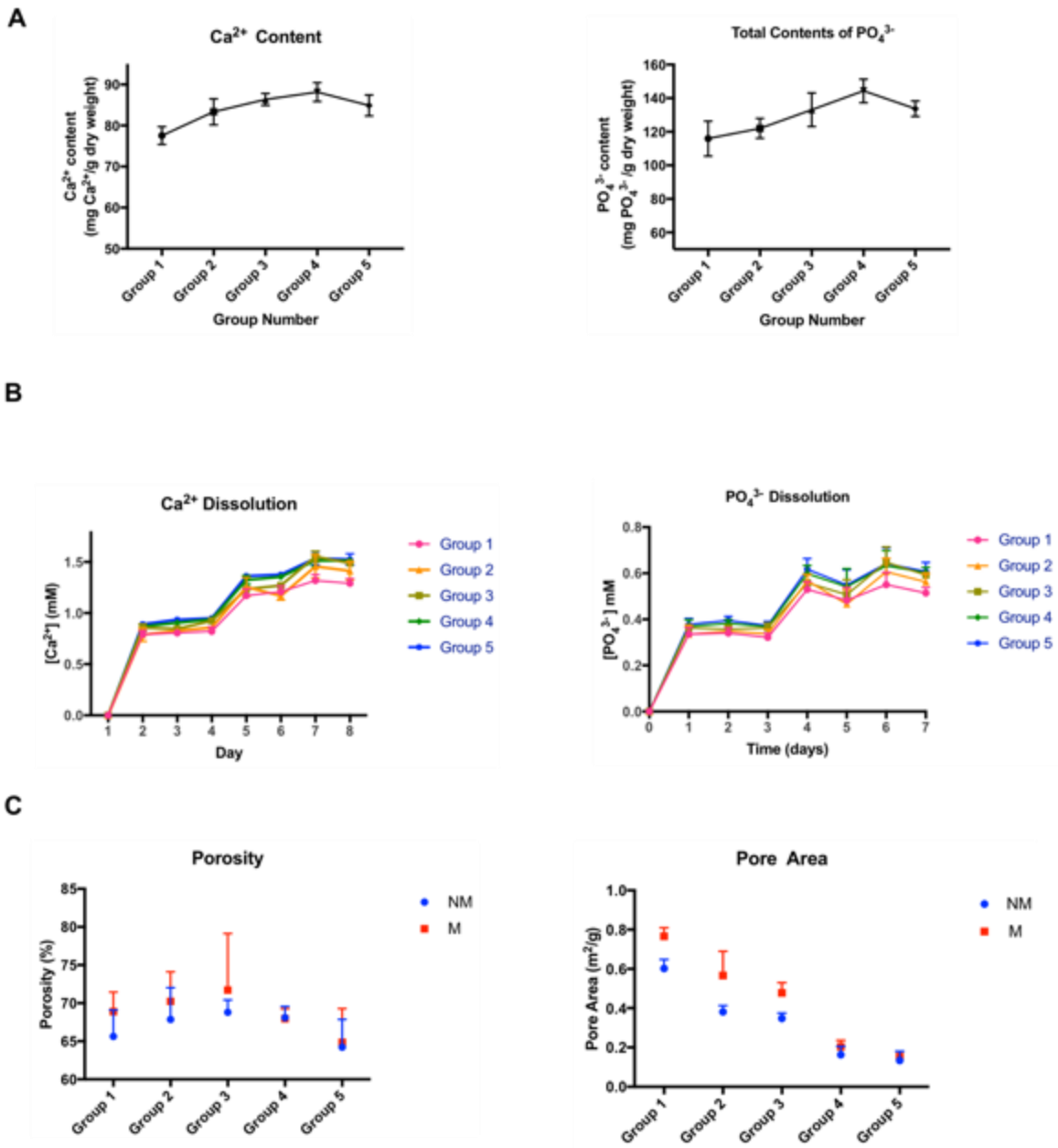

Figure 7: Calcium Phosphate content and dissolution and mercury intrusion porosimetry (MIP) measurement of the PEGDA-co-A6ACA scaffold. (A) Total $Ca^{2+}$and PO_4^{3-} content of the biomineralized scaffold prior to implantation. (B) Release of Ca^{2+} and PO_4^{3-} as a function of time in ion-free Tris-HCl (1M, pH = 7.4) (C) Mercury intrusion porosimetry measurements of (left) porosity and (right) pore area of non-mineralized and mineralized macroporous scaffolds of all groups.

3.3.3 *In vivo* hard tissue formation

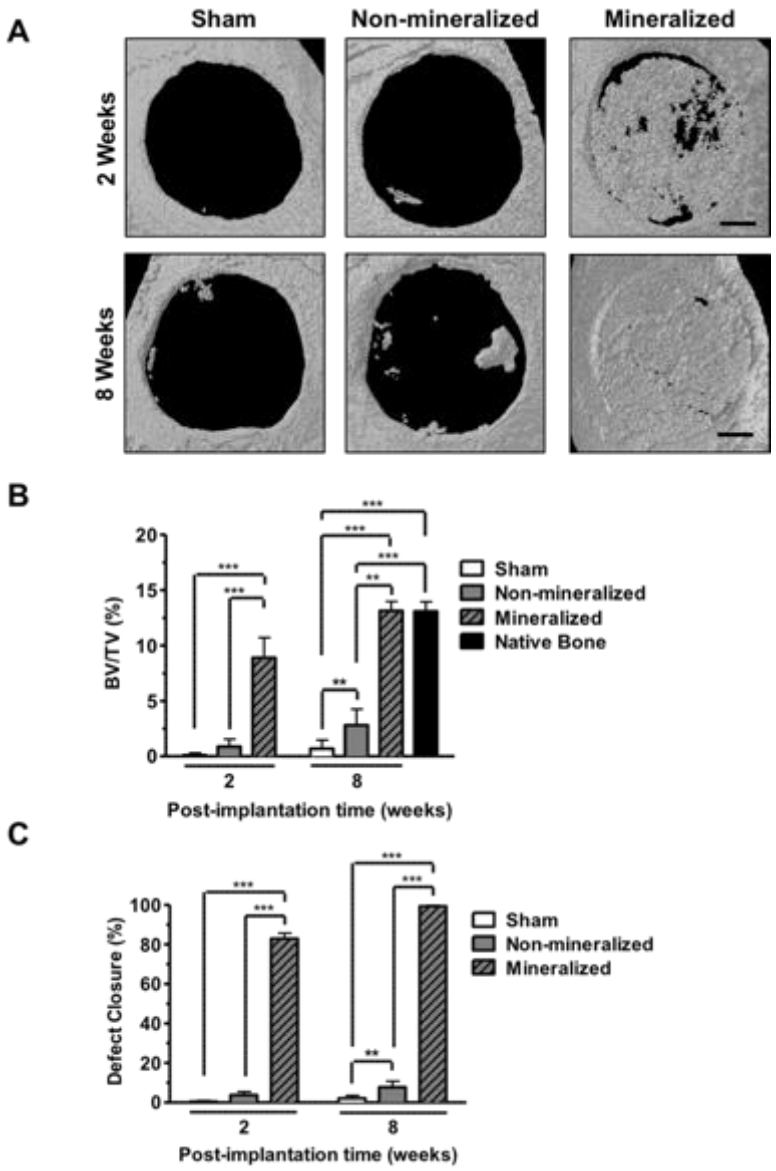

Figure 8: Calcified bone tissue formation within critical-sized cranial defects. (A) μCT images of mouse cranial defects treated with mineralized and non-mineralized cryogels, as well as sham groups, at 0 (day 0), and 2 and 8-week post-implantation. Scale bars: 1 mm. (B) Quantification of bone volume for sham, non-mineralized, and mineralized groups at 2- and 8-week posttreatment. *Asterisks* denote *p* values with statistical significance (*$p < 0.001$). μCT, Microcomputed tomography.**

Hard tissue formation within the cranial defects treated with mineralized and non-mineralized cryogels as well as sham groups was examined by using μCT at 2- and 8-week post-implantation (Figure 8). Two weeks post-implantation analysis showed hard tissue formation compared to non-mineralized and sham groups (Figure 8A). Quantification of hard tissue formation in the defect site revealed a significantly higher bone volume in groups treated with mineralized cryogels compared to sham and non-mineralized groups. Furthermore, the percent bone volume at 8 weeks was comparable to that in the surrounding native bone tissue (Figure 8B). An almost complete closure of the defect was achieved in groups treated with mineralized macroporous materials by 8 weeks (Figure 8C). In contrast, sham and non-mineralized groups revealed minimal to no hard tissue formation within the defect site throughout the extent of the study.

For scaffolds with different pore sizes, after 2 weeks and 8 weeks of subcutaneous implantation, the scaffolds were retrieved and analyzed for bone tissue formation. Gross images of the excised implants shown in Figure 9A indicated hard tissue ingrowth within the all the scaffolds. At 2 weeks post-implantation, group 4 and 5 exhibited pronounced cell infiltration than the other groups. At 8-weeks post implantations, all groups displayed significant tissue ingrowth within the scaffolds.

3-D micro-computed tomography (micro-CT) were performed to further analyze the hard tissue formation within the scaffolds as shown in Figure 9B. At 2-week point

implantation, quantification of BV/TV revealed varying extent of calcification amongst different groups. Among all the groups, Figure 9 exhibited the highest and group 4 the second highest amount of calcification; whereas least amount of calcification was observed in group 1. From the 3D images, group 4 and 5 showed homogenous calcification throughout the matrices; however, as the size of the porous decreased, the hard tissue was more likely to formed only on the peripheral of the implants, with apparent volumes devoid of calcification at the center of the implants shown in group 1.

At 8-week post implantation, all groups displayed significantly more calcifications than 2-week, suggesting persisted mineral deposition from 2 weeks to 8 weeks post-implantation. In the case of group 1, although more hard tissue was observed at the peripheral of the implants compared to 2 weeks as evidenced by increased BV/TV, unlike the other groups, the center of the implants displayed minimal hard tissue formations. Except group 1, all the other groups exhibited dense and homogeneous hard tissue formation throughout the implant, and there were no significant differences in amount of hard tissue formation among these groups (Figure 9C).

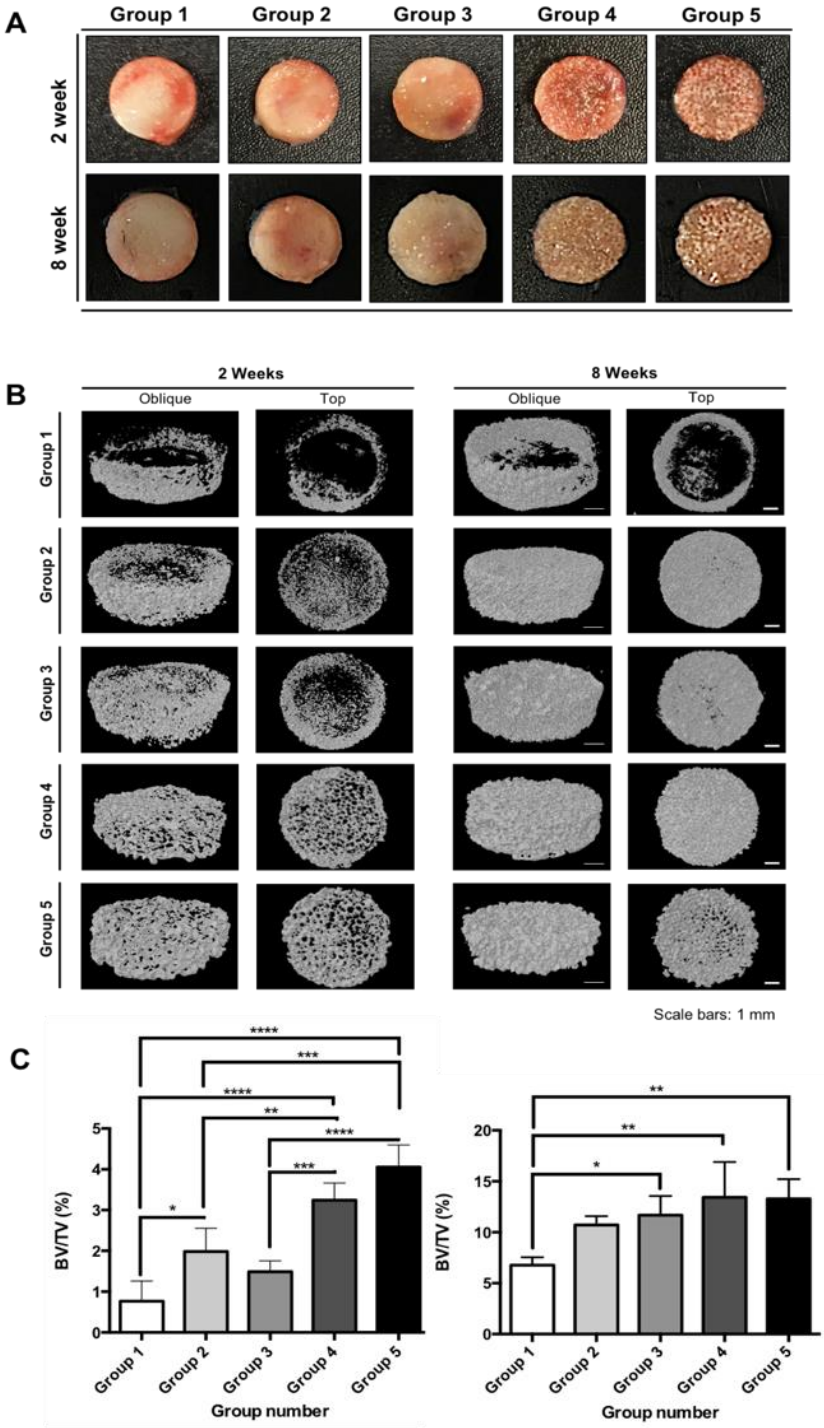

Figure 9: Growth images and Micro-computed tomography (μCT) images and quantification of excised scaffolds. (A) Gross images of excised scaffold at 2 weeks and 8 weeks post-implantation. (B) MicroCT images of the excised scaffolds at 2

weeks and 8 weeks post-implantation. With oblique view and top view. Scale bar: 1 mm. (C) Quantification of bone mineral densities for all groups at (left) 2 and (right) 8 weeks post-treatment. Asterisks denote p-values with statistical significance (*indicates $p < 0.001$, ** indicates $p < 0.01$, * indicates $p < 0.05$).**

3.3.4 Histological assessment of bone formation and cell recruitment

For the cranial defect study, Hematoxylin and Eosin (H&E) staining was performed for cranial sections harvested following 2 and 8 weeks post-treatment to further evaluate the healing process and neo-bone tissue formation at the defect site (Figure 10 and Figure 11). After 2 weeks, defects treated with both non-mineralized and mineralized biomaterials showed significant host cell infiltration, which was homogeneously distributed throughout the implant (Figure 11). By 8 weeks, groups treated with mineralized cryogels revealed abundant ECM throughout the defect site (Figure 10). Despite significant host cell infiltration, no detectable bone tissue formation was observed in defects treated with non-mineralized cryogels. In the case of sham groups, no bone formation was observed, and the defects were bridged by a thin layer of fibrous tissue, which is consistent with that normally found in non-healing bone defects(Figure 10 and Figure 11).

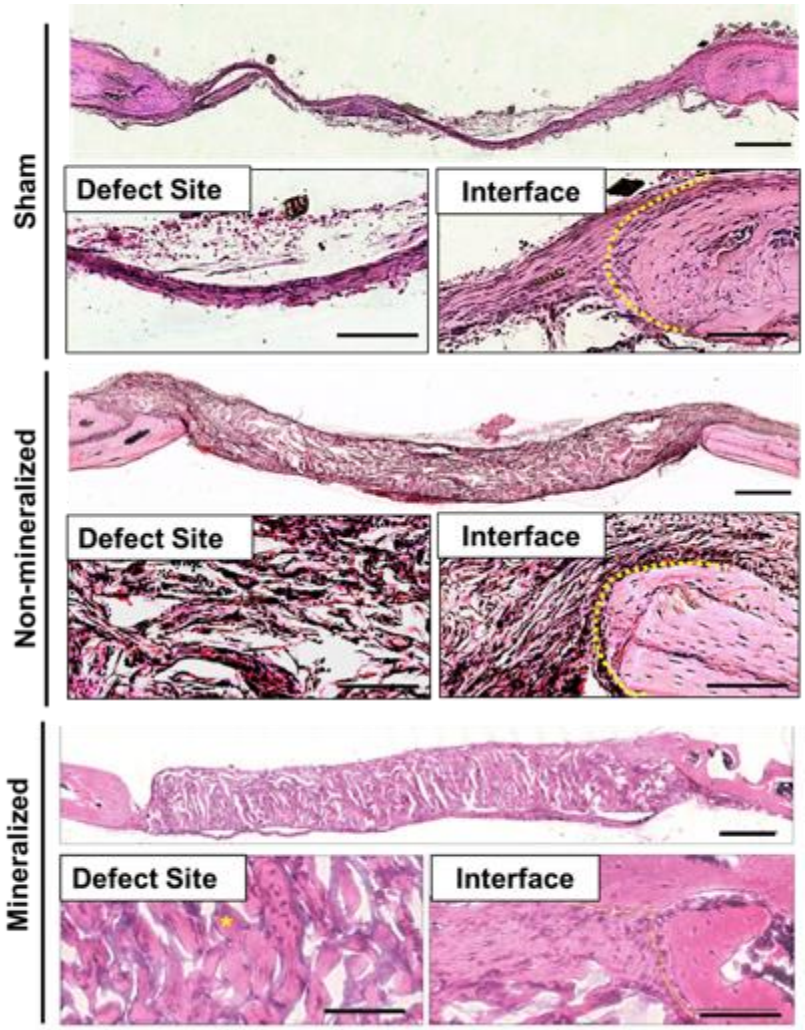

Figure 10: Morphological assessment of bone formation within critical-sized cranial defects. H&E staining of cranial sections following 8 weeks of implantation. High magnification images reveal bone tissue within the defect site (lower left panels) and at the interface between the defect site and native bone (lower right panels). A yellow dotted line was used to delineate the location of the interface between the neo-tissue/implant and native bone. Yellow asterisks denote bone tissue. Scale bars: 500 μm (upper panel) and 20 μm (lower panels). H&E, hematoxylin and eosin

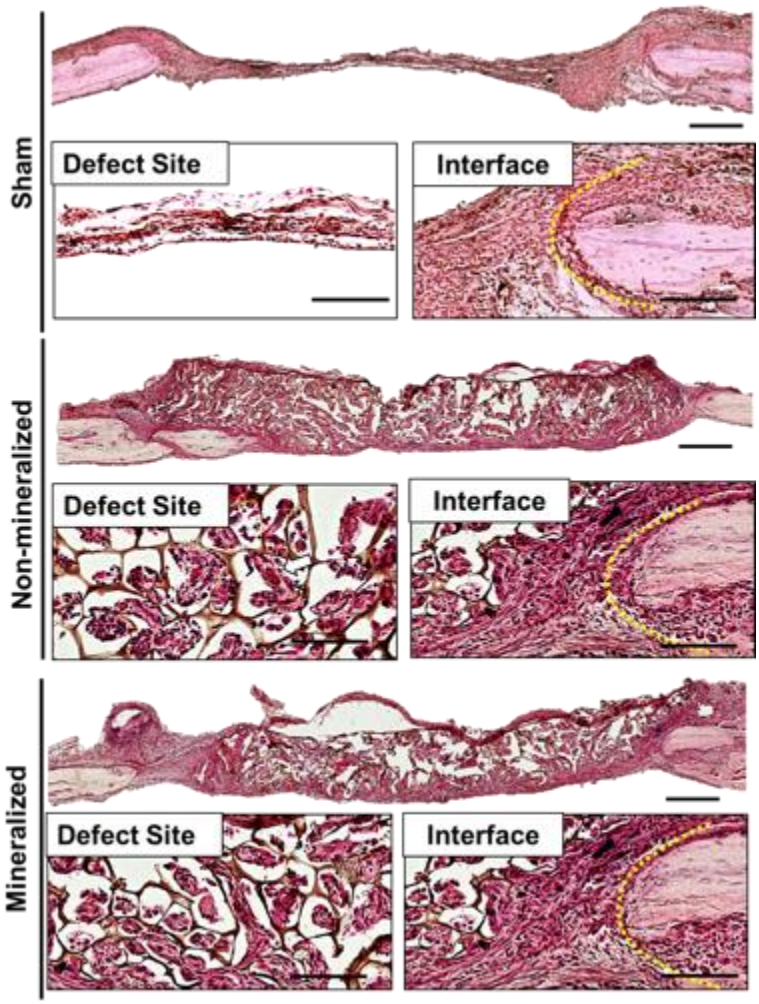

Figure 11: H&E staining of cranial sections following 2 weeks of implantation. High magnification images reveal tissue found within the defect site (lower left panels) and the interface between the defect site and native bone (lower right panels). A yellow dotted line was used to delineate the location of the interface with native bone. White arrows indicate intraluminal blood vessels. Scale bars: 500 μm (upper panel) and 30 μm (lower panels).

For pore size study, H&E staining after 2 weeks implantation showed significant host cell recruitment into the scaffolds in all groups (Figure 12). However, scaffolds with smaller pore sizes of 45~53 μm, 90~106 μm, only showed cell infiltration at the edge of

the scaffold whereas the center of the construct had minimal cell infiltration. Scaffolds with the larger pore size (group 3~5) facilitated a higher rate of scaffold infiltration with more homogenous cell distribution. In group 3, 4, and 5, pronounced cells recruitment was seen in the center of the scaffold.

At 8 weeks post-implantation, bone formation in group 1 only limited to the peripheral area of the implants, and the center of the implant is almost devoid of any ECM deposition. Similar to group 1, in Group 2, significant amount of bone formation was observed at the peripheral area, but group 2 showed some form of bone formation at the center of the implant (Figure 12). In group 3, 4, and 5, bone formation was observed homogenous throughout the implant.

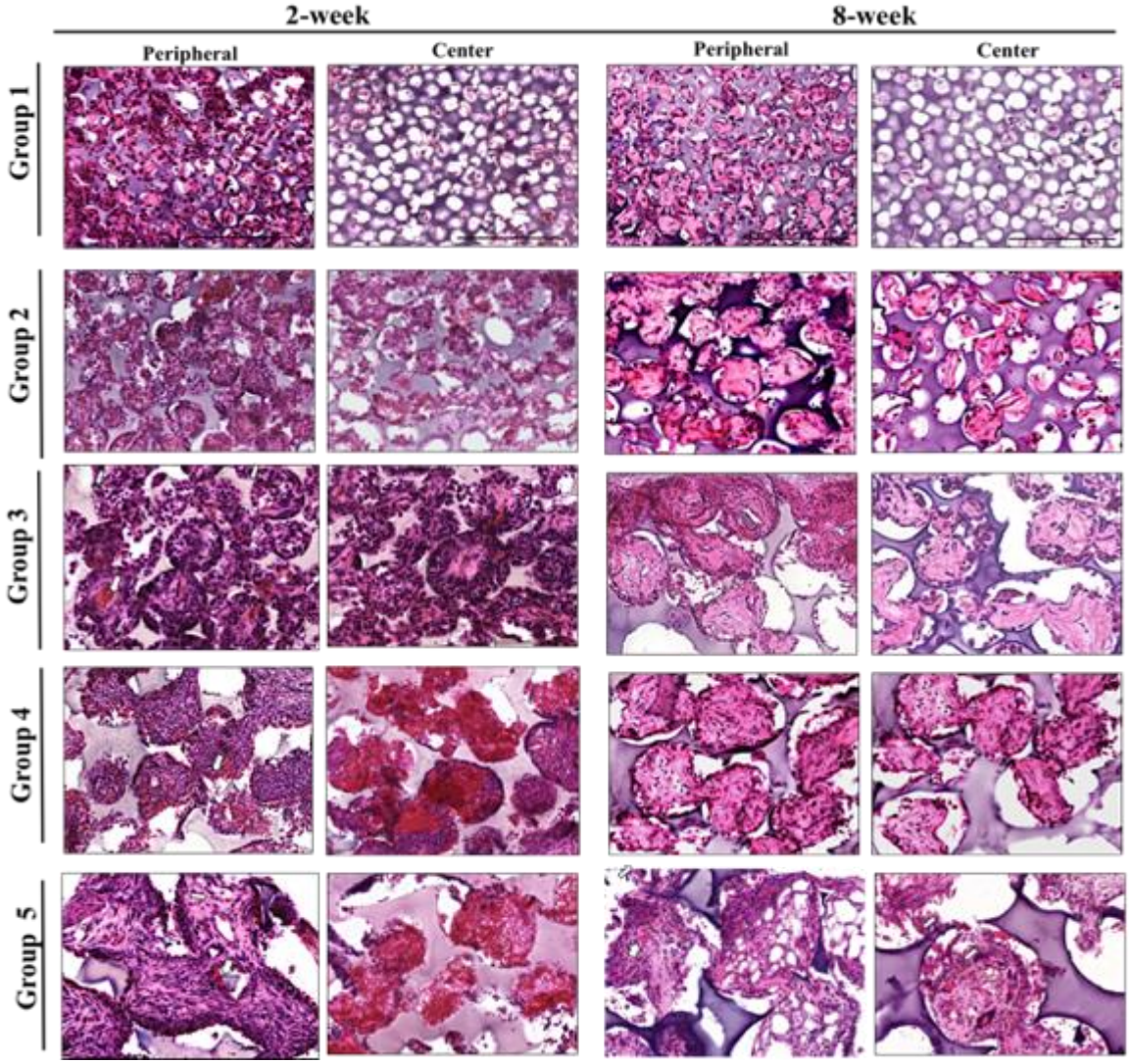

Figure 12: Morphological assessment of bone formation within critical-sized cranial defects. Hematoxylin and Eosin (H&E) staining of excised scaffolds at 2 weeks and 8 weeks post-implantation for all groups, left panel shows peripheral area of the scaffold, and right panel shows center region of the scaffold. Scale bars: 200 μm.

3.3.5 Vascularization of implanted grafts

As evident from Figure 11, the H&E staining of the tissue sections following 2 weeks of implantation showed vascular connections throughout the implant and at the

defect interface with the native bone, suggesting formation of anastomosed vessels with the host. The formation of vasculature was further confirmed by staining for platelet endothelial cell adhesion molecule (PECAM-1) (Figure 14). Groups treated with mineralized and non-mineralized macroporous matrices revealed the presence of PECAM-1-positive cells within the defect at 2- and 8-week post-implantation (Figure 13). In contrast, tissue sections of sham groups showed no evidence of vascularization throughout the defect site.

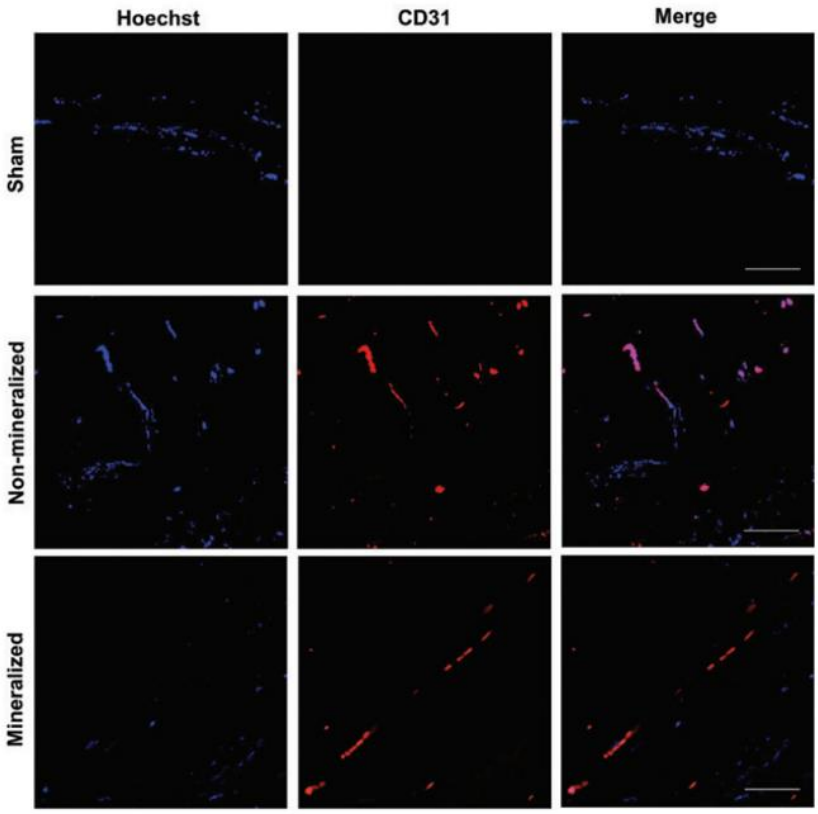

Figure 13: Vascularization of the defect following 2 weeks of implantation. Immunofluorescent staining for platelet endothelial cell adhesion molecule (CD31) and Hoechst 33342 staining of cell nuclei within the defect site for sham, non-mineralized, and mineralized cryogel groups. Scale bars: 100 μm.

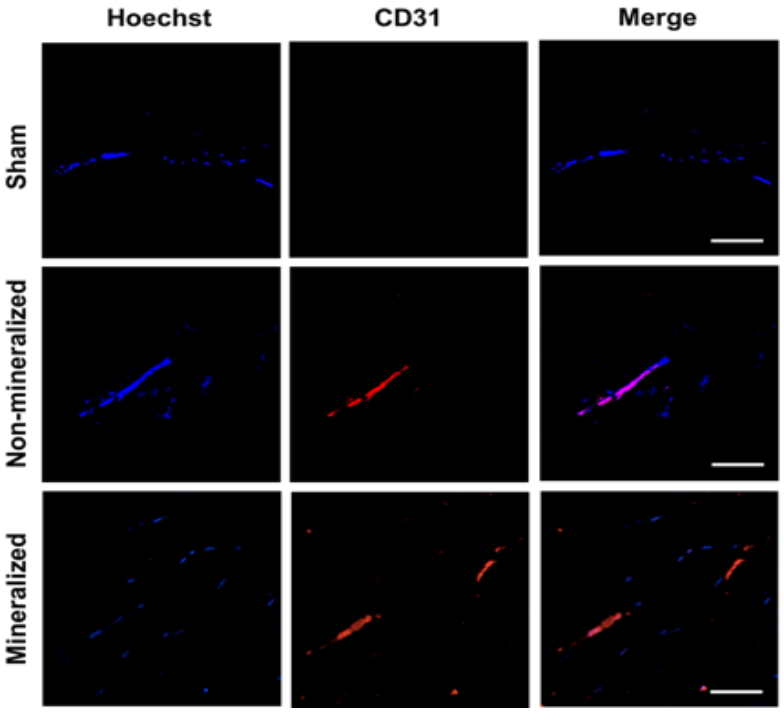

Figure 14: Vascularization of the defect following 8 weeks of implantation. Immunofluorescent staining for platelet endothelial cell adhesion molecule (CD31) and Hoechst 33342 staining of cell nuclei within the defect site for sham, non-mineralized, and mineralized cryogel groups. Scale bars: 100 μm.

Furthermore, scaffolds with different pore size demonstrate varying degree of vascularization. At 2 weeks post-implantation, presence of vasculature was observed in scaffold with pore size larger than 150-180um (Group 3 above), with presence of red blood cells, indicating formation of anastomosed vessels with the host. The presence of vasculature was further confirmed by staining for platelet endothelial cell adhesion molecule (PECAM-1) (Figure 15). By the end of 8 weeks, group 1-2 showed vascularization only at the peripheral area whereas group 3-5 had vascularization within the implant, with more vascularization observed in larger pore size group.

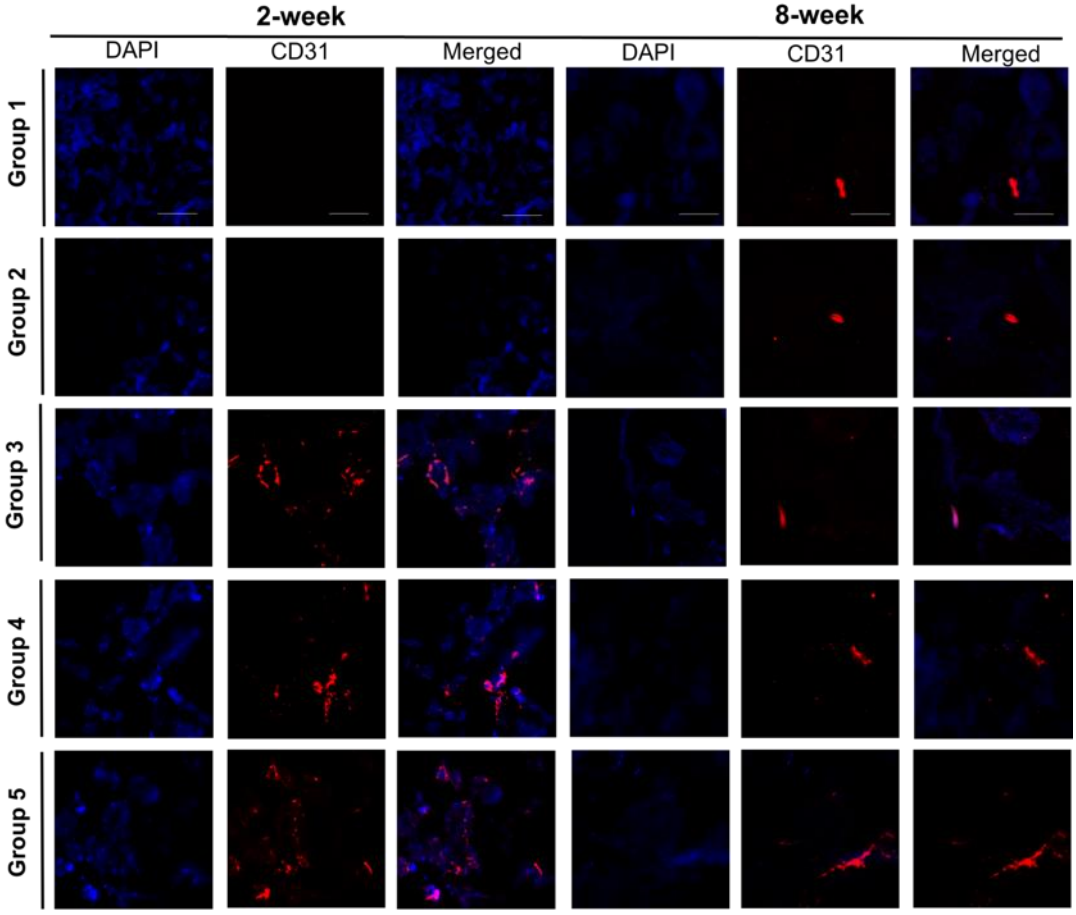

Figure 15: Vascularization of mineralized scaffold 2- and 8-week post-implantation. Immunofluorescent staining for platelet endothelial cell adhesion molecule (PECAM-1; CD31) and Hoechst 33342 staining of cell nuclei within the mineralized scaffold in all groups following 2 and 8 weeks of implantation. Scale bar: 100 μm.

3.3.6 Histology and Immunostaining

For the cranial defect study, to further confirm the bone tissue formation, the tissue sections were stained for osteocalcin, a bone-specific matrix protein that is secreted by osteoblasts (Figure 16A,B and Figure 17A,B). At 2 weeks, groups treated with mineralized cryogels showed presence of ECM enriched with osteocalcin (Figure

17A, B). A similar finding was also observed after 8 weeks of post-implantation (Figure 16A). These findings are further shown by histogram intensity of the images, in which lower histogram values indicate higher osteocalcin expression (Figure 16B). In contrast, defects treated with non-mineralized cryogels showed minimal presence of osteocalcin at the defect site, at both 2- and 8-week post-implantation. The fibrous-like tissue bridging the defect site of sham groups was found to have some, but less, osteocalcin deposition at both 2- and 8-week posttreatment. After 2 weeks of implantation, the mineralized group, but not the sham and non-mineralized group, showed BMP2 expression, a protein commonly involved during osteogenesis (Figure 17C, D).

TRAP staining was performed to examine the presence of osteoclast-like cells within the neo-bone tissue (Figure 16C,D and Figure 17E, F). TRAP-positive cells were detected in both the defects treated with mineralized and non-mineralized cryogels at 2 weeks post-implantation (Figure 17E, F). Following 8 weeks of treatment, an increase in TRAP-positive cells was observed in defects treated with mineralized cryogels, but none was detected for groups treated with non-mineralized cryogels(Figure 16C). No TRAP-positive cells were observed for sham groups at both 2- and 8-week post-procedure. Quantification of TRAP staining at 8 weeks posttreatment corroborated aforementioned observations (Figure 16D). To further confirm the presence of osteoclasts, receptor activator of nuclear factor κB (RANK) expression, a marker of osteoclasts, was positive

in the mineralized, but not sham and non-mineralized groups after 2 weeks post-implantation (Figure 16E,F).

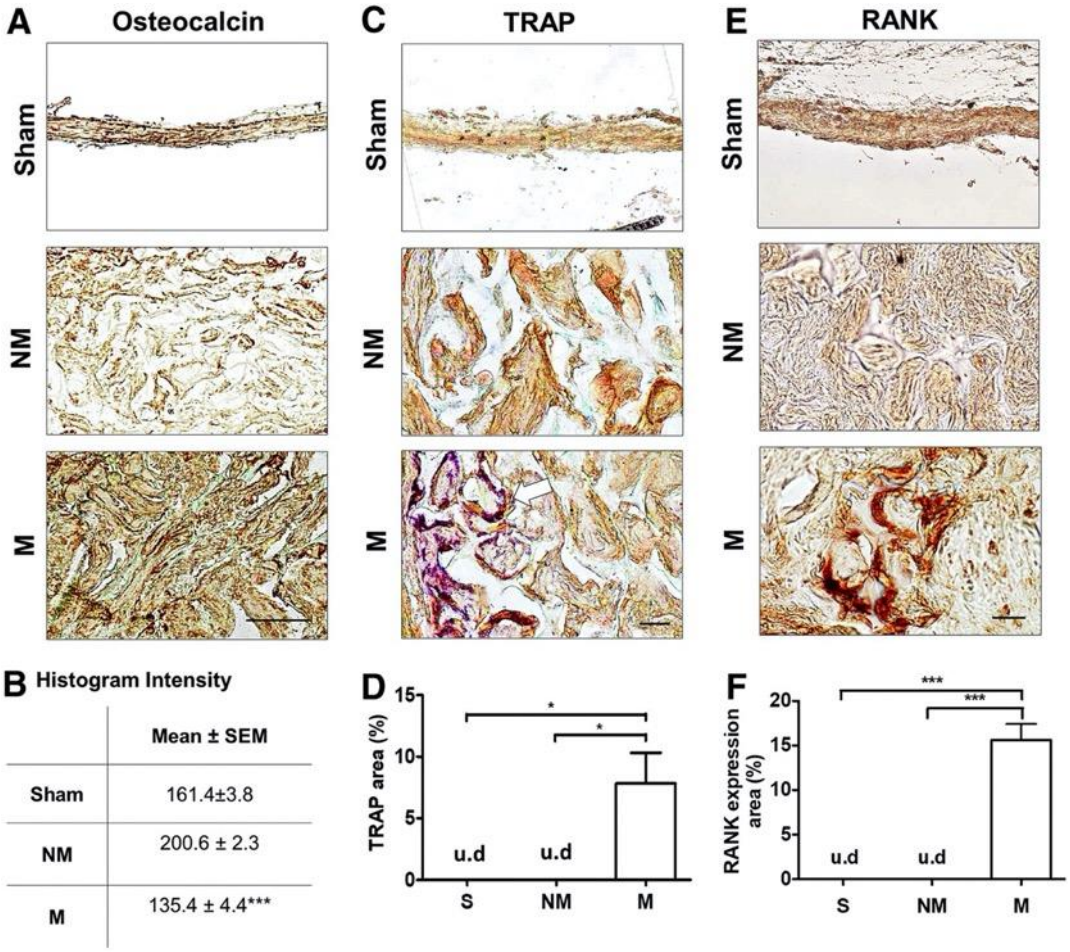

Figure 16: Bone-specific markers in newly formed tissue within cranial defects at 8 weeks after implantation.A) Immunohistochemical staining of osteocalcin for sham (S), non-mineralized (NM), and mineralized (M) groups and (B) mean histogram intensity of images following 8 weeks of implantation. Lower intensity values correspond to higher expression. (C) Histochemical staining for TRAP and (D) percent positive area of the cranial defect site for sham (S), non-mineralized (NM), and mineralized (M) treatment groups following 8 weeks of implantation. *Arrow* indicates TRAP-positive cells found within the constructs. (E) Histochemical staining for RANK and (F) percent positive area of the cranial defect site for sham (S), non-mineralized (NM), and mineralized (M) treatment groups following 8 weeks of implantation. Scale bars:30 μm. Asterisks denote p values with statistical significance

(*$p < 0.05$, ***$p < 0.001$). RANK, receptor activator of nuclear factor κB; TRAP, tartrate-resistant acid phosphatase; u.d, undetectable.

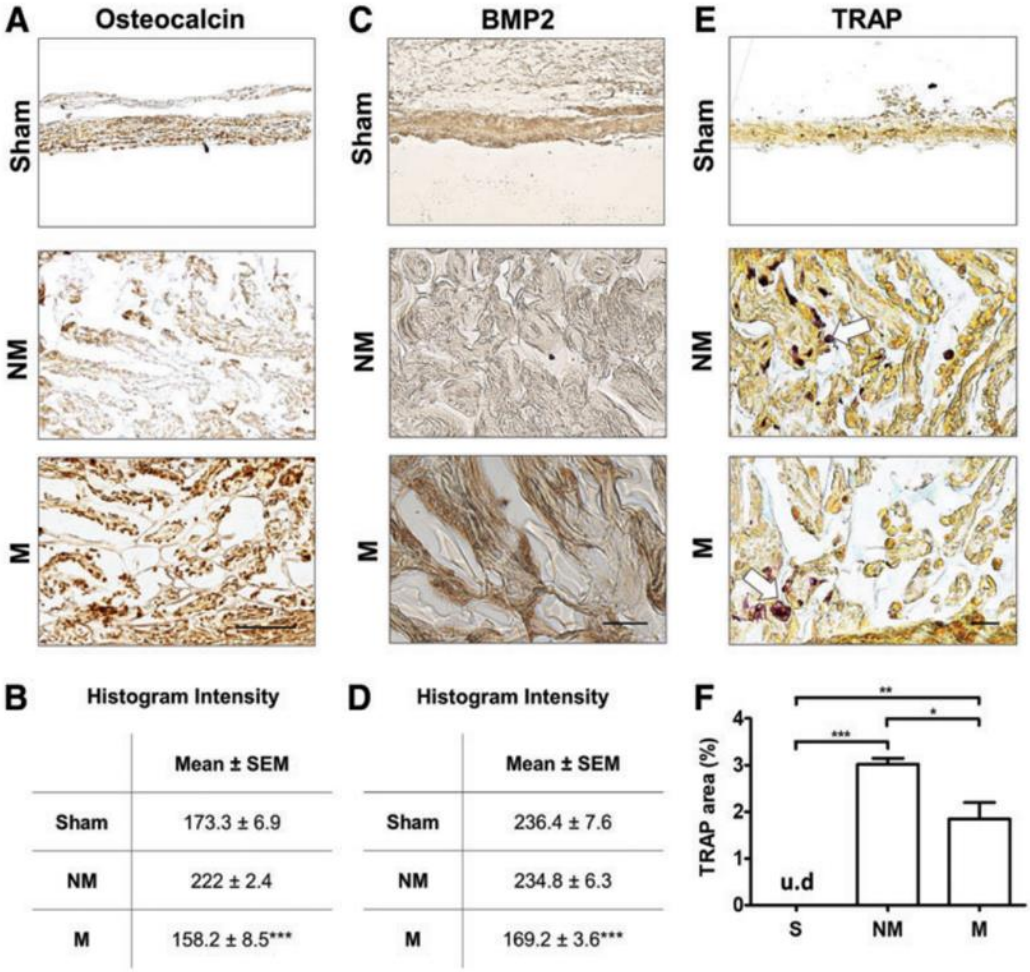

Figure 17: Bone specific marker evaluation at 2 weeks after implantation. (A) Immunohistochemical staining of osteocalcin for sham (S), non-mineralized (NM), and mineralized (M) groups and (B) mean histogram intensity of images following 2 weeks of implantation. Lower intensity values correspond to higher expression. (C) Histochemical staining for tartrate-resistant acid phosphatase (TRAP) and (D) quantification of percent positive area of the cranial defect site for sham (S), non-mineralized (NM), and mineralized (M) treatment groups following 2 weeks of implantation. Arrows indicate TRAP-positive cells found within the constructs. (E) Histochemical staining for BMP2 and (F) Mean histogram intensity of the cranial defect site for sham (S), non-mineralized (NM), and mineralized (M) treatment groups following 2 weeks of implantation. Arrows indicate TRAP-positive cells found within

the constructs. Scale bars: 30 mm. Asterisks denote p values with statistical significance (*p < 0.05, **p < 0.01, ***p < 0.001). u.d: undetectable.

For the pore size study, immunohistochemically staining of osteocalcin (OCN) and bone morphogenetic protein 2 (BMP-2) showed ECM enriched with OCN and BMP-8 weeks post-implantation (Figure 18). The expression of OCN increased as the pore size increased. For BMP-2 staining, Group 4-5 showed least expression whereas group 1, 2, and 3 showed moderate expression of BMP-2.

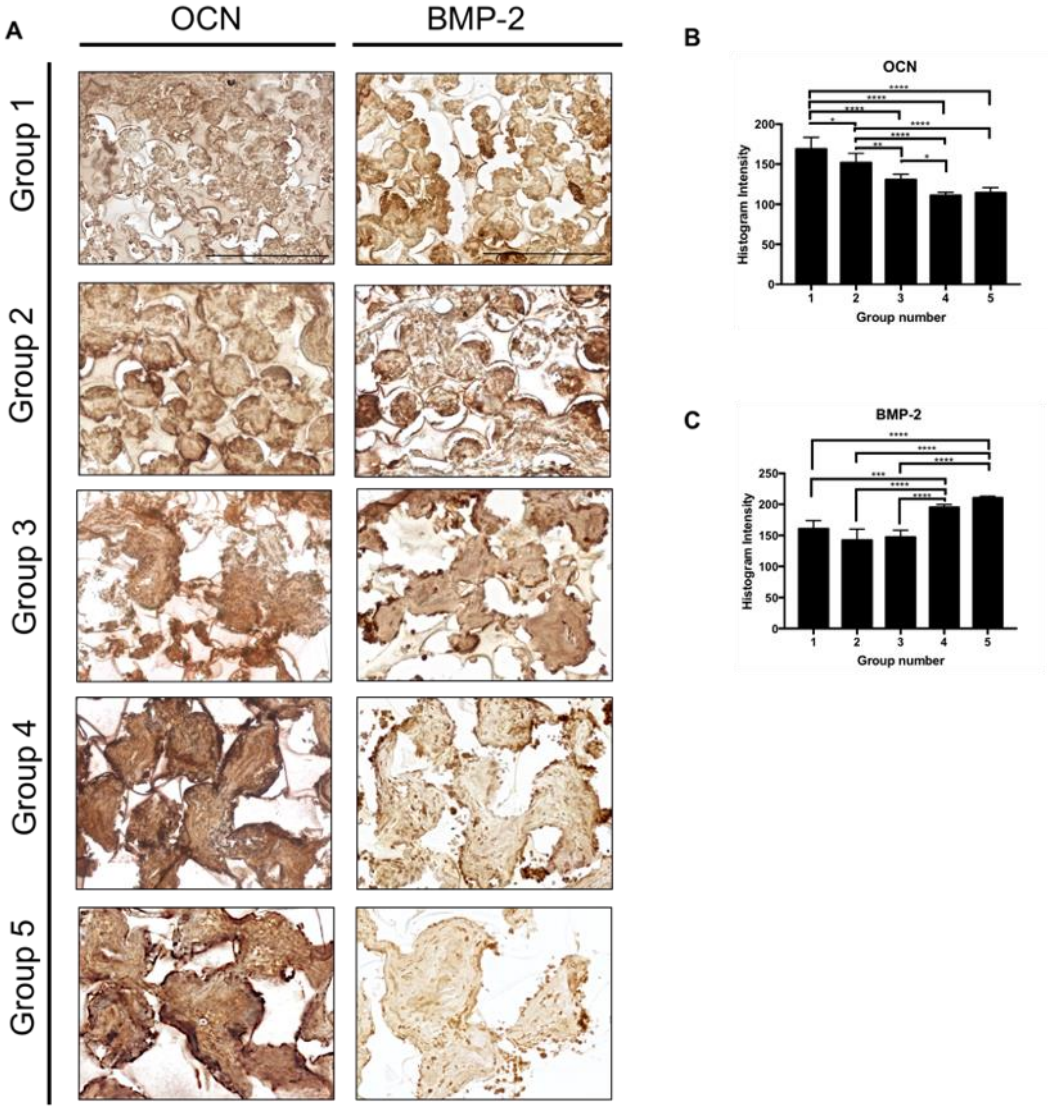

Figure 18: Bone-specific markers in newly formed tissue within cranial defects 8-week post-implantation. (Left column): immunohistochemical staining of osteocalcin for biomineralized scaffold following 8 weeks of implantation; (right column): histochemical staining for BMP-2 of the cranial defect site following 8 weeks of implantation. Scale bars: 100 μm.

3.4 Discussions

In this chapter, I evaluated the potential of macroporous, mineralized biomaterials to stimulate bone healing in the absence of exogenous biologicals by using a critical-sized cranial defect as a model system. Results from the studies show that mineralized macroporous matrices promoted hard tissue formation that led to complete healing of the cranial defect by 8 weeks post-implantation. Histological analysis of the defects revealed extensive host cell infiltration within both non-mineralized and mineralized cryogels. This suggests that cell infiltration is a consequence of the macroporous nature of the scaffolds, which supported homogeneous distribution of the host cells throughout the implant. The μCT analyses along with the osteocalcin staining suggest that despite the widespread cell infiltration, only cells within the mineralized materials contributed to the formation of bone-forming cells and hard tissue formation, highlighting the importance of the mineral environment in promoting osteogenic differentiation of recruited cells, and to bone tissue formation. These *in vivo* findings are consistent with the *in vitro* findings, where the importance of CaP minerals in directing osteogenic differentiation of stem cells have been demonstrated.[52-54,56] It has been showed previously that these mineralized scaffolds when implanted in the subcutaneous space of a rat, recruited endogenous cells to form bone tissue.[77]

For scaffolds with varying pore sizes, histological evidence of the excised implants suggests that implants with pore size greater than 150-180 μm supported more

homogenous cell infiltration and subsequently more bone tissue formation within the implants, and a pore size under 100 μm allowed very little bone formation inside the implant. A number of studies have shown that cell migration and proliferation were affected by scaffold pore size [190-193]. The larger pores reduced cell aggregations along the edges of the scaffold promoting cell proliferation and migration into the center of the scaffold. Cell attachment, migration and speed are influenced by specific integrin–ligand interactions between the cell and the surrounding ECM, making it crucial to maintain a high surface area in scaffolds for optimal osteoconductivity. In this study, although scaffolds with smaller macropores had larger pore surface areas, their osteoconductivity was impaired by limited cellular infiltration at the early time point. The effects of larger surface area were overcome in larger pores by the importance of cell migration and proliferation as was seen histologically in Groups 3-5. Besides cell migration, studies have shown that proliferation of osteoblasts was also affected by pore size of the scaffold [192,193]. The mechanical behavior of the scaffolds showed considerably less sensitivity to pore size than the biological ingrowth. All of the scaffolds possessed very low stiffness (about 0.05 MPa) and compressive strength values in the 0.04 to 0.5 MPa range. The porous scaffolds are quite deformable, capable of more approximately 70% compressive strain without fracture. The low stiffness of the scaffolds would result in very large deformations and pore collapse even at moderate loads. This pore collapse under load would presumably influence the bony ingrowth properties of the scaffold if it was

placed alone in a linear load bearing segmental defect or across an open fusion site. On the contrary, in low load bearing defects surrounded by structural bone, this low stiffness would not be an issue. Further work is needed to understand how the scaffolds would behave in a load bearing environment, and what reinforcement would be necessary to facilitate the same growth behavior under monotonic and cyclic loading conditions.

Concomitant with the cell infiltration, only the groups with pore sizes greater than 150 μm showed the presence of intraluminal red blood cells, which suggests that neo-vessel formation was only permitted in pore sizes larger than 150 μm. Furthermore, vascularization was also positively correlated with the volume of newly formed bone deposited within the implanted scaffolds. The repair of bone defects with biomaterials depends on sufficient vascularization of the implantation site. Angiogenesis, which ultimately leads to functional vascularization, is crucial for bone formation and for the substitution of biomaterials with osseous tissue. Porous bone substitutes permit vessel ingrowth and thus facilitate osteogenesis. Previously, studies have illustrated the role of scaffold pore size in vascularization [194,195]. The findings of our study were consistent with the previous results, where vascularization was enhanced in the larger pore sizes

The physicochemical properties of the mineralized scaffold play a key role in supporting osteogenic differentiation of progenitor cells and bone tissue formation. For instance, previous studies have shown that the dissolution properties of calcium

phosphate minerals could contribute to the osteoinductive ability of biomaterials. Higher osteoinductive potential was observed with scaffolds containing resorbable biphasic calcium phosphate and β-TCP compared to hydroxyapatite.[196,197] Recently, we have shown that the CaP minerals present in the mineralized materials readily dissociate into Ca^{2+} and PO_4^{3-} ions and modulate their concentration in the extracellular milieu.[56,57] Both extracellular Ca^{2+} and PO_4^{3-} play a key role in promoting osteogenic differentiation of stem cells.[56,198-202]

Combined and coordinated action of osteoblasts and osteoclasts is essential to maintain bone homeostasis. It is therefore necessary that engineered bone grafts provide a permissive environment for bone remodeling to take place. Although TRAP-positive cells were observed in defects treated with both mineralized and non-mineralized cryogels after 2 weeks treatment, their presence at 8 weeks was observed only in groups treated with mineralized cryogels. TRAP-positive cells detected in the non-mineralized groups at 2 weeks suggest that monocytic/osteoclast precursors possibly migrated from the surrounding bone[36] and contributed to TRAP positivity in the grafts, while the non-calcified environment lacking osteoblasts and their secreted factors does not support their continued activity at 8 weeks.[203-205] In addition to neo-bone tissue formation, successful healing of bone defects requires vascularization and anastomosis of the implant with the host tissue. [205 206] Our results demonstrate that the macroporous architecture of our scaffold facilitated the infiltration of host cells as well as

vascularization of the implant. Prior studies have also shown the influence of bone-residing osteoblasts in angiogenesis by secreting vascular endothelial growth factor A.[207,208]

The expression of BMP-2 and OCN at 8 weeks post-implantation in the groups with pore sizes greater than 200 μm (Groups 4-5) showed distinguished patterns compared to those below 200 μm (Groups 1-3). Groups 4-5 exhibited higher BMP-2 expression and lower OCN expression of compared to Groups 1-3. As a bone-specific extracellular matrix protein, OCN is a marker of mature osteoblasts [209] while BMP-2 is involved in activating immature mesenchymal cells for osteoblastogenesis [210]. Therefore, low BMP-2 expression and high OCN expression could indicate the maturation of osteoblasts in the groups with pores sizes greater than 200 μm.

The osteocondctive/inductive function of the mineralized materials could be attributed to the dissociation of CaP mineral phase into Ca^{2+} and PO_4^{3-} ions. These extracellular Ca^{2+} and PO_4^{3-} ions play a key role in promoting osteogenic differentiation of stem cells [56,198,200-202,211]. Due to the increase of their local concentrations, the released Ca^{2+} and PO_4^{3-} ions could also lead to spontaneous precipitation of calcium phosphate [57]. This process is usually accompanied with co-precipitation of osteoinductive factors such as bone morphogenic proteins [44,45,47,196,197],. These proteins have high affinity to apatite-like calcium-phosphate phase [44,45,47,196,197], which was shown to resemble the CaP minerals

present in our biomineralized scaffold. Therefore, sequestration of osteoinductive factors on the scaffold could further promote formation of bone tissue within the defect site.

In summary, as the need to develop simple treatment strategies that are reliable and cost-effective has become increasingly important, the studies described here demonstrate that mineralized macroporous biomaterials alone are sufficient to promote the formation of functional bone tissue and achieve complete healing of bone defects. While the macroporous structure of the scaffold enabled infiltration of host cells, the osteogenic differentiation of recruited cells and maintenance of osteoblasts required the presence of mineral environment. The newly formed tissue, although appears to be immature at 8 weeks post-implantation time, recapitulated many key characteristics of native bone tissue such as presence of bone-forming osteoblasts and TRAP-expressing osteoclasts, as well as vascular networks. Such approaches involving synthetic biomaterials that not only support bone formation but also facilitate vascularization solely by recruitment of host progenitors, without the need of exogenous donor cells and growth factors provide an attractive alternative to current therapeutic strategies involving osteoinductive growth factors and bone tissue derivatives.

3.5 Conclusions

The work in this chapter demonstrates the ability of mineralized, macroporous biomaterials to direct bone healing of critical-sized cranial defects. By providing a bone-specific mineral environment, these biomaterials induce osteogenic commitment of

recruited host progenitor cells and support the maintenance of cells relevant for the formation and function of bone tissues, resulting in the formation of mature, vascularized bone tissue and complete healing of the defects.

Furthermore, this chapter shows that pore size is a critical parameter governing the dynamic processes of cell infiltration, vascularization, and osteo-ingrowth of the mineralized macroporous hydrogels. I found that pore diameter greater than 100 μm is essential for cell infiltration and vascularization within the scaffolds, which ultimately dictates the materials-mediated neo bone tissue formation.

4. Chapter 4: Elucidate Effects of Host Age on Endogenous Cell Mediated Bone Tissue Formation

The strategies of *in situ* bone tissue engineering depend not only upon the properties of materials, but also on the cellular environment and reparative capabilities of the host tissue environment. Aging is one of the most importance factors that cause significant changes in tissue repair ability. To this end, the work of Chapter 4 studies the effect of physiological age of host on the biomineralized materials-mediated bone tissue formation with a mouse critical-sized cranial defect model. The findings from this chapter suggests that biomineralized materials able to aid almost-complete healing of the defects, and this bone healing process was highly dependent upon the age of the host.

As the first author of the manuscript serving as the basis for this chapter, I oversaw and was involved in all aspects of this research, including experimental planning, writing, figure preparation, and editing in conjunction with my co-authors Yu-Ru V. Shih, Manando Nakasaki and Shyni Varghese.

4.1 Introduction

As described earlier in this dissertation, biomineralized macroporous materials containing calcium phosphate minerals shows great potentials to support bone tissue regeneration *in vivo* and *in vitro*[53-55,77,212,213]. While physical (e.g. pore size) and chemical (e.g. osteoinductivity) properties of the scaffolds play a key role in the recruitment of

endogenous cells and their function (including osteogenic differentiation), a number of host-specific parameters such as the age of the recipients could be an important factor in determining the treatment outcome. It is very well documented that tissue repair abilities decline with age and bone healing is no exception. Studies have shown a decline in bone healing capacity in the elderly [214-217]. Such a decline in tissue repair has been touted to be associated with multiple age-related alterations of cellular activities and microenvironment in the body, including decreased number and/or function of stem cells [218,219], structural and cellular changes in periosteum [220,221], changes in the local signaling at injury site [222], and rate of vascularization [215]. Thus, it is crucial to gain a better understanding of the effect of physiological age of the host tissue on biomineralized material-mediated bone tissue repair *in vivo*.

In this chapter, I investigated the effect of the host age on biomineralized material-mediated bone tissue repair by employing mice of varying ages (1, 2, 6, and 14-month-old). We used critical-sized cranial defects as a model system and assessed biomaterial-mediated recruitment of host cells and bone tissue formation as a function of post-implantation time. While almost complete closure of defects was achieved in all ages by 8 weeks post-implantation, significant differences, in terms of pace of healing and extent of neo-bone tissues and mineral depositions, were observed.

4.2 Materials and Methods

4.2.1 Graft synthesis and mineralization

Synthesis of poly (ethylene glycol) diacrylate (PEGDA) [Mn (number-average molecular weight) = 3.4 kDa] and N-acryloyl 6-aminocaproic acid (A6ACA) was performed as previously reported [76,127]. Macroporous copolymer hydrogels of PEGDA and A6ACA (PEGDA-co-A6ACA) were prepared through cryogelation as described elsewhere [77]. Briefly, a precursor solution containing 20% (w/v) PEGDA and 0.5 M A6ACA, 0.5% (w/v) ammonium persulfate (APS) and 0.2% (v/v) N, N, N′, N'-tetramethylethylenediamine (TEMED) were prepared in 0.5 M NaOH. A drop of 75 μL precursor solution was dispensed into a pre-chilled polystyrene petri-dish. A pre-chilled circular glass coverslip of 15 mm in diameter was then put onto the precursor solution, and the solution was allowed to polymerize at −20°C for 24 hours. After gelation, PBS at room temperature was added into the petri-dish to facilitate thawing of the ice crystals, thus yielding an interconnected macroporous structure. The resultant macroporous hydrogels (i.e. cryogel) were subsequently punched into disks of 4 mm in diameter and 0.7 mm in height. Mineralization of the macroporous scaffold was achieved by incubating the cryogel structures in simulated body fluid (m-SBF) for 12 h and, subsequently, in 40 mM Ca^{2+} and 24 mM PO_4^{3-} (pH 5.2) for 1 h [35]. m-SBF was prepared as detailed previously by Oyane *et al*. [23]. Briefly, 1 L of a HEPES−NaOH buffered solution (pH 7.4) was prepared containing 142 mM Na^+,103 mM Cl^-, 10 mM HCO_3^-, 5 mM K^+, 1.5

mM Mg^{2+}, 1.0 mM HPO_4^{2-}, and 0.5 mM SO_4^{2-}, 2.5 mM Ca^{2+}. Prior to usage, the solution was warmed to 37 °C. The scaffolds were briefly rinsed in ultrapure water, followed by incubation in m-SBF for 48 h at 37°C. After the complete biomineralization, the mineralized scaffolds were sterilized by incubating in 70% ethanol for 3 hours, followed by rinsing with sterile PBS for 3 days.

4.2.2 Calcium and phosphate assays

Calcium and phosphate assays were performed to determine the amount of Ca^{2+} and PO_4^{3-} in the biomineralized scaffolds and their release to the surrounding medium. The scaffolds were rinsed and homogenized in ultrapure water. The homogenized scaffolds were freeze-dried, and their dry weights were recorded. Dried scaffolds were incubated in 0.5 M HCl at 25°C. Incubation medium was collected after 3 days, which was sufficient to dissolve all the minerals from the scaffolds, and the amount of $Ca^{2+}$and PO_4^{3-} was measured.

To assess dissolution of Ca^{2+} and PO_4^{3-} from the mineralized scaffolds and their release to the surrounding medium, dried scaffolds were rehydrated and equilibrated in ultrapure water. After reaching the equilibrium swollen state, the scaffolds were incubated in 1 M Tris-HCl (pH = 7.4), free of these ions, at 37 °C for 7 days. Incubation solution was collected and replaced with fresh medium daily. The collected incubation solution was used to determine the release of Ca^{2+} and PO_4^{3-} ions from the scaffolds.

A calcium assay was conducted based on the manufacturer's protocol (Calcium reagent set, Pointe Scientific, catalog number: C7503) as described previously [52]. Briefly, 20 μL of the sample solution was mixed with 1 mL of assay solution containing o-Cresolphthalein complexone (CPC). The absorbance of the mixture solution was measured at 570 nm by a UV/Vis spectrophotometer (Beckman Coulter, DU 730). The Ca^{2+}concentration was computed from a standard curve generated for a concentration range of 0-4 mM Ca^{2+}.

A phosphate assay was conducted as detailed elsewhere [188]. Briefly, an assay solution was prepared by mixing 1 volume of 10 mM ammonium molybdate, 2 volumes of acetone, and 1 volume of 5 N H_2SO_4. One mL of this assay solution was mixed with 125 μL of the sample solution. To this, 100 μL of 1M citric acid was added. The absorbance at 380 nm of the resultant product was determined by a UV/Vis spectrophotometer. The PO_4^{3-} concentration was computed from a standard curve generated for a concentration range of 0–4 mM PO_4^{3-}.

4.2.3 Scanning electron microscopy (SEM) and energy dispersive spectra (EDS)

Scanning electron microscopy (SEM) was used to examine the pore structures of the mineralized scaffolds. The scaffolds were cut into thin slices, followed by freeze-drying for 24 h. These samples were sputter coated (Emitech, K575X) with iridium for 7 s and imaged using SEM (Philips XL30 ESEM). The mineral composition of the scaffolds

was determined through EDS analysis. ICA software was used to quantify the calcium to phosphate atomic ratio (Ca/P) from the resulting elemental spectra.

4.2.4 Surgical procedures and biomaterial implantation

For the *in vivo* studies, female C57BL6/J mice (1, 2, 6 and 14-month-old) were used. All animal studies were performed in accordance with the Institutional Animal Care and Use Committee (IACUC) at the University of California, San Diego and National Institutes of Health (NIH). In preparation for surgery, mice were anesthetized using ketamine hydrochloride (Ketaset, 100 mg/kg), xylazine (AnaSed, 10 mg/kg) and buprenorphine (0.05 mg/kg) via intraperitoneal injection.

A skin incision was made along the length of the calvaria to expose the parietal region and a 4 mm-diameter defect was made in both the left and right parietal bones with a 4-mm biopsy punch [187]. For the experimental group, sterile mineralized scaffolds were transplanted into each defect site. Groups with untreated defects were used as sham groups. Following implantation, the skin was sutured and mice were kept on a warm heating pad until wakening. After the surgery, all the mice were kept in separate housing cages. The ability of the mineralized biomaterials to support neo-bone tissue formation were compared against groups with untreated defects. The bone tissue formation within the bone defects were analyzed at 2- and 8-week post-procedure.

4.2.5 Micro-computed tomography (μCT)

Micro-computed tomography (μCT) was performed to assess hard tissue formation within the cranial defect at 2- and 8-week post-implantation. The entire skull of each mouse was harvested and fixed in paraformaldehyde (PFA) by immersing the specimens in 4% PFA for 4 days at 4°C. The retrieved samples were rinsed with PBS and secured tightly between styrofoam disks within a conical tube. Scanning was performed using SkyScan 1076 (Bruker: 9 μm/pixel, 50 kV, 0.5 mm Al filter). Scan reconstruction was performed using the NRecon software (SkyScan, Bruker). Using CT Analyzer software (SkyScan, Bruker), cranial bone tissues were segmented using a threshold of 90-255. The reconstructed images were used to generate 3-D models by using CT Analyzer software (SkyScan, Bruker). Bone mineral density (Bone volume/Total volume, BV/TV) was quantified from the reconstructed images.

4.2.6 Histology and immunohistological staining

The PFA fixed samples were decalcified by using 10% ethylenediaminetetraacetic acid (EDTA, pH 7.4), where the samples were incubated in the solution for 2 weeks at 4°C. The decalcified samples were gradually dehydrated with increasing concentration of ethanol and equilibrated in CitriSolv. Following dehydration, samples were incubated in a mixture of 50% (v/v) CitriSolv, 50% (v/v) paraffin for 30 min at 70°C. The samples were then embedded in paraffin and sliced into sections of 10-μm thickness using a rotary microtome (Leica, RM2255). Before staining, the sections were deparaffinized

using CitriSolv and subsequently rehydrated with decreasing concentration of ethanol until the samples were equilibrated with deionized (DI) water.

Hematoxylin and eosin (H&E) staining was performed by incubating the rehydrated samples in hematoxylin solution for 2 minutes (Ricca, catalog no. 3536-16), followed by eosin-Y solution (Richard-Allan Scientific, catalog no. 7111) for 20 seconds. The stained sections were dehydrated, mounted and imaged using a Keyence microscope (BZ-X700).

Histomorphometric analysis was conducted to evaluate the quantity of the neo-bone tissue. Six H&E images of each defect were randomly selected and areas of the newly formed bone tissues resembling the morphology of native bone were identified. The total area of the newly formed bone tissue, as well as the total defect area, were analyzed using ImageJ. The mean areal density of the newly formed bone was presented as the fraction of bone area per defect area.

Osteoclasts were detected by the tartrate-resistant acidic phosphatase (TRAP) staining. Briefly, The TRAP incubating solution was prepared by first mixing 50 μL of Fast Garnet GBC base solution with 50 μL of sodium nitrite solution. This mixture was added to 4.5 mL of pre-warmed DI water at 37°C. After mixing, 50 μL of Naphthol AS-BI phosphate solution, 200 μL of acetate solution, and 100 μL of tartrate solution were added and mixed to generate a working solution. Rehydrated sections were immersed in the working solution, incubated at 37°C for 1 h in dark, and rinsed with DI water.

After staining, the sections were dehydrated with increasing concentration of ethanol and finally with CitriSolv until equilibrium was reached. Slides were mounted with glycerol and imaged immediately. Quantification of TRAP-positive staining was performed using ImageJ. The mean areal density of TRAP-positive area was presented as the percentage of total TRAP-positive area over total tissue area.

For immunohistochemical and immunofluorescent staining, rehydrated sections were immersed in a solution of proteinase K (20 μg/mL; Invitrogen, catalog #1000005393) in 95% (v/v) TE buffer (50 mM Tris-HCl, 1mM EDTA, and 0.5% [v/v] Triton X-100; pH 8) with 5% (v/v) glycerol and incubated for 15 min at 37°C. For immunohistochemical staining, sections were incubated in a blocking buffer containing 3% (w/v) bovine serum albumin (BSA) for 1 h at 25°C. Samples were incubated with primary antibody against osteocalcin (OCN) (1:100, rabbit polyclonal, Abcam, catalog#ab93876), or BMP-2 (1:100, rabbit polyclonal, Abcam, catalog #ab1493) in blocking solution for 9 h at 4°C. Sections were rinsed with PBS and treated with 3% (v/v) hydrogen peroxide for 7 min at 25°C. The samples were then incubated with secondary antibody (1:100, horseradish peroxidase-conjugated donkey anti-rabbit, Jackson ImmunoResearch, catalog #711-035-152) in a blocking solution for 1 h at 25°C. The treated sections were rinsed with PBS and developed by immersion in 3,3'-diaminobenzidine (DAB) substrate solution (Vector Laboratories, catalog #SK-4100) for 1 min at 25°C. The sections were washed with PBS and gradually dehydrated using

increasing concentrations of ethanol and incubated in CitriSolv until equilibrium was reached. Slides were mounted and imaged immediately. For immunofluorescent staining, sections were washed with PBS and permeabilized using 0.1% Triton X-100 for 10 min at 25°C, which were then treated with sodium borohydride solution (2.5 mg/mL in 50% [v/v] ethanol) for 30 min at room temperature. The sections were immersed in a blocking solution (3% [w/v] BSA and 0.1% [v/v] Triton X-100) and incubated for 1 h at 25°C. Sections were then incubated with primary antibody against CD31 (Platelet endothelial cell adhesion molecule [PECAM-1], 1:100, goat Santa Cruz Biotechnology, catalog #sc-1506) in a blocking buffer for 12 h at 4°C and rinsed with PBS.

The immunohistochemical (IHC) and immunofluorescent staining were analyzed using ImageJ. For IHC staining, the expression of the markers was represented using mean histogram intensity as described earlier [189]. Histogram intensity ranges from 0-255, with 255 representing white (lightest) and 0 representing black (darkest), indicating that the higher the histogram intensity, the lower the expression of the marker. For immunofluorescent staining, the mean areal percentage of the CD31-positive region was presented as percentage of total CD31-positive area over total defect area.

4.2.7 Statistical Methods

Each experiment used 5 biological replicates (n=5) and repeated at least twice to independently verify the findings. GraphPad Prism 7 software was used to perform statistical analysis of the data. Two-tailed Student's t-test was applied when comparing

two groups at the same time point. One-way analysis of variance (ANOVA) with Tukey-Kramer post-hoc test was used for comparisons between multiple groups within the same time point.

4.3 Results

4.3.1 Fabrication and Characterization of mineralized biomaterials

Macroporous cryogels made of PEGDA-co-A6ACA were used for the studies. The SEM images showed macroporous architecture of the mineralized scaffold networks composed of randomly oriented, interconnected macroporous structures measuring approximately 80-200 μm(Figure 19A). The cryogels were mineralized to incorporate calcium phosphate moieties, where the carboxyl functional groups of the A6ACA moieties bind to Ca^{2+} and initiate nucleation and growth of mineral crystals. The bound minerals of the scaffold showed a flat, plate-shaped morphology (Figure 19B). EDS analysis further confirmed the presence of CaP minerals within the mineralized scaffolds and the calcium (Ca^{2+}) to phosphate (PO_4^{3-}) (Ca/P), ratio was estimated to be 1.5 (Figure 19C). As anticipated, both Ca^{2+} and PO_4^{3-} were released from the mineralized scaffolds and showed similar release profiles (Figure 19D-E). Each biomineralized scaffold contained a total amount of 102.65 ± 2.91 mg/g of Ca^{2+}, and 155.32 ± 8.90 mg/g of PO_4^{3-} (Figure 19F-G). The molar ratio of the released Ca^{2+} to PO_4^{3-} was estimated to be ~1.6 ± 0.2 (averaged over 7 days). This is very similar to the stoichiometric Ca/P ratio in

hydroxyapatite (1.67), implying that the Ca^{2+} and PO_4^{3-} release from the scaffolds could be a result of dissolution of an apatite-like CaP phase from the scaffolds.

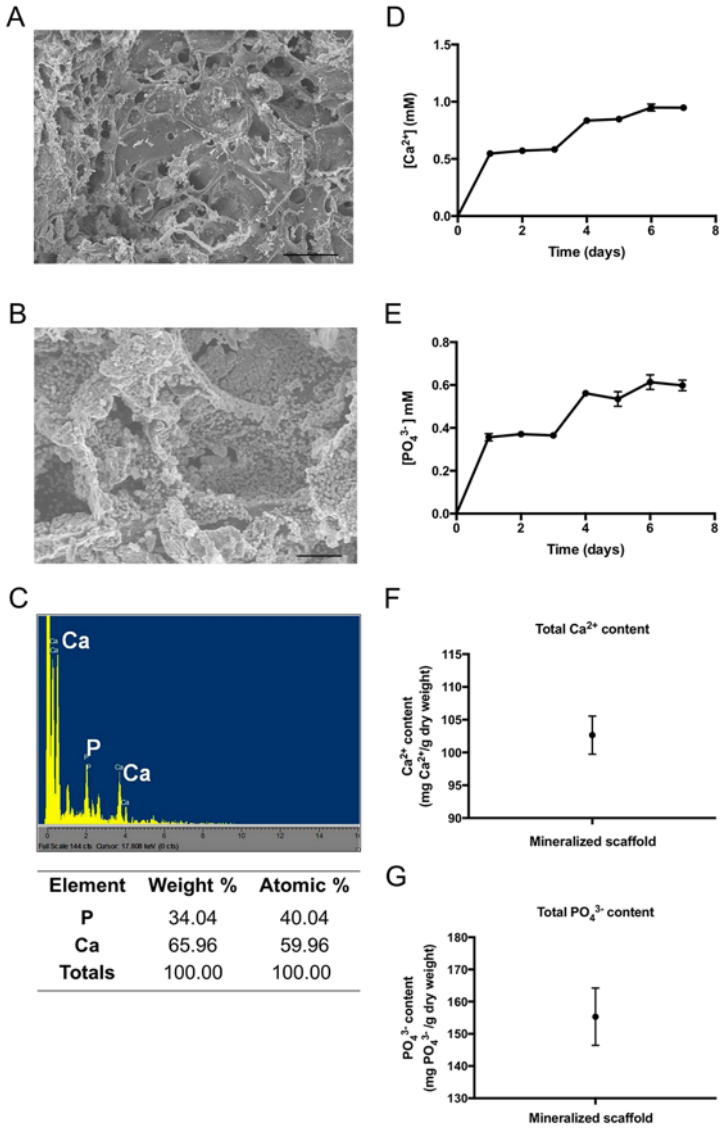

Figure 19: SEM/EDS and calcium phosphate dissolution of mineralized PEGDA-co-A6ACA macroporous hydrogel. (A-C) Scanning electron microscopy image of mineralized PEGDA-co-A6ACA macroporous hydrogel. Scale bar: 200 μm. (A) The macroporous network composed of randomly oriented, interconnected macroporous structures measuring 80-200 μm in diameter. Scale bar: 50 μm. (B) High magnification images revealed the presence of mineral crystals. (C) Elemental

dispersive spectroscopy (EDS) spectrum showing the presence of calcium and phosphate in the mineralized phase with Ca/P ratio of 1.5. (D-G) Total mineral contents and dissolution of the mineralized phase into Ca^{2+} and PO_4^{3-} ions. The release of (D) Ca^{2+} and (E) PO_4^{3-} as a function of time in ion-free Tris-HCl (1M, pH = 7.4) (F) Ca^{2+} content and (G) PO_4^{3-} content of the biomineralized scaffold prior to implantation.

4.3.2 Evaluation of hard tissue formation

Hard tissue formation within the cranial defects treated with the mineralized scaffolds, as well as the sham (untreated) groups, was examined by μCT at 2 and 8 - week post-implantation (Figure 20). μCT images after 2 weeks showed some form of hard tissue formation in all groups treated with mineralized scaffolds albeit with varying levels of differences (Figure 20A). The extent of hard tissue formation within the defect decreased with increasing age with 6-month and 14-month-old mice having the lowest levels of calcified tissue within the defect at 2 weeks post-implantation (Figure 20A). At 8 weeks post-implantation, almost complete closure of the defects with calcified tissues of varying degree of calcification was observed in all groups (Figure 20A). In contrast, sham groups had minimal hard tissue formation within the defect site throughout the extent of the study.

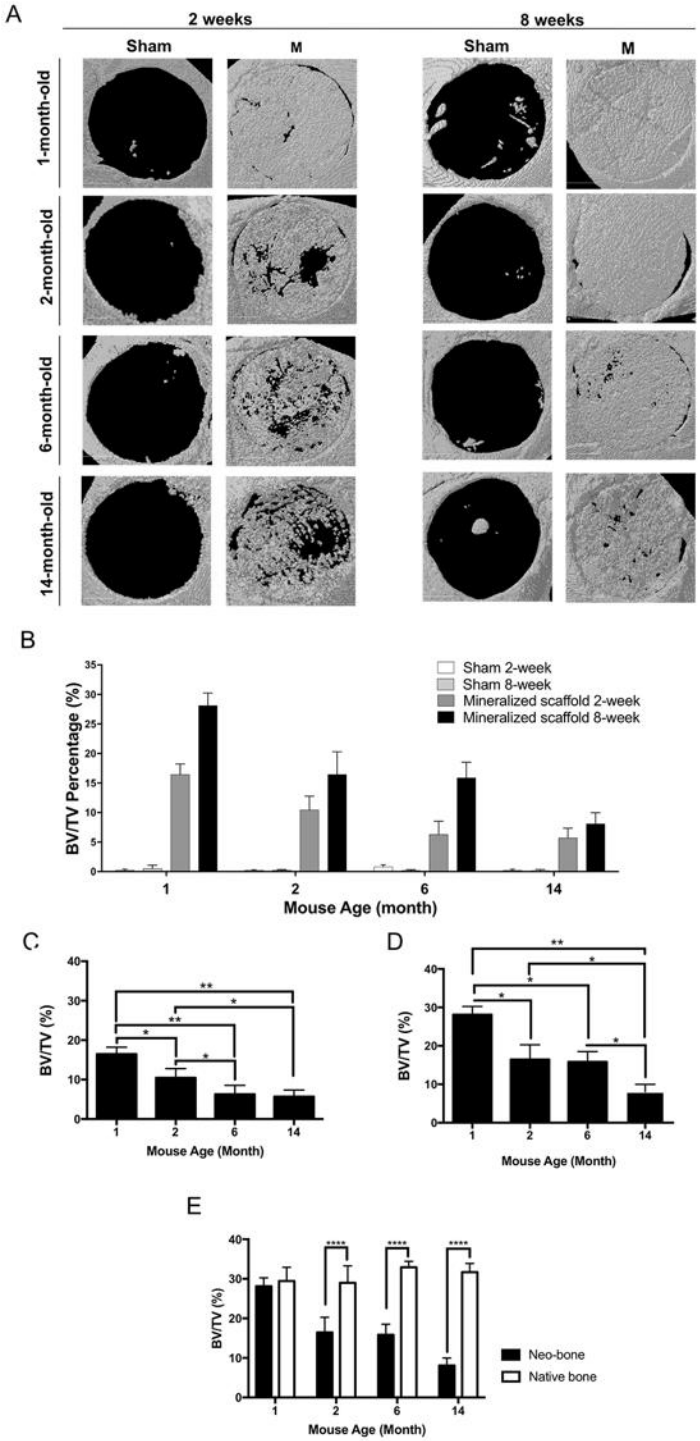

Figure 20: Calcified hard tissue formation within critical-sized cranial defects. (A) Micro-computed tomography (μCT) images of cranial defects in 1, 2, 6 and 14-

month-old mice treated with biomineralized scaffolds (M) and untreated (sham) groups at 2- and 8-week post-implantation. Scale bar: 1 mm. (B) Quantification of BV/TV percentage of sham and mineralized groups at 2- and 8-week post-implantation. (C) Quantification of defect closure at 2 weeks post-implantation. (D) Quantification of defect closure at 8 weeks post-implantation. (E) Comparison of BV/TV percentage between the neo-bone tissue formed within the mineralized scaffold and the surrounding native bone tissue at 8 weeks post-implantation. Asterisks denote *p*-values with statistical significance (*indicates $p < 0.001$, ** indicates $p < 0.01$, * indicates $p < 0.05$).**

Quantification of hard tissue formation by bone volume over total volume (BV/TV) within the defect site corroborated the observations made from the μCT images (Figure 20B-D). At 2 weeks post-implantation, 1-month and 2-month-old mice had higher hard tissue formation compared to the older cohorts (6-month and 14-month-old mice). Between the 6-month and 14-month-old mice, no statistical difference was observed in hard tissue formation (Figure 20C). Quantification of hard tissue formation at 8 weeks after implantation demonstrated similar trends as that of 2-week, where decreased bone formation was observed in older cohorts (Figure 20D). At 8 weeks post-implantation, 6-month-old cohorts showed similar calcification as to 2-month-old cohorts. While post-implantation time-dependent increase in calcification was observed in 1, 2, and 6-month-old cohorts, no significant change in calcification was observed in 14-month-old mice between 2 and 8-weeks post-implantation. At 8 weeks post-implantation, the μCT analyses showed similar BV/TV percentage between the newly formed and the surrounding native bone tissue for 1-month-old mice. For all other age

groups, the BV/TV percentage of the native tissue was significantly higher compared to the neo-bone tissue within the implant (Figure 20E).

4.3.3 Bone tissue formation

The H&E staining of the excised implants showed neo-bone tissue formation within the defects. Despite significant host cell infiltration, only a limited amount of detectable bone tissue was observed in the case of 6-month and 14-month-old groups at 2 weeks. In contrast, 1-month-old mice showed some level of neo-bone tissue formation. The extent of bone formation increased with post-implantation time. By 8 weeks, neo-bone tissue formation was observed among all age groups with 1-month and 2-month-old mice showing a significantly higher level of bone formation compared to 6-month and 14-month-old mice. Between 6-month and 14-month-old cohorts, the 14-month-old group had the lower bone formation. Furthermore, in the 14-month-old group, a thin layer of fibrous-like tissue was found to present at the periphery of the defect sites (Figure 22A). Histomorphometric quantification of areal fraction of bone tissue based on the H&E staining confirmed that bone tissue formation decreased as mouse age increased (Figure 22B). In the case of sham groups, no bone formation was observed and the defects were bridged by a thin layer of fibrous tissue, which is consistent with that normally found in non-healing bone defects (Figure 21A) [223].

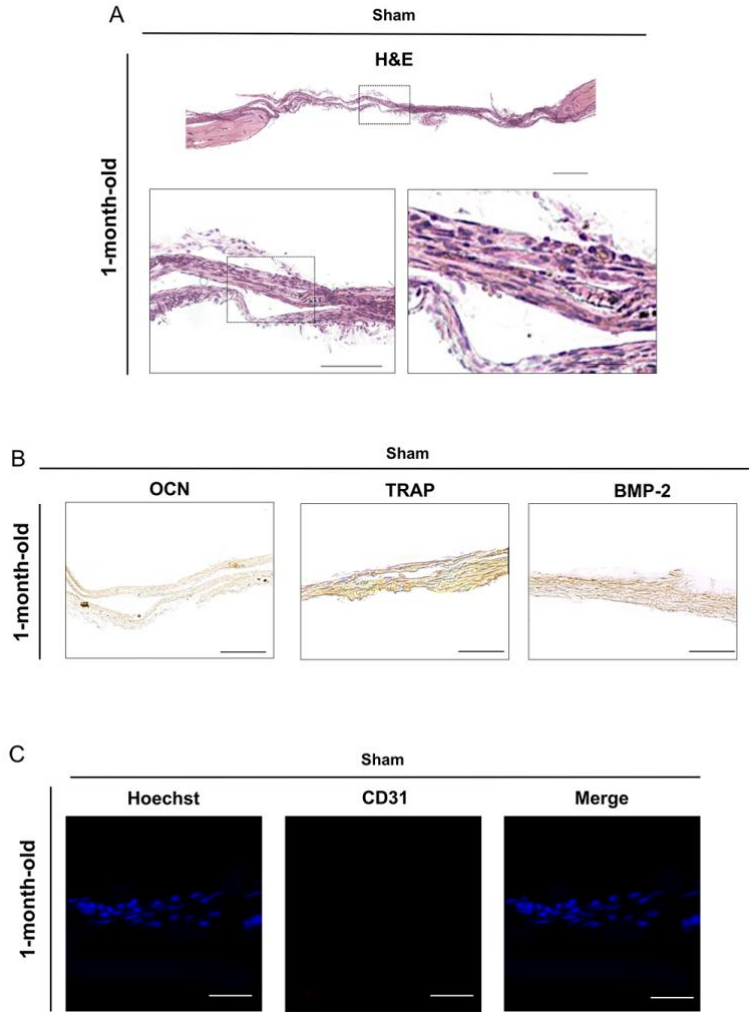

Figure 21: Histological assessment of the sham group. (A) H&E staining of the untreated defect (sham) for 1-month-old mice at 8 weeks post-implantation. Scale bars: 500 μm (upper panel), 100 μm (lower left panel), 25 μm (lower right panel). (B) Histological staining for bone-specific markers: OCN, BMP-2 and TRAP for 1-month-old mice at 8 weeks post-implantation. Scale bar: 100 μm. (C) CD31 staining of the untreated defect site. Scale bar: 100 μm.

To further confirm the neo-bone tissue formation, the tissue sections were stained for OCN, a bone-specific matrix protein that is secreted by osteoblasts. At 2 weeks, all groups treated with mineralized scaffold showed the presence of extracellular

matrix enriched with OCN (Figure 24A). However, the expression of OCN decreased as the age of the mice increased. A similar trend was observed at 8 weeks of post-implantation (Figure 23A). The mean histogram intensity of the images confirmed the aforementioned observations in which lower histogram values indicate higher OCN expression (Figure 23B). In the case of 14-month-old mice, no significant change in OCN expression between 2 and 8 weeks was observed. The fibrous tissue bridging the defect site of sham groups was found to show minimal OCN expression at 8 weeks post-implantation. (Figure 21B).

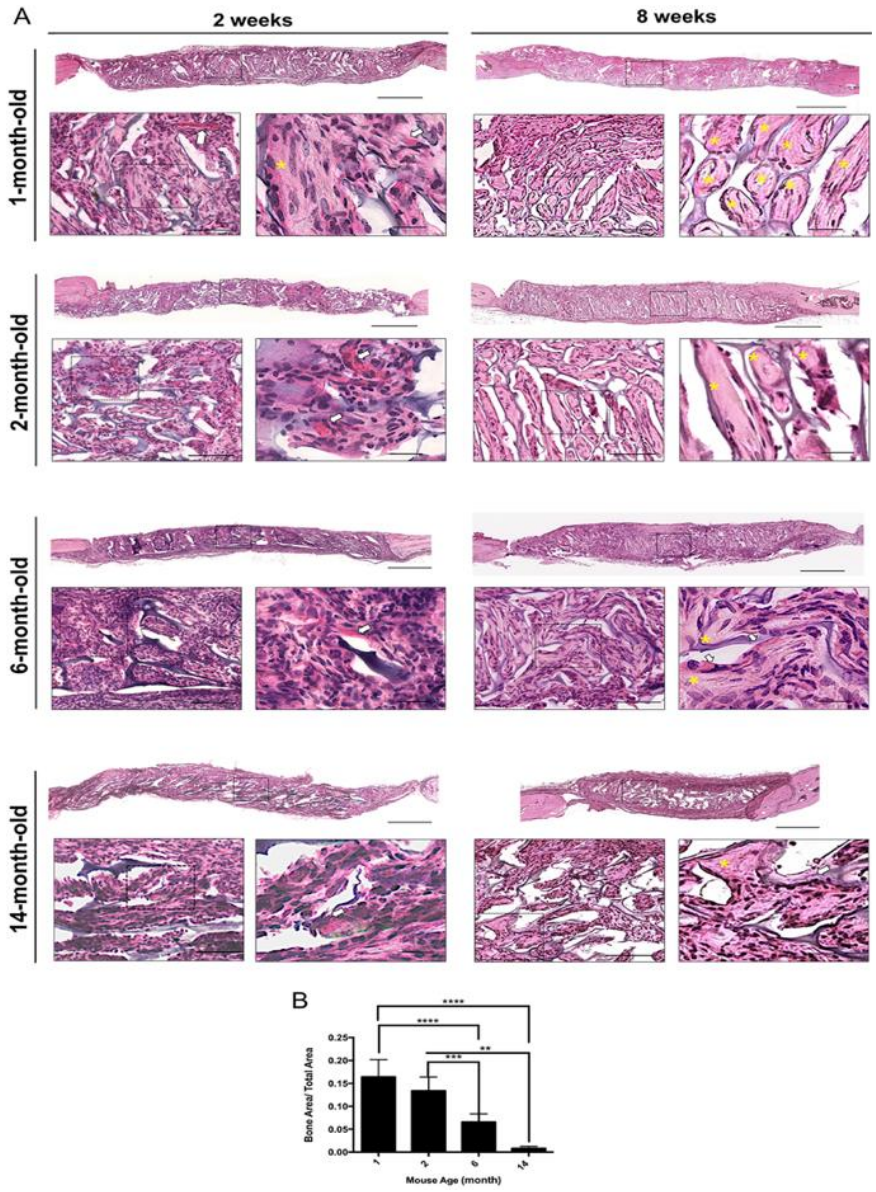

Figure 22: Morphological assessment of bone formation within critical-sized cranial defects at 8 weeks post-implantation. (A) Hematoxylin and eosin (H&E) staining of cranial sections for 1, 2, 6 and 14-month-old mice. High magnification images and insets reveal neo-bone tissue within the defect site. Yellow asterisks denote bone formation. White arrows indicate intraluminal blood vessels. Scale bars: 500 μm (upper panel) and 100 μm (lower left panels), and 25 μm (lower right panels). (B) Histomorphometric quantification of bone tissues. Asterisks denote p-values with statistical significance. (** indicates $p < 0.0001$, ***indicates $p < 0.001$, ** indicates $p < 0.01$, * indicates $p < 0.05$).**

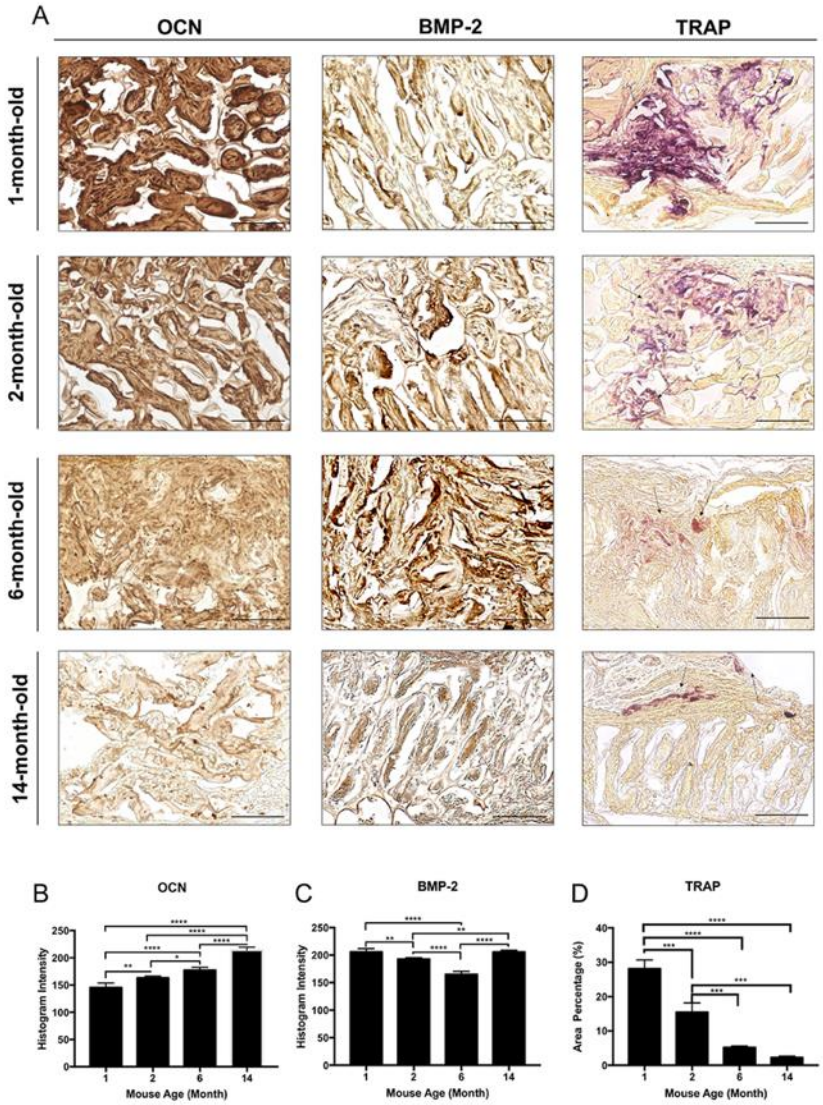

Figure 23: Bone-specific markers in newly formed tissue within cranial defects of biomineralized scaffold-treated groups at 8 weeks post-implantation. (A) Left column: immunohistochemical staining for osteocalcin (OCN) of the cranial defect site; middle column: immunohistochemical staining for bone morphogenetic protein 2 (BMP-2) of the cranial defect site; right column: histochemical staining for tartrate-resistant acid phosphatase (TRAP) of the cranial defect site. Arrows indicate TRAP-positive cells present within the scaffolds. Scale bars: 100 μm. (B) Mean histogram intensity of OCN expression in the left column of (A). (C) Mean histogram intensity of BMP-2 expression in the middle column of (A). (D) Quantification of areal percentage of TRAP-positive area per defect area in the right column of (A) (** indicates $p < 0.0001$, ***indicates $p < 0.001$, ** indicates $p < 0.01$, * indicates $p < 0.05$).**

At 2 and 8-week post-implantation, different age groups showed varying expressions of BMP-2, a protein commonly involved during osteogenesis (Figure 23A and Figure 24A). At 2 weeks post-implantation, all age groups showed the presence of BMP-2 within the defects treated with mineralized scaffolds. The expression of BMP-2 decreased as the age of the mice increased. Abundant expression of BMP-2 was observed in 1-month and 2-month-old groups, while moderate to slight expressions were found in the 6-month-old group and 14-month-old group, respectively (Figure 24A). At 8 weeks post-implantation (Figure 23A), the 6-month-old group had the highest expression of BMP-2 among all groups, while the 14-month-old group exhibited the lowest expression. Also, compared to the 1-month-old group, the 2-month-old group demonstrated higher expression of BMP-2. The mean histogram intensity of the images corroborated the findings in which lower histogram values indicate higher BMP-2 expression (Figure 23C and Figure 24C). Similar to OCN expression, the fibrous tissue bridging the defect site of sham groups was found to have a minimal BMP-2 expression at 8 weeks post-treatment (Figure 21B).

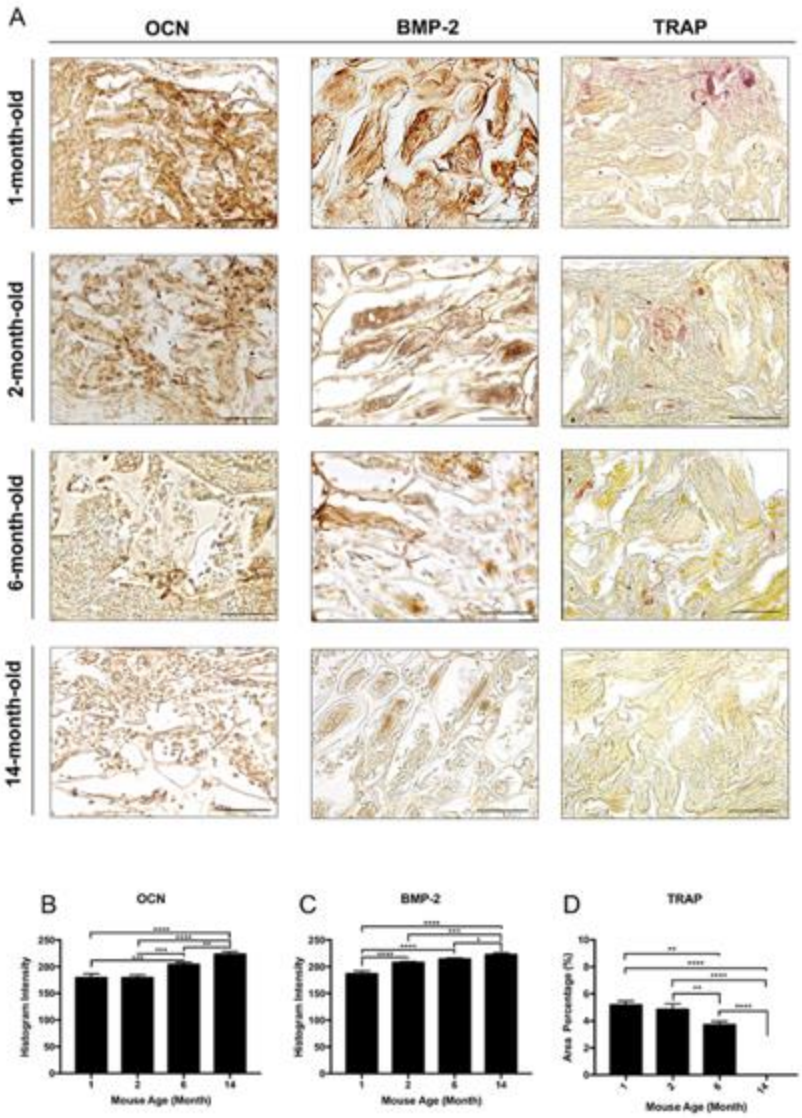

Figure 24: Bone-specific markers in newly formed tissue within cranial defects of biomineralized scaffold-treated groups at 2 weeks post-implantation. (A) Left column: immunohistochemical staining for OCN of the cranial defect site; middle column: immunohistochemical staining for BMP-2 of the cranial defect site; right column: TRAP of the cranial defect site. Arrows indicate TRAP-positive cells present within the scaffolds. Scale bars: 100 μm. (B) Mean histogram intensity of OCN expression in the left column of (A). (C) Mean histogram intensity of BMP-2 expression in the middle column of (A). (D) Quantification of the areal percentage of TRAP-positive area per defect area in the right column of (A) (** indicates $p < 0.0001$, ***indicates $p < 0.001$, ** indicates $p < 0.01$, * indicates $p < 0.05$).**

Tartrate-resistant acid phosphatase (TRAP) staining was performed to examine the presence of osteoclast-like cells within the newly formed bone tissue (Figure 23A and Figure 24A) At 2 weeks post-implantation, TRAP-positive cells were detected in all defects treated with mineralized scaffolds except 14-month-old cohorts, where no TRAP-positive cells were detected (Figure 24A and Figure 24D). Following 8 weeks of implantation, TRAP-positive cells were detected in all age groups. Among the different age groups, more TRAP-positive cells were observed in younger mice (Figure 23A and Figure 23D). In 1, 2 and 6-month-old groups, TRAP-positive cells were located within the mineralized implants. However, in the 14-month-old group, TRAP-positive cells were observed only at the interface of the native tissue and the implant (Figure 23A). In the sham groups, no TRAP-positive cells were detected at 8 weeks post-implantation (Figure 21B).

4.3.4 Vascularization and Recruitment of cells

Hematoxylin and eosin (H&E) staining after 2 weeks of implantation showed significant host cell infiltration in all treated groups (defects covered by mineralized scaffolds) despite the differences in host age. The recruited cells were homogeneously distributed throughout the implant. Concomitant with the recruitment of cells, all the defects treated with the mineralized scaffolds were positive for vasculature throughout the defect, with the presence of red blood cells, indicating formation of anastomosed vessels with the host (Figure 25 and Figure 26). The presence of vasculature within the

implants persisted throughout the experimental time (8 weeks post-implantation). The presence of vasculature was further confirmed by staining for platelet endothelial cell adhesion molecule (PECAM-1; CD31) at 2 and 8 weeks (Figure 26A and Figure 27A, respectively). At 2- and 8-week post-implantation, all groups showed the presence of CD31-positive cells within the defects. At 2 weeks, there were more CD31 positive cells present in the 1 month and 2-month-old groups than 6-month and 14-month-old groups (Figure 26B). By the end of 8 weeks, amounts of vasculature decreased in 1, 2 and 14-month-old groups, whereas the 6-month-old group demonstrated more vasculature (Figure 27B).

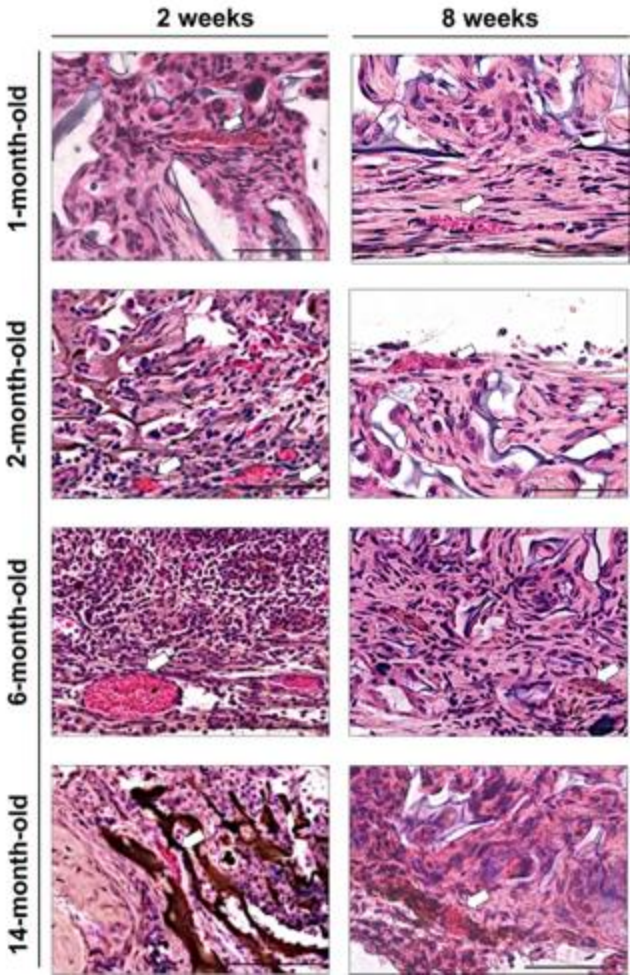

Figure 25: Vascularization of biomineralized scaffolds showing red blood cells. H&E images of biomineralized scaffolds showing the presence of red blood cells (RBCs) at 2- and 8-week post-implantation. White arrow denotes RBCs. Scale bar: 100 μm.

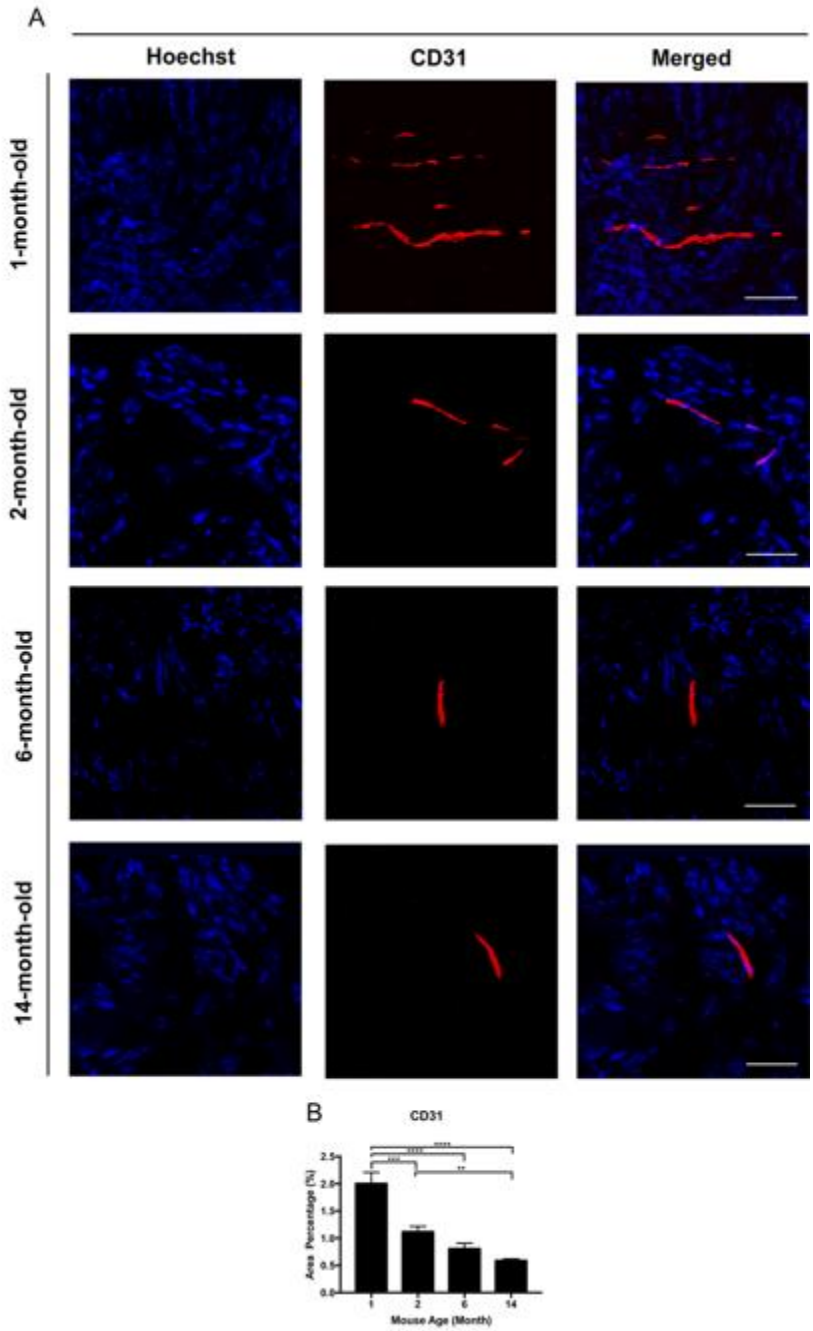

Figure 26: Vascularization of cranial defects treated with biomineralized scaffolds at 2 weeks post-implantation (A) Immunofluorescent staining for CD31 and Hoechst 33342 staining of cell nuclei within the defect. Scale bar: 100 μm. (B) Quantification of the areal percentage of CD31 positive area per defect area. (** indicates $p < 0.0001$, ***indicates $p < 0.001$, ** indicates $p < 0.01$, * indicates $p < 0.05$).**

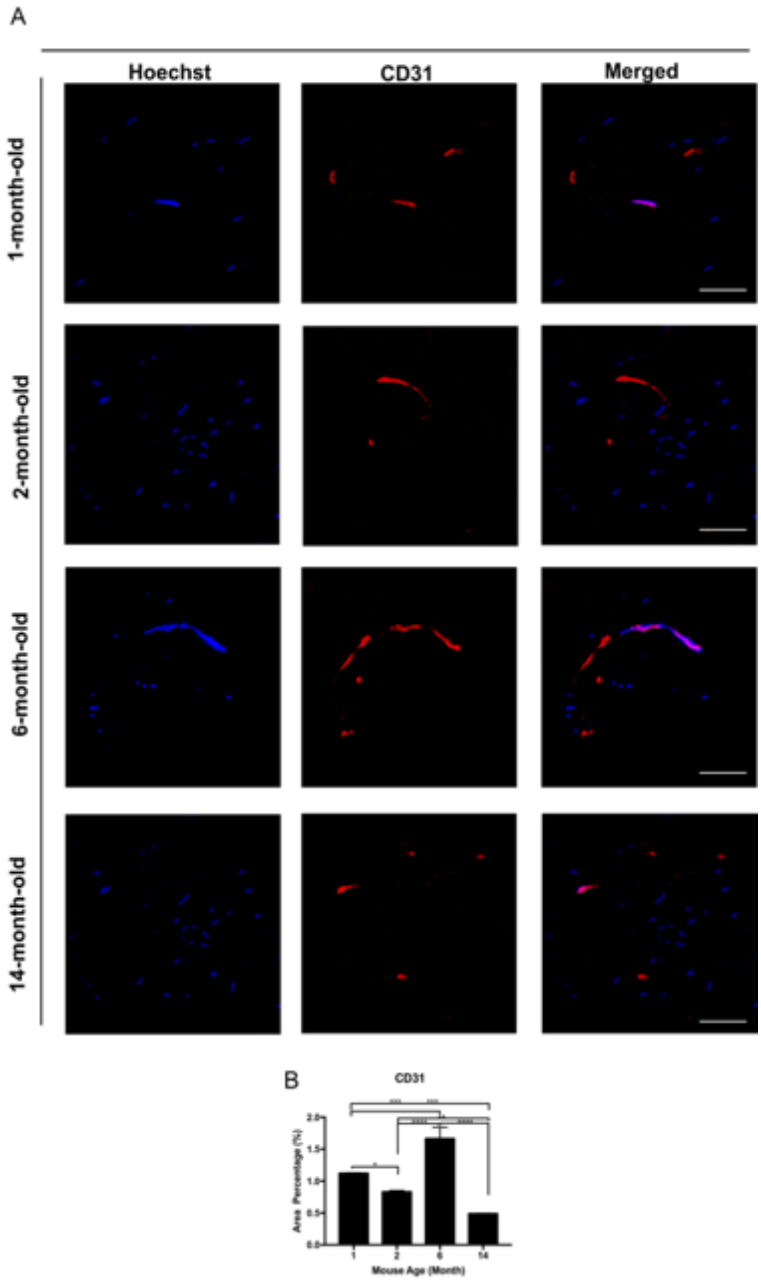

Figure 27: Vascularization of cranial defects treated with biomineralized scaffolds at 8 weeks post-implantation. (A) Immunofluorescent staining for platelet endothelial cell adhesion molecule (PECAM-1; CD31) and Hoechst 33342 staining of cell nuclei within the defect site. Scale bar: 100 μm. (B) Quantification of the areal percentage of CD31 positive area per defect area. (** indicates $p < 0.0001$, ***indicates $p < 0.001$, ** indicates $p < 0.01$, * indicates $p < 0.05$).**

4.4 Discussion

Previous chapter demonstrated that mineralized materials that can recruit endogenous cells and support their osteogenic differentiation to form bone tissue can be used to repair cranial defects [213]. It was also established that the CaP mineral component is necessary for recruiting and activating endogenous cells for bone repair [213]. Herein, I evaluated the effect of host age on mineralized biomaterial-mediated bone tissue formation using a critical-sized cranial defect as a model system. Consistent with our previous findings, results from this study show that the mineralized scaffolds support neo-bone tissue formation within the defect through recruiting endogenous cells [213].

Histological analyses of the excised tissues suggest that all implants were infiltrated with host cells despite the age differences among the recipients. The macroporous nature of the scaffold not only facilitated cell infiltration, but also aided homogeneous distribution of the host cells throughout the implant. Similar to cell infiltration, all implants were characterized by the presence of intraluminal red blood cells, suggesting that the neo-vessel within the implant had anastomosed with the host vasculature. A number of factors, such as microarchitecture of the scaffold and presence of calcium phosphate minerals, could contribute to implant vascularization [194,224]. The mineral phase of the CaP-biomaterials also plays an important role in vascularization [224]. Besides scaffold properties, the infiltrated cells could also promote vascularization of the

implants. Osteoblasts and mesenchymal progenitor cells are known to secrete pro-angiogenic growth factors such as vascular endothelial growth factor A (VEGF-A) [207,208].

OCN is an osteoblast-specific marker [209], whereas BMP-2 is mostly a pre-osteoblast marker [210]. While OCN expression showed an age-dependent decrease in expression throughout the study, BMP-2 expression in 6-month-old mice was more prominent than 1-month and 2-month-old mice at 8 weeks post-implantation. This high expression of BMP-2 could be associated with the delayed osteoblastogenesis in 6-month-old mice. Concurrent with these observations, μCT analyses demonstrated that BV/TV percentage of 6-month-old mice, which was significantly lower than the 2-month-old group at 2 weeks post-implantation, resembled that of the 2-month-old group by 8 weeks post-implantation. Taken together, these observations imply delayed osteoblastogenesis/bone healing in the middle-age group compared to the younger groups. In contrast, the persistent low expression of these makers in the 14-month-old mice suggests impaired osteoblastic differentiation/ bone forming abilities in the elderly group. As for 1-month and 2-month-old mice, the low BMP-2 expression and high OCN expression at 8 weeks could indicate maturation of osteoblasts, suggesting more efficient bone reparative capabilities in the younger groups.

Coincided with high BMP-2 expression, 6-month-old mice also exhibited the highest vascularization at 8 weeks post-implantation among all the groups. This high vascularization could be associated with the high osteoblastogenesis in 6-month-old

mice at 8 weeks post-implantation. Vascularization plays a key role in bone formation [225] and the crosstalk between osteoblasts and endothelial cells is necessary for bone formation and regeneration [226,227]. In intramembranous osteogenesis, extensive vascularization was reported during the transition of pre-osteoblasts to osteoblasts [226]. In addition to promoting osteoblastogenesis, BMPs stimulate angiogenesis through the production of VEGF-A by osteoblasts[226].

Our findings showed that the number of TRAP-positive cells in the neo-bone tissue decreased as the age of mouse increased. Besides this decline, the TRAP-positive cells were only found at the interface of the implant and native bone in the case of the 14-month-old mice by 8 weeks. Osteoblasts not only play a central role in bone formation, but also regulate osteoclast maturation through soluble factors, which is necessary for bone resorption and remodeling[228,229]. The role of cell-cell communication in terms of direct contact is necessary for osteoclastogenesis, and therefore the minimal osteoblast content within the implants could have contributed to the lack of TRAP-positive cells in the 14-month-old group. Osteoblasts have been shown to secrete monocyte chemoattractant protein-1 (MCP-1) to recruit osteoclastic precursors, and receptor activator of nuclear factor kappa-B ligand (RANKL) to induce osteoclast differentiation of these cells[228]. The lack of osteoblasts within the implant could have led to less precursor recruitment and osteoclast formation.

Osteoclasts not only play a key role in bone remodeling through bone resorption, but also contribute to bone formation through multiple processes [230,231]. In addition to RANKL/RANK interactions, osteoclastic cells also communicate with osteoblastic cells through ephrinB2/EphB4 signaling (ephrinB2 expressed by osteoclast progenitor cells and EphB4 expressed by osteoblastic cells)[232]. Forward signaling through EphB4 in osteoblasts has been shown to enhance their differentiation resulting in increased bone mass[233]. Furthermore, resorption of matrix releases and activates a number of growth factors that are shown to promote osteoblast activity and bone formation[234].

Age of the recipients had a strong influence on the rate and the amount of bone formation. As evident by the radiographic and histochemical analyses, 6-month-old mice showed delayed bone regeneration, while the 14-month-old mice exhibited a compromised tissue repair ability with no significant increase in calcification observed between 2 to 8 weeks. These findings are in agreement with the clinical observations that the ability of the bone tissue repair declines with age [235-237]. Given that the physicochemical cues of the implant are consistent across the groups, the delayed bone regeneration in older groups could be associated with decreased osteogenic potential [238-241], lower clonogenic ability [219,242,243], decreased proliferation [242,244], and diminished vascular support [245] of osteoprogenitor cells. Age-related decrease in growth hormone levels involved during bone formation [246,247], and decline in angiogenesis [215,248,249] may contribute to impaired bone repair. Since for C57BL6/J mice, 14-month-old is not

considered as an age of postmenopausal, the compromised bone repair observed in this study may not be entirely due to sex steroid deficiency associated with postmenopause [250]. Previous *in vitro* studies have shown that bone marrow-derived mesenchymal stem cells from aged mice exhibit lower VEGF expression, stromal cell-derived factor 1 chemokine (SDF-1), protein kinase B than those from young mice [251]. Both VEGF and SDF-1 are involved in neovascularization and angiogenesis. In addition, age-associated changes of inflammatory environments could also have a profound influence on bone regeneration through affecting the levels of inflammatory mediators that are pivotal for osteoblast differentiation and subsequent bone formation [252-254].

The results discussed in this study involves female mice, and similar experiments should be performed with male mice in order to fully elucidate effects of age on biomaterial-mediated bone regeneration. Furthermore, our current work only focuses on repairing of cranial defect, which involves intramembranous ossification. Hence, caution should be used while extrapolating results from this model to long bone defects which involve endochondral ossification[255].

4.5 Conclusion

In summary, this chapter demonstrates age-related host responses in the healing of critical-sized cranial defects treated with biomineralized materials. My findings show that mineralized macroporous biomaterials are sufficient to induce hard tissue formation through recruitment of endogenous cells and achieve almost complete closure

of critical-sized cranial defects in mice. Moreover, the age of the recipient mice had a significant influence on the quantity and quality of the neo-bone tissues characterized in terms of bone mineral deposition and bone tissue-specific markers. Specifically, as elucidated by radiographic and histological evidence, delayed bone formation and decreased quantity of neo-bone tissue formation were observed in older mice.

5. Chapter 5: Develop a Tough Hydrogel Network to Enhance the Mechanical Property of Mineralized Scaffolds

While the biomineralized biomaterial-mediated bone tissue repair is highly attractive, its clinical application in bone defect repair is greatly hindered by the lack of mechanical strength and toughness of this material. Therefore, in this chapter, I describe a novel double network hydrogel system with unique contrasting network structure, where the first network is tightly cross-linked by a rigid and brittle polyelectrolyte (A6ACA) while the second network is loosely cross-linked by a soft and ductile neutral polymer (PEGDA). The mechanical property, swelling property and mineral dissolution kinetics of the proposed materials were evaluated. Moreover, macroporous scaffold was prepared using the proposed DN hydrogel.

As the first author of the manuscript serving as the basis for this chapter, I oversaw and was involved in all aspects of this research, including experimental planning, writing, figure preparation, and editing in conjunction with my co-authors Alina Kirillova and Ken Gall.

5.1 Introduction

As described in earlier sections, bone defects caused by degenerative disease and trauma are a widespread clinical problem that require effective bone augmentation strategies[256]. Incorporating N-acryloyl-6-aminocaproic acid (A6ACA) moieties to biocompatible polymeric hydrogel backbone has been reported as a promising strategy

to promote osteogenicity and osteoinductivity of conventional inert hydrogel systems[35]. As shown in Chapter 3-4, PEGDA-co-A6ACA hydrogels exhibited excellent biological functionalities both *in vivo* and *in vitro*, but their clinical application in bone defect repair are greatly restricted by their intrinsic poor mechanical properties.

In recent years, many efforts have been made to develop tough hydrogels with new approaches and new hydrogel systems, including double network hydrogels[257], nanocomposite hydrogels[258-262], sliding-ring hydrogels[263,264], macromolecular microsphere composite hydrogels[265], tetra-PEG hydrogels[266], and physical interaction enhanced hydrogels[267-269]. Among them, double network (DN) hydrogels have been reported to achieve extremely high mechanical strength [257] and high mechanical toughness [270]. DN hydrogels are prepared by combining a rigid network with a flexible network based on physical or chemical cross-linking, where the rigid network can effectively consume the fracture energy during the deformation process while the flexible network can ensure the integrity of the hydrogel[271]. A number of double network hydrogels with excellent mechanical properties have been reported in the recent years for bone tissue engineering[272-275]. Nonoyama *et al*. developed a tough DN hydrogel consisting of poly (2-acrylamido-2-methyl propanesulfonic acid) as the brittle first network and poly (N, N-dimethylacrylamide) (PDMAAm) as the ductile second network. Fukui *et al*. showed that implantation of this into the osteochondral defect of rabbits[276]PAMPS–PDMAAm DN-hydrogel can promote cartilage regeneration, but this hydrogel only serves as

structural support that lacks bioactivity for the underlying bone defects. Hybridization of the DN-hydrogels with hydroxyapatite enhances their osteointegration to native bone after implantation [277]. However, the poor interactions between inorganics and the polymer matrix usually make these hybrid hydrogels decrease in toughness under external force [278]. Furthermore, Zhang et el. developed a strong DN-hydrogel by interspersing methacrylated gelatin (GelMA) network into a well-defined nanocomposite hydrogel consisting of methacrylated chitosan (CSMA) and polyhedral oligomeric silsesquioxane (POSS)[279]. They demonstrated *in situ* bone regeneration after implanting osteoprogenitor cell-loaded GelMA/CSMA-POSS hydrogels into rat cranial defects. However, incorporation of exogenous cells into the hydrogel to treat bone defects may introduce potential safety and cost concerns.

As mentioned earlier, PEGDA-co-A6ACA hydrogel has demonstrated great potentials for bone tissue regeneration [52-56,77,280]. In order to enhance its mechanical properties and expand its ranges of applications in bone tissue engineering, I prepared a A6ACA-PEGDA DN-hydrogel through a simple two-step synthesis process, where the first network of A6ACA was crosslinked through introduction of crosslinker N,N'-Methylenebisacrylamide (bisacrylamide), followed by formation of second PEGDA network within it. I investigated the effects of crosslinking density of these networks on DN-hydrogel formation by employing varying bisacrylamide crosslinker concentrations (2 mol.%, 4 mol.%, and 6 mol.%) and PEGDA molecular weight (3.4 kDa, 6 kDa, 10 kDa,

and 20 kDa). The findings from this study suggest that mechanical properties A6ACA-PEGDA DN-hydrogels are greatly enhanced compared to SN-hydrogels of the same composition. Among all groups involved in this study, DN-hydrogel with 6 mol.% bisacrylamide and 10 kDa PEGDA displayed the highest compressive strength and toughness. Using this composition, I further introduced macroporous architectures into the DN-hydrogels and demonstrated their mineralization capacities through mineral dissolution kinetic study.

5.2 Materials and Methods

5.2.1 Material synthesis and characterization

N-acryloyl 6-aminocaproic acid (A6ACA) and poly (ethylene varying glycol)-diacrylate (PEGDA Mn: 3.4 kDa, 6 kDa, 10 kDa and 20 kDa) were synthesized as previously described [76,127]. Briefly, 2.98 mmol PEG (Mn: 3.4 kDa, 6 kDa, 10 kDa, and 20 kDa) was dissolved in 250 mL of toluene at 127 °C, followed by refluxing for 4 h with vigorous stirring. Azeotropic distillation was used to remove the traces of water from the reaction mixture. On cooling this solution to room temperature (~25 °C), 1 mL (7.46 mmol, 2.5 eq) of triethylamine was added with vigorous stirring. The reaction mixture was transferred to an ice bath at 4°C. To this reaction mixture, 0.6 mL (7.46 mmol, 2.5 eq) of acryloyl chloride in 15 mL of anhydrous dichloromethane (DCM) was added in dropwise manner for 30 mins. The reaction mixture was raised to 45 °C and stirred overnight. The reaction mixture was filtered through diatomaceous earth (Celite 545) to

remove quaternary ammonium salt. The filtrate was concentrated using a rotavapor and precipitated in excess diethyl ether. Precipitated product was dissolved in DCM and reprecipitated in diethyl ether. The resultant PEGDA was filtered and dried under vacuum at room temperature for 24 h.

N-Acryloyl 6-aminocaproic acid (A6ACA) was prepared as described by Ayala et al.[76] Briefly, 13.11 g (100 mmol) of 6-aminocaproic acid (Sigma Aldrich, catalog number: A2504) and 4.4 g (110 mmol, 1.1 equivalents) of NaOH were dissolved in 80 mL of deionized (DI) water at 4 °C under vigorous stirring. To this, 8.937 mL (110 mmol, 1.1 equivalents) of acryloyl chloride in 15 mL of anhydrous tetrahydrofuran was added dropwise for 30 minutes. The pH of the reaction mixture was maintained between 7.5 and 7.8 until the reaction was complete. The pH of the reaction mixture was then decreased to pH 3 using 6 N HCl at 0 °C, and the solution was extracted using ethyl acetate. The organic layers were collected, combined, and dried over sodium sulfate. The solution was then filtered, concentrated, and precipitated in petroleum ether.

The successful syntheses of various products were confirmed through Fourier transform infrared (FT-IR) spectra. The Fourier transform infrared (FT-IR) spectra were recorded on Nicolet 8700 equipped with germanium crystal ATR crystal.

5.2.2 Single and double-network hydrogel synthesis

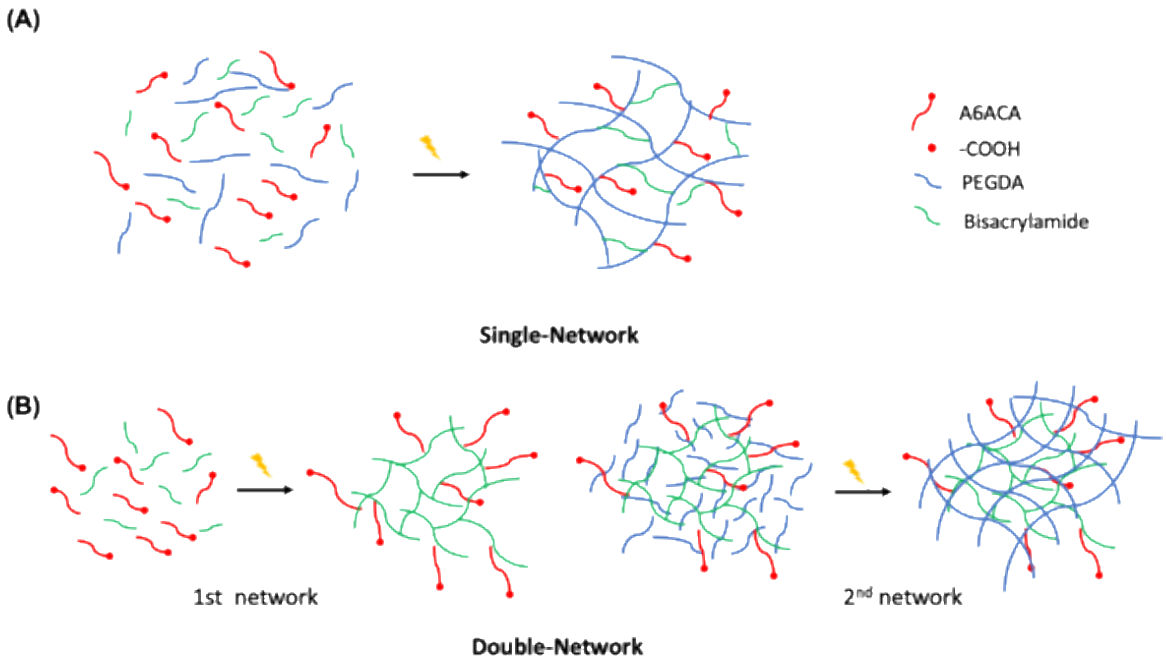

Figure 28: Schematics of single and double-network hydrogel synthesis.(A) Schematics of one-step synthesis process of A6ACA-PEGDA SN-hydrogel (B) Schematics of two-step synthesis process of A6ACA-PEGDA DN-hydrogels.

Double network hydrogels were prepared using the two-step synthesis method illustrated in Figure 28, with compositions listed in Table 1. Briefly, approximately 75μL first network precursor solution containing 1M A6ACA, bisacrylamide (2 mol.%, 4 mol.% and 6 mol.%) and 0.3% (w/v) Irgacure was added to cylindrical polypropylene mold measuring 4 mm in diameter and 6 mm in height. First network hydrogels were polymerized under ultraviolet light (λ = 365 nm) for 10 mins. Subsequently, these intermediate hydrogels were immersed in precursor solution of the second network containing a mixture of 20% (w/v) PEGDA (Mn: 3.4 kDa, 6 kDa, 10 kDa and 20 kDa)

respectively, and 0.3% (w/v) Irgacure for 1 day. After equilibration, the second network was polymerized within the first network under ultraviolet light (λ = 365 nm) for 10 mins, followed by hydrating in deionized (DI) water to yield double network hydrogels.

Table 1: Polymer network compositions of DN-hydrogels

Network	Components	Concentrations			
1st	Bisacrylamide (mol %)	0%	2%	4%	6%
	A6ACA (M)	1M			
2nd	PEGDA Mw (Da)	3.4k	6k	10k	20k

For single network hydrogels, approximately 75 of precursor solution containing of a mixture of 1M A6ACA, bisacrylamide (2 mol.%, 4 mol.%, and 6 mol.%) and 20%(w/v) PEGDA (Mn: 3.4 kDa, 6 kDa, 10 kDa, and 20 kDa) and 0.3% (w/v) Irgacure were polymerized under ultraviolet light (λ = 365 nm) for 10 mins in cylindrical polypropylene mold measuring 4 mm in diameter and 6 mm in height.

After completion of UV polymerization, the resultant SN/DN-hydrogels were subsequently hydrated in deionized water for 1 day.

5.2.3 Porous hydrogel Synthesis and Mineralization of Hydrogels

Macroporous hydrogels were prepared using the poly (methyl methacrylate) (PMMA) leaching method. Briefly, cylindrical polypropylene molds (4 mm in diameter, 6 mm in height) were packed with PMMA microspheres with diameters ranges of 160-180 μm (Cospheric, catalog No. PMMAMS-1.2).

Porous double network hydrogels were prepared using the two-step method described in the earlier section. Briefly, precursor solution of first network containing

1M A6ACA, bisacrylamide (2 mol.%, 4 mol.%, and 6 mol.%) and 0.3% (w/v) Irgacure was added into the PMMA-packed mold and photopolymerized by using ultraviolet light (λ = 365 nm) for 10 mins. Subsequently, together with the PMMA beads, the first network hydrogels were immersed in precursor solution of second network containing mixture of 20% (w/v) PEGDA (Mn: 3.4 kDa, 6 kDa, 10 kDa, and 20 kDa) respectively, and 0.3% (w/v) Irgacure for 1 day. After equilibration, the second network was polymerized under ultraviolet light (λ = 365 nm) for 10 mins. For porous single network hydrogels, precursor solution containing of 1M A6ACA, bisacrylamide (2 mol.%, 4 mol.% and 6 mol.%), and 20%(w/v) PEGDA (Mn: 3.4 kDa, 6 kDa, 10 kDa, and 20 kDa) and 0.3% (w/v) Irgacure was added to the PMMA-packed mold and polymerized using ultraviolet light (λ = 365 nm) for 10mins. Finally, PMMA beads were leached out using acetone for 3 days and the resultant hydrogels were hydrated in deionized (DI) water to yield macroporous architectures.

Mineralization of the hydrogels was achieved by immersing the hydrogel cylinders in simulated body fluid (m-SBF), prepared as previously described[35], for 12h and, subsequently, in 40 mM Ca^{2+}/24 mM PO_4^{3-} (pH 5.2) for 1 h. The scaffolds were briefly rinsed in ultrapure water and immersed in m-SBF for 48 h at 37°C.

5.2.4 Scanning electron microscopy (SEM)

Scanning electron microscopy (SEM) was used to examine the pore structure and surface morphology of the DN-hydrogels. The sample hydrogels were sliced into thin pieces followed by drying under 60°C for 48 h. These samples were then sputter coated (Denton Desk V) with gold for 200s and imaged using SEM (Apreo S ThermoFisher Scientific).

5.2.5 Mechanical testing

Monotonic compression tests were conducted on all groups ($n = 4$/group) and at a displacement rate of 1 mm/min until mechanical failure using a Test Resources 910LX25 servo-hydraulic test machine (max capacity of 25kN) at room temperature. Compressive strain of the hydrogel sample was regarded as the length change related to the initial length of the sample, and the stress was assessed by the force divided by the initial cross-sectional area of the hydrogel sample. Mechanical properties including ultimate compressive strength and strain were identified. Toughness of the sample was estimated by the area below the stress-strain curve, and compressive modulus was fitted by power-law on the initial linear regime of the stress-strain curve.

5.2.6 Calcium and phosphate assays

Calcium and phosphate assays were performed to determine the contents of Ca^{2+} and PO_4^{3-} in the mineralized hydrogels and their dissolution from CaP minerals. The hydrogels were rinsed and homogenized in ultrapure water. Their dry weights were

recorded after drying under 37°C for 48 h. To measure the amounts of Ca^{2+} and PO_4^{3-}, dried scaffolds were incubated in 0.5 M HCl at 25 °C. Incubation medium was collected after 3 days. To assess dissolution of Ca^{2+} and PO_4^{3-} from CaP mineral in environments lacking these ions, dried scaffolds were rehydrated and equilibrated in ultrapure water. The scaffolds were then incubated in 1 M Tris-HCl (pH = 7.4) at 37 °C for 7 days. Incubation medium was collected and replenished with fresh medium daily. The collected medium was analyzed to determine Ca^{2+} and PO_4^{3-} contents.

A calcium assay was conducted based on manufacturer's protocol (Calcium reagent set, Pointe Scientific, catalog number: C7503). Briefly, 20 μL of the sample solution was mixed with 1 mL of assay solution containing o-cresolphthalein complexone (CPC). The reaction of calcium with CPC results in a purple color. The absorbance of the resultant product was measured at 570 nm using a UV/Vis spectrophotometer (Shimadzu UV-3600).

Phosphate assay was performed as reported elsewhere [188]. Briefly, the assay solution was prepared by mixing 1 volume of 10 mM ammonium molybdate, 2 volumes of acetone, and 1 volume of 5 N H_2SO_4. 125 μL of the sample solution was mixed with 1 mL of assay solution. To this, 100 μL of 1 M citric acid was added. The absorbance of the resulting solution was measured at 380 nm using a UV/Vis spectrophotometer. The PO_4^{3-} concentration in solution was determined using a calibration curve for PO_4^{3-}, which was generated for a concentration range of 0–4 mM PO_4^{3-}.

5.2.7 Swelling ratio measurement

The equilibrium swelling ratios (SR) of hydrogels were investigated in deionized water at room temperature. The swelling ratios of the samples were determined as the ratio between weights of swollen hydrogel (W_s) and dried hydrogel (W_d).

$$\text{Swelling ratio} = (W_s / W_d) * 100\%$$

5.2.8 Statistical analysis

All data were presented as mean ± standard deviation values. Mechanical properties (i.e. toughness, elastic modulus, ultimate compressive strength and strain), and swelling ratio of hydrogels were assessed by GraphPad Prism 7. One-way analysis of variance (ANOVA) with Tukey-Kramer post-hoc test was used for comparisons between mechanical properties of different hydrogels.

5.3 Results and Discussions

5.3.1 Mechanical testing

Mechanical strength is one of the important indicators for considering hydrogels as a bone tissue repair material. It has been demonstrated that the strength of hydrogels can affects cell proliferation and differentiation.[72]

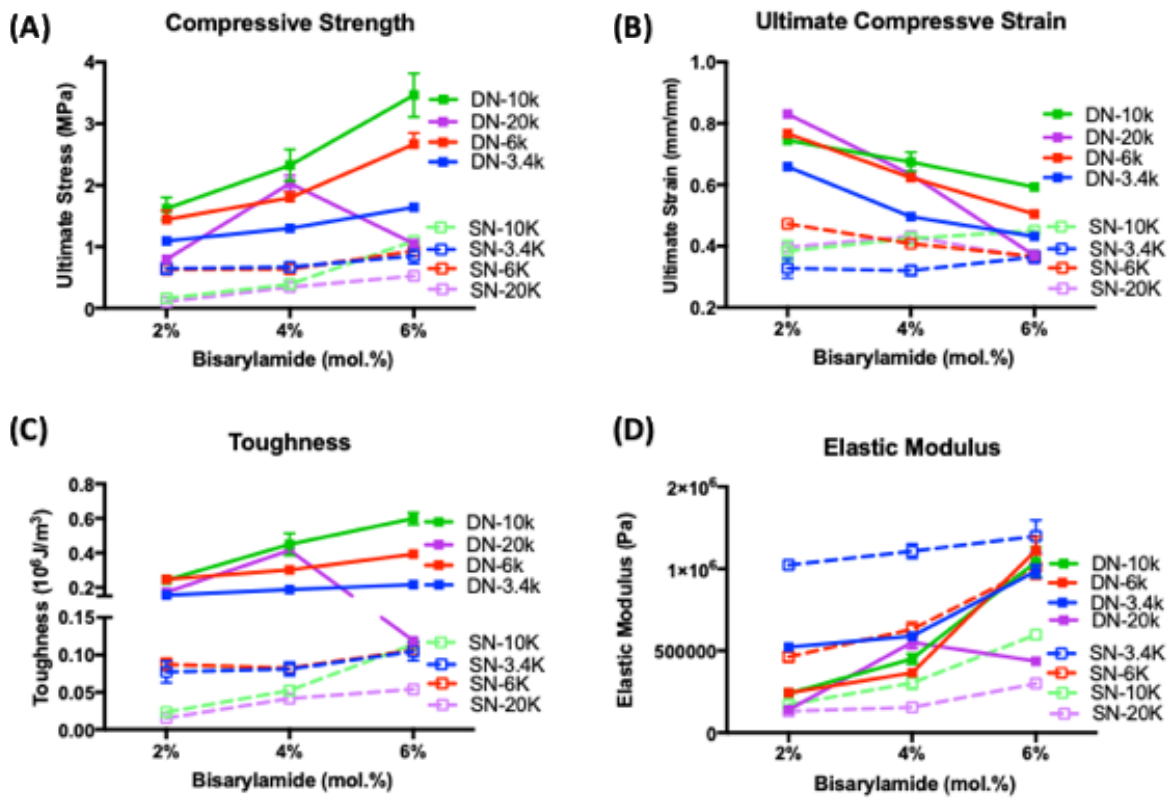

Figure 29: Summary mechanical property of SN and DN-hydrogels based on compositions. (A) Compressive strength (B) Ultimate compressive strain (C) Toughness (D) Elastic Modulus of SN and DN hydrogel with different PEGDA Mw and bisacrylamide concentrations. DN: double-network, SN: single-network

The compressive strength, ultimate strain, toughness and elastic modulus of A6ACA-PEGDA SN and DN-hydrogels are summarized in Figure 29A-D. Different plot line types represent either SN (dotted line) or DN (solid line) configuration, and different colors of the plots represent different PEGDA molecular weights ranging from 3.4 kDa to 20 kDa. From Figure 29, DN hydrogels demonstrates higher toughness, ultimate strain and compressive strength than their SN counterparts for all compositions of this study. Among them, DN-hydrogel consisting 6 mol.% bisacrylamide and

$PEGDA_{10k}$ exhibits the highest toughness 0.60 ± 0.03 M J/m^3, the highest ultimate compressive strength 3.47 ± 0.35 MPa, ultimate strain of 0.592 ± 0.127 mm/mm, and elastic modulus of 1.04 ± 0.09 MPa. As summarized in Table 2, DN-hydrogels with this composition demonstrated significant increase ($p < 0.0001$) in mechanical properties compared to those of SN-hydrogels

Table 2: Summary of mechanical property of SN and DN-hydrogel of $PEGDA_{10K}$ and 6 mol.% bisacrylamide

	Compressive Strength (MPa)	Ultimate Compressive Strain (mm/mm)	Toughness (J/m^3)	Elastic Modulus (MPa)
Single Network	1.09 ± 0.04	0.451 ± 0.004	0.11 ± 0.04	0.60 ± 0.02
Double Network	3.47 ± 0.35	0.592 ± 0.127	0.60 ± 0.03	1.04 ± 0.09

Figure 30 shows representative stress-strain curves for DN and SN-hydrogels consisting $PEGDA_{10k}$ and 6 mol.% bisacrylamide. DN-hydrogels of this composition was used to perform subsequent studies including mineralized macroporous hydrogel synthesis and other characterizations in this work.

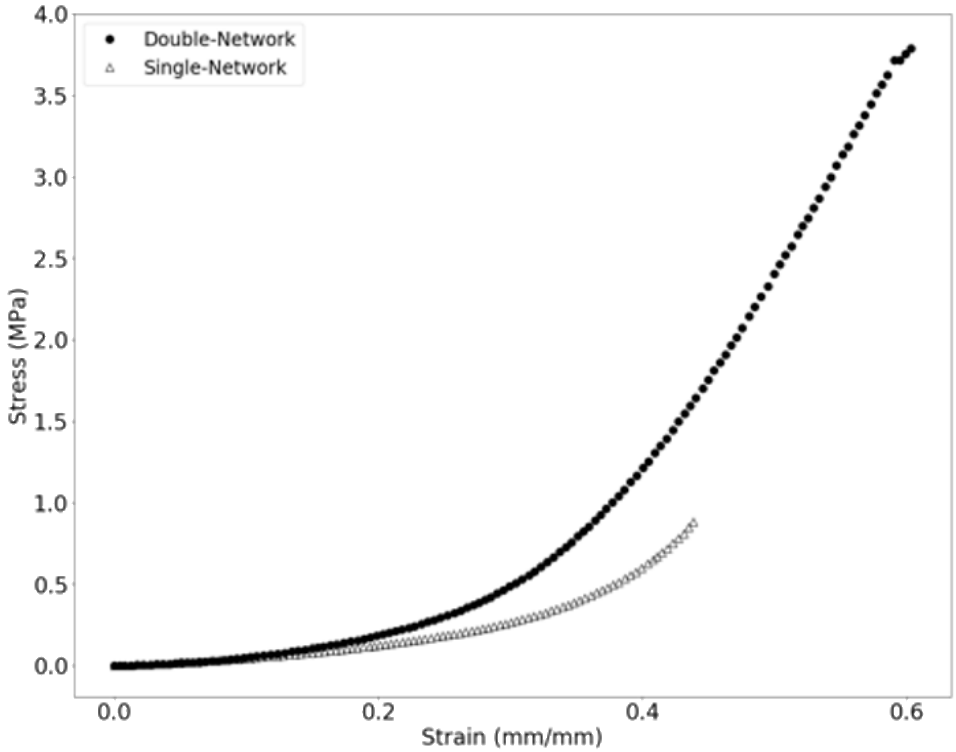

Figure 30: Stress-strain curve of SN and DN-hydrogel with 6 mol. % Bisacrylamide and PEGDA$_{10k}$

As illustrated in Figure 29, for DN-hydrogels made from PEGDA with Mw of 3.4 kDa, 6 kDa and 10 kDa, their toughness, compressive strength, and elastic modulus increase as bisacrylamide concentration increases, while ultimate compressive strain decreases as bisacrylamide concentration increases. With higher crosslinking density of the first network, DN-hydrogel demonstrates enhanced elastic modulus, compressive strength and toughness possibly due to the increase of brittleness in the first network and presumably more effective energy dissipations through this network, and lower ultimate strain could also be a result of increase in brittleness of first network. In contrast, with the decrease in crosslinking density of second network due to increased

PEGDA molecular weight, increased compressive strength, toughness and ultimate strain were observed.

The only exception of this trend occurs for DN-hydrogels with $PEGDA_{20k}$ when bisacrylamide concentration was increased from 4 mol.% to 6 mol.%, toughness and ultimate compressive strength of the hydrogels both start to decrease. Also, DN-hydrogels with $PEGDA_{20k}$ demonstrated decrease in strength and toughness than DN-hydrogels with $PEGDA_{10k}$ with the same bisacrylamide concentration. It is noteworthy that these decreases may be caused by the decreased ability of the PEGDA precursor of highest molecular weight to diffuse into the first network with highest crosslinker concentration (6 mol.%). As demonstrated previous DN-hydrogel studies, the increase in the mechanical strength of the DN hydrogels is a result of synergistic effects of an optimal binary combination of a suitable brittleness of the first network and a ductility of the second network [270], and toughening in DN hydrogels has been shown to occur with the formation of a network configuration consisting of a more tightly crosslinked first network with a more loosely crosslinked second network, with molar ratio of the second network to the first network in the range of serval tens[257]. Owing to the polyelectrolyte nature of A6ACA (high osmotic ionic pressure), the first network was highly swelled in the second monomer solution (PEGDA) during the synthesis process, therefore the first network was highly extended in the final product and the amount of the second network in the final product would be in large excess to that of the first

network. However, for PEGDA with molecular weight of 20 kDa, the total amount of second network could be greatly limited by the decreased diffusion ability of PEGDA into the pre-formed first network, causing final product to exhibit declined mechanical properties comparing to DN networks of other compositions.

5.3.2 Swelling ratios of DN-hydrogels

The ability of a scaffold to retain water is an essential index to evaluate its property for tissue engineering [281]. In this study, swelling ratios of all DN-hydrogels were examined and present in Figure 31. As evident from Figure 31, swelling ratio of DN-hydrogel was shown to decrease as bisacrylamide concentration of the first network increases, but increase as molecular weight of PEGDA increases. Highest swelling ratio (1948 ± 12%) was observed at 2% bisacrylamide-PEGDA$_{20k}$, while the lowest was observed at 6% bisacrylamide-PEGDA$_{3.4k}$ (569 ± 20%).

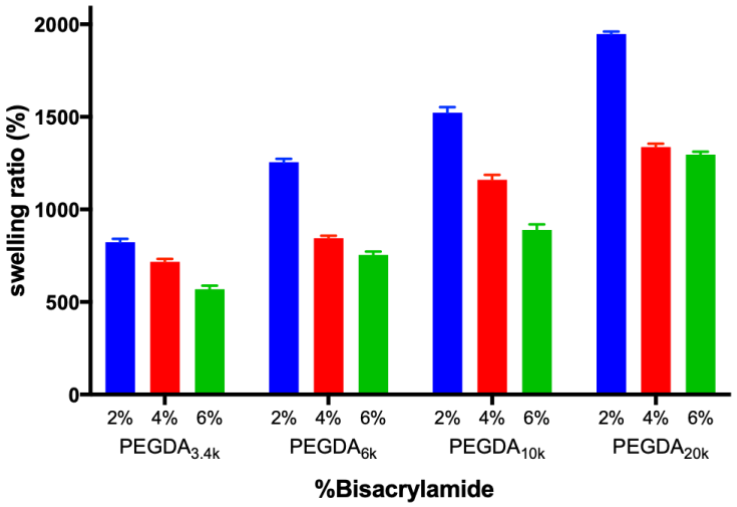

Figure 31: Swelling ratios of DN-hydrogels of varying compositions.

The structure and swelling property of DN-hydrogels are affected by molecular weight and cross-linker concentrations of the precursor solutions of underlying networks. Mesh size (ξ), which defines the average distance between adjacent polymer crosslinks, is a linear measure of the free space available between polymer chains for diffusion[282]. Mesh size increases with polymer molecular weight. For instance, studies have shown that mesh size of PEG increased from 7.6 nm to 16 nm as its molecular weight increases from 860 Da to 10 kDa [283]. In addition, mesh size increases as polymer (or crosslinker agent) concentration decreases. Previous studies have shown that mesh size increases from 6–8 to 14–16 nm when the concentration of 3 kDa PEG decreases from 20 to 10% (w/v) [284,285]. Another basic parameter that describes hydrogels is average molecular weight between crosslinks (*M*c). Similar to mesh size, *M*c describes the degree of crosslinking of hydrogels[286]. Previous studies shows that the volumetric swelling ratio increases with PEG molecular weight [283,287] and decreases with PEG concentration [284,288,289].

When exposed to aqueous solvents, crosslinked network of hydrogels swells, and network chains deform. During this process, two opposing forces develop: retractive (elastic) forces of the polymer chain and swelling forces of the network. Equilibrium state of hydrogels is achieved when these two forces are balanced[290]. A more tightly crosslinked polymer network have higher retractive forces, therefore resulting in less water being imbibed within the hydrogel at equilibrium state [291].

5.3.3 Surface topography and mineral dissolution kinetics

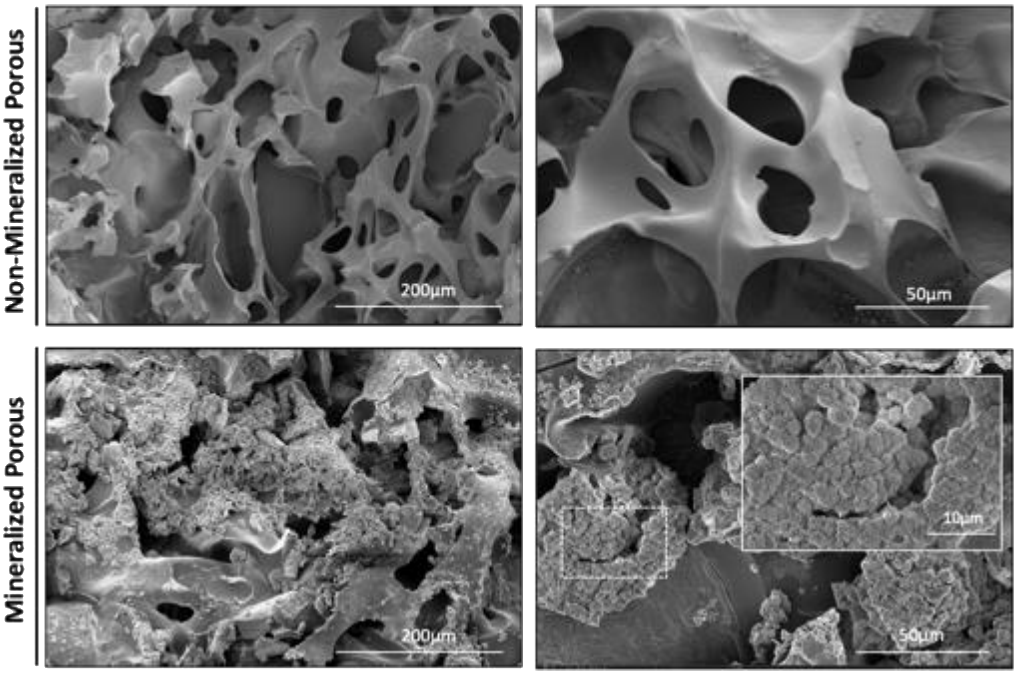

Figure 32: SEM images of non-mineralize/mineralized porous DN-hydrogels. Upper): Nonmineralized porous matrix and (Lower) mineralized porous matrix. Scale bar: 200 µm (left column), 50 µm (right column) and 10 µm (inset)

Using the composition identified through mechanical testing (bisacrylamide 6% - $PEGDA_{10k}$), mineralized macroporous hydrogels were synthesized and characterized using SEM for pore architecture and surface morphology. SEM imaging confirmed that hydrogels exhibited interconnected pore structure (Figure 32). Moreover, there are abundant plate-shape mineral bound to the surface of mineralized hydrogels.

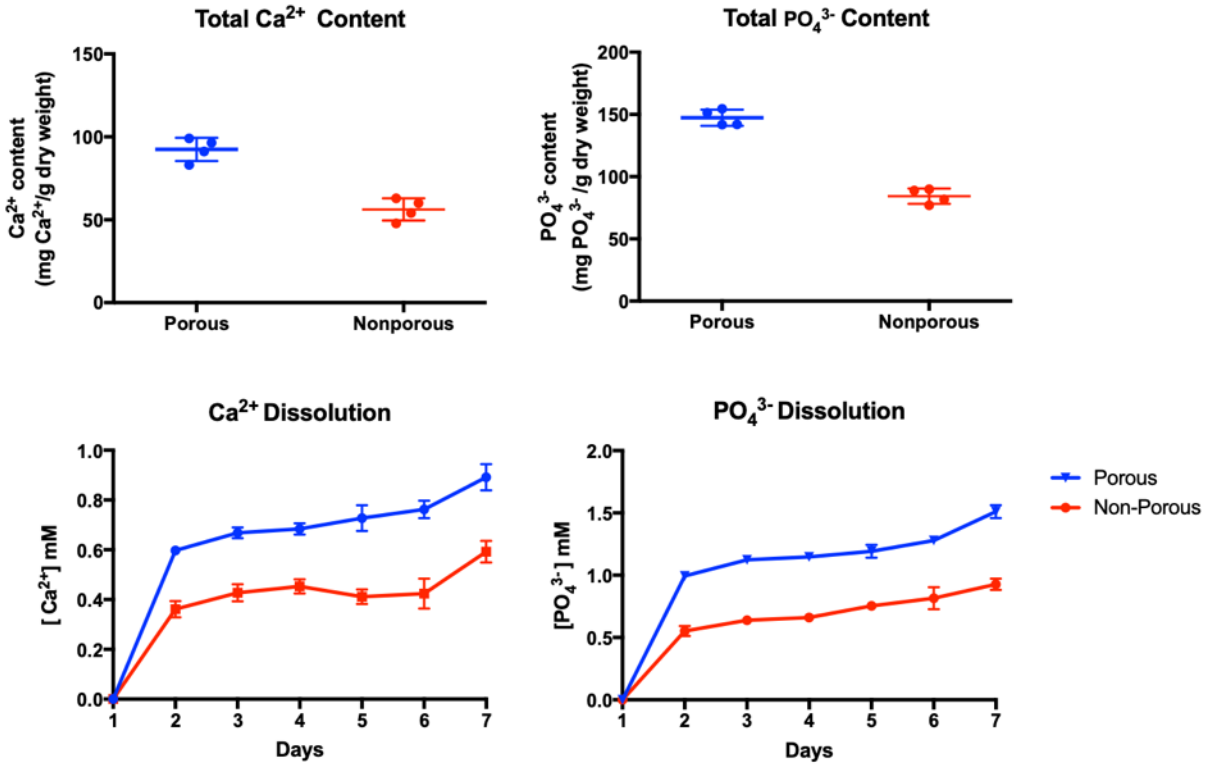

Figure 33: Mineral contents and dissolution kinetics of A6ACA-PEGDA DN-hydrogels. (A) Mineral content measurements and (B) Calcium Phosphate dissolution profile of nonporous and porous DN-hydrogels

As shown in Figure 33A, these mineral crystals consist of Ca^{2+} and PO_4^{3-} components and are able to undergo dissolution process. The amounts of Ca^{2+} were estimated to be 92.45 ± 6.10 mg/g and 56.21 ± 5.8 mg/g in porous and nonporous scaffolds respectively. Concomitantly, the amounts of PO_4^{3-} were estimated to be 147.459 ± 5.64 mg/g and 84.4512 ± 5.30 mg/g in porous and nonporous scaffolds. The increased mineral content in porous scaffolds is a result of surface area increase due to the introduction of macroporous architecture.

As illustrated in Figure 33B, both Ca^{2+} and PO_4^{3-} bound to the DN-hydrogel were released from the mineralized porous and nonporous DN-scaffolds. The molar ratio between the released Ca^{2+} and PO_4^{3-} was estimated to be ~1.6 ± 0.2 (averaged over 7 days) for both porous and non-porous hydrogels. This is very close to the stoichiometric Ca/P ratio in hydroxyapatite (1.67) suggesting that the Ca^{2+} and PO_4^{3-} release could be due to the dissolution of an apatite-like calcium phosphate phase from the mineralized hydrogel. Moreover, porous groups demonstrated higher Ca^{2+} and PO_4^{3-} contents than nonporous groups (Figure 33B), the molar ratio between porous and nonporous stays relatively constant (~ 1.65 ± 0.1) throughout the study, suggesting that this difference may be caused by the difference of total amounts of these minerals present on the DN-hydrogels.

Dissolutions and reprecipitations of CaP minerals of material bound minerals are essential for recapitulating many osteoconductive and osteoinductive cues relevant for bone regeneration *in vitro* and *in vivo*[52-56]. Biomineralized materials are also well established for their ability to adsorb and regulate growth factor signaling. For instance, CaP minerals are known to adsorb osteoinductive growth factors such as bone morphogenic proteins (BMPs) both *in vitro* and *in vivo*[19,44], suggesting their potential use as delivery vehicles for such growth factors. An illustrative example was provided in a recent study by Lee *et al*. in which multiple proteins were adsorbed and delivered from CaP multi-layers in a controllable manner[45]. In addition to the inherent growth factor

adsorption capacity, dissolution and reprecipitation of matrix bound CaP can also sequester and release osteoinductive growth factors. A recent work by Suarez *et al*. showed that release kinetics of BMP-2 was highly dictated by the dissolution of CaP moieties[48,49]. Dissolution of matrix bound minerals leads to release of adsorbed growth factor that could stimulate osteogenic differentiation of stem cells.

5.3.4 Mechanical properties of (non)mineralized (non)porous DN/SN-hydrogels

Mechanical properties of mineralized SN and DN- hydrogel with macroporous architecture were examined and compared. Representative compressive stress-strain curves of mineralized/non-mineralized, porous/nonporous hydrogels are present in Figure 34A (DN) and Figure 34B (SN). For both DN and SN-hydrogels, porous hydrogels demonstrated declined compressive strength, toughness and elastic modulus than their nonporous counterparts (Figure 34C). Introduction of macroporous structure leads to decrease in material volumes, therefore resulting in decrease of these mechanical properties.

For both porous and non-porous hydrogels, DN hydrogels exhibit significantly higher compressive strength, toughness and elastic modulus ($p < 0.0001$) than SN-hydrogels. Moreover, mineralized groups displayed similar mechanical properties as the non-mineralized group, suggesting that CaP minerals bound to the surface of hydrogels have limited impact on the mechanical properties of the hydrogels.

When comparing the compressive strain and elastic modulus between porous and nonporous hydrogels in Figure 34, it is noteworthy that although porous SN-hydrogel are capable of more than 80% compressive strain without fracture, this high ultimate strain is a result of pore collapse at very low load due to the low elastic modulus of SN hydrogels. As manifested in Figure 34C, the overall elastic modulus of porous SN-hydrogel (~41kPa) is an order of magnitude lower than that of DN porous hydrogels (~450kPa).

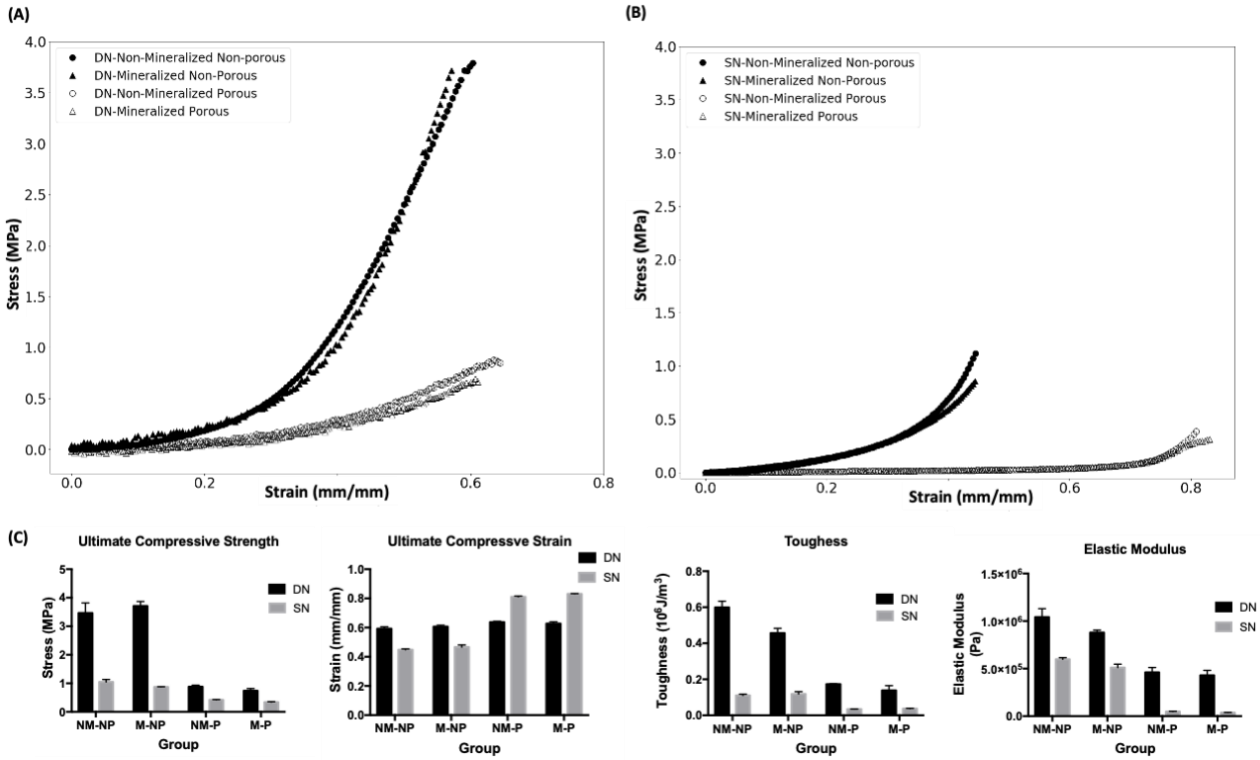

Figure 34: Mechanical properties of (non)mineralized (non)porous DN and SN hydrogels. Stress-strain curves of (A) DN hydrogels and (B) SN hydrogels. (C) Ultimate compressive strength, ultimate compressive strain, toughness, and elastic modulus comparison between DN and SN-hydrogels (M: Mineralized; NM: Nonmineralized; P: porous; NP: nonporous). Despite decline in mechanical properties,

interconnected macroporous architecture of DN-hydrogels is crucial for the biological functionalities for bone engineering scaffolds. Bone regeneration in a scaffold *in vivo* involves recruitments of endogenous cells from the surrounding environments, and vascularization throughout the scaffolds. Higher porosity is expected to enhance osteogenesis, since larger surface area results in higher ion exchange and bone-inducing factor adsorption[292,293]. Furthermore, materials with interconnected pore architecture are advantageous over biomaterials containing dead-end pores, because a spatial continuous connection of the pore system is crucial for the ingrowth of new bone in long-term tissue interface maintenance [294].

5.4 Conclusions

In this chapter, a novel tough double network A6ACA-PEGDA hydrogel is proposed. By varying crosslinker concentrations and molecular weights of polymer components, A6ACA-PEGDA DN-hydrogels with different compositions were prepared, and their mechanical properties were studied and compared to the SN-hydrogels of the same compositions. The introduction of asymmetric double network structure enhanced the toughness, ultimate compressive strength and ultimate compressive strain of the A6ACA-PEGDA hydrogels. In the meantime, functional groups on A6ACA moieties are able to carry out biomineralization when exposed to appropriate conditions in the proposed DN-hydrogels. The CaP minerals bound to the DN-hydrogels can undergo dissolution, which could recapitulate certain aspects of

dynamic mineral environments of native bone. Macroporous pore architectures can be introduced to the DN-hydrogels, which could enhance relevant cellular and biological interactions for bone regeneration *in vivo*. The tough DN hydrogel described in this chapter could potentially be used for bone tissue engineering applications.

6. Chapter 6: Future Directions

The findings demonstrated in this dissertation showed osteoinductivity and osteoconductivity of bone-mimetic biomineralized materials to support *in vivo* bone regeneration and bone tissue regeneration. Chemical properties such as presence of calcium phosphate moieties is essential in activation of endogenous osteoprogenitor cells and their subsequential osteogenic differentiation to form bone tissue. In addition, structural parameter such as pore size plays an important role in biomaterials-mediated bone tissue repair by affecting cell recruitment, infiltration and vascularization of the scaffolds. Furthermore, host tissue microenvironments affect the effectiveness of the osteoconductivity of these materials, manifested by an age-dependent pattern in orthotopic bone regeneration demonstrated in this dissertation. Finally, mechanical properties of the biomineralized materials can be enhanced through creating a double-network hydrogel system.

As an extension of these works, the osteoconductivity of biomineralized materials could lead to functional bone tissue engineering for translational applications. In addition, the biomineralized materials presented in this dissertation can be utilized as *in vitro* platform for investigating the underlying mechanisms and interactions among tissue microenvironments, biophysical properties of the biomineralized materials and bone regeneration effectiveness in a fundamental

perspective. This chapter discuss future directions of studies that could extend from the works presented in this dissertation.

6.1 Evaluation of biomineralized scaffolds

Evaluation of the biomineralized scaffolds in additional healing models is a direction that warrants immediate investigation. The works demonstrated in this dissertation showed the applications of the biomineralized scaffolds in a cranial orthotopic defect model and a subcutaneous ectopic bone induction model. The results showed highly promising findings and it is important to investigate the applications of biomineralized scaffolds in other models such as tibial/femoral segmental defect models, and spinal fusion procedures such as interbody fusions.

Furthermore, the utilization of biomineralized scaffolds for *in vivo* bone tissue regeneration can also be applied to engineering of osteochondral tissue, adding a new dimension to their applications. The biomineralized materials can be combined with additional layers of materials to form multi-phasic hydrogels suitable for osteochondral tissue regeneration. The capacity of the biomineralized materials to activate endogenous cells for bone tissue formation could aid the integration of the engineered osteochondral tissue with native bone. Kang *et al*. have created a cell-loaded tri-layer hydrogel constructs with the biomineralized materials and demonstrated functional osteochondral tissue formation upon subcutaneous

implantation into immunodeficient mouse [295]. However, a drawback of the multi-layered structure is the poor integration among different layers, which leads to eventual delamination and failure of the scaffolds. With introduction of double-network hydrogel demonstrated in this work, a more robust multiphasic structure can be created through two-step synthesis process, where multiple first networks with different compositions or architecture can be integrated to form a robust layered constructure through polymerization of the same second network. Furthermore, enhancements in mechanical properties of the materials through double-network strategy could also lead to wider range of applications and more experimental models such as rabbit osteochondral defect models.

6.2 Investigation of cellular mechanisms underlying age-related osteogenic differentiation and tissue formation

Another important extension of this work is to investigate the biophysical and cellular mechanism underlying the osteogenic differentiation and tissue formation. As demonstrated in this work, age of the host has a significant impact on the effectiveness of biomaterial-mediated *in vivo* bone repair, and the underlying mechanisms causing these changes are areas of study that require further investigations and experimental validations. In general, aging is an important factor that lead to many cellular and microenvironment changes in host tissue. Studies have shown that aging results biological differences in osteoprogenitor cells,

including shifting towards adipogenic phenotype [296,297], and cellular senescence due to oxidative damage and glycation[237,244]. Biomineralized materials demonstrated in this work can be used as an *in vitro* flatform to study the bone formation capacity of different osteoprogenitor cells and their osteogenic differentiation ability to form bone ECM. Furthermore, it has been reported that aging also affects inflammatory responses and relevant cellular activities during bone healing[298-300]. For instance, older macrophages have been shown to demonstrate a more pro-inflammatory phenotype than younger macrophages[298], and cellular factors secreted by young macrophages is able to promote osteoblastic differentiation and enhance bone healing[299,300]. The biomineralized scaffold can be used as a cell substrate to investigate the interaction between macrophage phenotypes and osteoprogenitor cells, and how such interaction may affect bone regeneration capacity.

An additional mechanism that can be investigated is the capacity of biomineralized materials to bind growth factors/proteins. It is well established that calcium phosphate-based materials are able to adsorb osteoinductive proteins/growth factors like bone morphogenic proteins in body fluid. This led to the increase in protein/growth factor concentration within the scaffolds which subsequently enhance the osteoconductivity of the biomaterials to recruit and activate endogenous for bone regeneration[301,302]. A comprehensive study of different

protein adsorption profiles and their binding affinities to the biomineralized materials is the next-step toward understanding the cellular activities involved in the biomineralized material-mediated *in vivo* bone regeneration. Furthermore, the binding mechanism of BMPs to calcium phosphate materials can also be investigated using this biomineralized material. A number of previous studies suggest that bone morphogenic proteins directly bind to calcium phosphates, while other studies also suggest that such binding is through an intermediate reagent fetuin[303,304]. This binding mechanism affects body's endogenous sequestration and storage of pro-osteogenic growth factors and certainly merits further investigations.

6.3 Development of degradable biomineralized scaffolds

In this dissertation, PEGDA-co-A6ACA have been investigated and demonstrated great potential for aiding *in vivo* bone tissue regeneration. Although PEGDA contains ester bonds which can be cleaved due to acidic or enzymatic mediated hydrolysis, this biomineralized material is still regarded as highly stable and non-biodegradable *in vivo*. Creating degradable synthetic materials that resemble the osteoinductivity and osteoconductivity of PEGDA-co-A6A6A but allow gradual replacement of scaffold materials with newly formed engineered bone tissue is an essential step towards maintenance of long-term of bone functions.

The rate of degradation is an important design factor governing the *in vivo* functionalities of the biomaterials. Excessively high degradation rate may cause

premature loss of the material-based cues relevant for bone formation, whereas an excessively low degradation rate may hinder neo-bone formation and remodeling of bone due to the occupying of space[305]. A good strategy for the development of degradable scaffolds involves recapitulating the native bone resorption processes, where osteoclasts create acidic environment to solubilized minerals, followed by subsequent secretion of enzymes such as cathepsins K to degrade the underlying osteoid structure [306]. Incorporating moieties cleavable by these specific enzymes enables the synthetic scaffolds to undergo osteoclast-mediated degradation. Biomaterials with enzyme-specific peptide moieties that is able to degrade through particular enzyme action have been reported [307].This strategy offers a feasible option for creating degradable biomineralized material.

6.4 Development of injectable biomineralized scaffolds

The approach demonstrated in this work involved bone reconstruction and regeneration using solid bulk scaffold. However, many orthopedic interventions such as maxillofacial procedures, minimally invasive alternatives are usually required[308-310]. Injectable biomaterials with appropriate functionalities and self-setting/self-assembly characteristics at physiological condition are essential for such bone reconstruction procedures. Therefore, creating an injectable biomineralized materials can expand the use of our materials to more orthopedic conditions.

Recently, microgel-assembled scaffolds have been demonstrated to create heterogeneous tissue mimics, with inclusion of more cues relevant for tissue regeneration. For example, Scott *et al*. have successfully prepared microgel-assembled scaffolds with different microgel components to allow structural supports, porogen and drug delivery functionalities.[311] Moreover, microgels have also been functionalized with cell adhesion peptides for increased cell attachment and accelerated wound healing[312]. Caldwell *et al*.[313] has demonstrated a clickable microgel scaffolds system functionalized with azide and alkyne moieties that can self-assembly into robust and porous scaffold system. [313] The resultant scaffolds have demonstrated excellent biocompatibility and high degree of tunability over mechanical properties[313]. Using a self-assembled microgel system functionalized with mineral binding moieties could be a future direction to create injectable biomineralized bone scaffold.

7. Chapter 7: Conclusions

In summary, the work presented in this dissertation investigates biomineralized material-mediated bone regeneration through leveraging endogenous healing mechanism. I showed the impacts of scaffold minerals, scaffold pore sizes and ages of the hosts on *in vivo* bone formation mediated by the biomineralized materials. In addition, I developed a double-network hydrogel system to enhance the mechanical properties of the biomineralized materials.

In Chapter 3, I demonstrated that biomineralized materials are able to promote *in vivo* bone healing by providing a bone-specific mineral environment to induce osteogenic commitment of recruited host progenitor cells and support the maintenance of cells relevant for the formation and function of bone tissues, resulting in the formation of mature, vascularized bone tissue and complete healing of the defects. In addition, scaffold pore size is a critical structural parameter governing the dynamic processes of cell infiltration and osteo-ingrowth of the mineralized macroporous hydrogels. I found that pore diameters greater than 100 μm are essential for cell infiltration and vascularization within the scaffolds, which ultimately dictates bone tissue in-growth in the scaffold.

In Chapter 4, I used the same system identified in Chapter 3 to study the effects of host age on *in vivo* orthotopic bone formation. I demonstrated that the age of the

recipient has a significant influence on the quantity and quality of the neo-bone tissues characterized in terms of bone mineral deposition and bone tissue-specific markers. Specifically, delayed bone formation and decreased quantity of neo-bone tissue formation were observed in the older recipients

Finally, in Chapter 5, I prepared a mineralized double-network hydrogel by introducing a contrasting double network configuration, while keeping the chemical compositions of the materials close to the biomineralized materials used in Chapter 3-4. I found that mechanical properties of biomineralized materials, including toughness, ultimate compressive strength and strain, can be enhanced through this double-network hydrogel strategy.

Overall, the works described in this dissertation provide a step-forward in advancing the development and optimization of biomaterial properties to harness the regeneration potential of host tissue through leveraging endogenous healing mechanism. Such biomaterial-based strategies provide an effective and easy-to-implement alternative for bone tissue regenerative therapy.

References

1 Baroli, B. From natural bone grafts to tissue engineering therapeutics: Brainstorming on pharmaceutical formulative requirements and challenges. *Journal of Pharmaceutical Sciences* **98**, 1317-1375 (2009).

2 Brinker, M. R. & O'Connor, D. P. The Incidence of Fractures and Dislocations Referred for Orthopaedic Services in a Capitated Population. *JBJS* **86** (2004).

3 Dimitriou, R., Jones, E., McGonagle, D. & Giannoudis, P. V. Bone regeneration: current concepts and future directions. *BMC Med* **9**, 66, doi:10.1186/1741-7015-9-66 (2011).

4 Campana, V. *et al.* Bone substitutes in orthopaedic surgery: from basic science to clinical practice. *Journal of Materials Science: Materials in Medicine* **25**, 2445-2461, doi:10.1007/s10856-014-5240-2 (2014).

5 Wang, Y. *et al.* The predominant role of collagen in the nucleation, growth, structure and orientation of bone apatite. *Nat Mater* **11**, 724-733, doi:10.1038/nmat3362 (2012).

6 Roach, H. I. Why does bone matrix contain non-collagenous proteins? The possible roles of osteocalcin, osteonectin, osteopontin and bone sialoprotein in bone mineralisation and resorption. *Cell Biol Int* **18**, 617-628, doi:10.1006/cbir.1994.1088 (1994).

7 Wegst, U. G. K., Bai, H., Saiz, E., Tomsia, A. P. & Ritchie, R. O. Bioinspired structural materials. *Nature Materials* **14**, 23-36, doi:10.1038/nmat4089 (2015).

8 Blair, H. C. *et al.* Osteoblast Differentiation and Bone Matrix Formation In Vivo and In Vitro. *Tissue Eng Part B Rev* **23**, 268-280, doi:10.1089/ten.TEB.2016.0454 (2017).

9 Charles, J. F. & Aliprantis, A. O. Osteoclasts: more than 'bone eaters'. *Trends Mol Med* **20**, 449-459, doi:10.1016/j.molmed.2014.06.001 (2014).

10 Lichte, P., Pape, H. C., Pufe, T., Kobbe, P. & Fischer, H. Scaffolds for bone healing: Concepts, materials and evidence. *Injury-International Journal of the Care of the Injured* **42**, 569-573, doi:10.1016/j.injury.2011.03.033 (2011).

11 Laurie, S. W. S., Kaban, L. B., Mulliken, J. B. & Murray, J. E. Donor-Site Morbidity after Harvesting Rib and Iliac Bone. *Plastic and Reconstructive Surgery* **73**, 933-938, doi:Doi 10.1097/00006534-198406000-00014 (1984).

12 Giannoudis, P. V., Dinopoulos, H. & Tsiridis, E. Bone substitutes: An update. *Injury* **36**, S20-S27 (2005).

13 Zlotolow, D. A., Vaccaro, A. R., Salamon, M. L. & Albert, T. J. The role of human bone morphogenetic proteins in spinal fusion. *J Am Acad Orthop Surg* **8**, 3-9 (2000).

14 Khan, S. N. *et al.* Use of osteopromotive growth factors, demineralized bone matrix, and ceramics to enhance spinal fusion. *Journal of the American Academy of Orthopaedic Surgeons* **13**, 129-137 (2005).

15 Campana, V. *et al.* Bone substitutes in orthopaedic surgery: from basic science to clinical practice. *J Mater Sci Mater Med* **25**, 2445-2461, doi:10.1007/s10856-014-5240-2 (2014).

16 James, A. W. *et al.* A Review of the Clinical Side Effects of Bone Morphogenetic Protein-2. *Tissue Eng Part B Rev* **22**, 284-297, doi:10.1089/ten.TEB.2015.0357 (2016).

17 Lad, S. P. *et al.* Cancer After Spinal Fusion: The Role of Bone Morphogenetic Protein. *Neurosurgery* **73**, 440-449, doi:10.1227/NEU.0000000000000018 (2013).

18 Carragee, E. J. *et al.* Cancer Risk After Use of Recombinant Bone Morphogenetic Protein-2 for Spinal Arthrodesis. *Journal of Bone and Joint Surgery-American Volume* **95a**, 1537-1545, doi:10.2106/Jbjs.L.01483 (2013).

19 Yuan, H. *et al.* Osteoinduction by calcium phosphate biomaterials. *J Mater Sci Mater Med* **9**, 723-726 (1998).

20 Mygind, T. *et al.* Mesenchymal stem cell ingrowth and differentiation on coralline hydroxyapatite scaffolds. *Biomaterials* **28**, 1036-1047, doi:10.1016/j.biomaterials.2006.10.003 (2007).

21 Müller, P. *et al.* Calcium phosphate surfaces promote osteogenic differentiation of mesenchymal stem cells. *J. Cell. Mol. Med.* **12**, 281-291, doi:10.1111/j.1582-4934.2007.00103.x (2008).

22 Choi, S.-W., Zhang, Y., Thomopoulos, S. & Xia, Y. In Vitro Mineralization by Preosteoblasts in Poly(D, L-lactide-co-glycolide) Inverse Opal Scaffolds Reinforced with Hydroxyapatite Nanoparticles. *Langmuir : the ACS journal of surfaces and colloids* **26**, 12126-12131, doi:10.1021/la101519b (2010).

23 Oyane, A. *et al.* Preparation and assessment of revised simulated body fluids. *J Biomed Mater Res A* **65**, 188-195, doi:10.1002/jbm.a.10482 (2003).

24 Ducheyne, P. & Qiu, Q. Bioactive ceramics: the effect of surface reactivity on bone formation and bone cell function. *Biomaterials* **20**, 2287-2303, doi:10.1016/s0142-9612(99)00181-7 (1999).

25 Roberts, S. J. *et al.* The combined bone forming capacity of human periosteal derived cells and calcium phosphates. *Biomaterials* **32**, 4393-4405, doi:10.1016/j.biomaterials.2011.02.047 (2011).

26 Yuan, H. *et al.* Osteoinductive ceramics as a synthetic alternative to autologous bone grafting. *Proc. Natl. Acad. Sci. U. S. A.* **107**, 13614-13619, doi:10.1073/pnas.1003600107 (2010).

27 Johal, H. S., Buckley, R. E., Le, I. L. & Leighton, R. K. A prospective randomized controlled trial of a bioresorbable calcium phosphate paste (alpha-BSM) in treatment of displaced intra-articular calcaneal fractures. *J Trauma* **67**, 875-882, doi:10.1097/TA.0b013e3181ae2d50 (2009).

28 Moore, W. R., Graves, S. E. & Bain, G. I. Synthetic bone graft substitutes. *ANZ J Surg* **71**, 354-361 (2001).

29 Saiz, E. *et al.* In vitro behavior of silicate glass coatings on Ti6A14V. *Biomaterials* **23**, 3749-3756 (2002).

30 Valerio, P., Pereira, M. M., Goes, A. M. & Leite, M. F. The effect of ionic products from bioactive glass dissolution on osteoblast proliferation and collagen production. *Biomaterials* **25**, 2941-2948, doi:10.1016/j.biomaterials.2003.09.086 (2004).

31 Shkilnyy, A. *et al.* Poly(ethylene imine)-controlled calcium phosphate mineralization. *Langmuir* **24**, 2102-2109, doi:10.1021/la702523p (2008).

32 Song, J., Saiz, E. & Bertozzi, C. R. A new approach to mineralization of biocompatible hydrogel scaffolds: an efficient process toward 3-dimensional bonelike composites. *J Am Chem Soc* **125**, 1236-1243, doi:10.1021/ja028559h (2003).

33 Kretlow, J. D. & Mikos, A. G. Review: mineralization of synthetic polymer scaffolds for bone tissue engineering. *Tissue Eng.* **13**, 927-938, doi:10.1089/ten.2006.0394 (2007).

34 Osathanon, T. *et al.* Microporous nanofibrous fibrin-based scaffolds for bone tissue engineering. *Biomaterials* **29**, 4091-4099, doi:10.1016/j.biomaterials.2008.06.030 (2008).

35 Phadke, A., Zhang, C., Hwang, Y., Vecchio, K. & Varghese, S. Templated mineralization of synthetic hydrogels for bone-like composite materials: role of matrix hydrophobicity. *Biomacromolecules* **11**, 2060-2068, doi:10.1021/bm100425p (2010).

36 Suárez-González, D. *et al.* Controlled nucleation of hydroxyapatite on alginate scaffolds for stem cell-based bone tissue engineering. *J. Biomed. Mater. Res. A* **95**, 222-234, doi:10.1002/jbm.a.32833 (2010).

37 Filmon, R., Grizon, F., Baslé, M. F. & Chappaard, D. Effects of negatively charged groups (carboxymethyl) on the calcification of poly(2-hydroxyethyl methacrylate). *Biomaterials* **23**, 3053-3059 (2002).

38 Murphy, W. L. & Mooney, D. J. Bioinspired growth of crystalline carbonate apatite on biodegradable polymer substrata. *J. Am. Chem. Soc.* **124**, 1910-1917, doi:10.1021/ja012433n (2002).

39 Oyane, A. *et al.* Simple surface modification of poly(epsilon-caprolactone) for apatite deposition from simulated body fluid. *Biomaterials* **26**, 2407-2413, doi:10.1016/j.biomaterials.2004.07.048 (2005).

40 Song, J. *et al.* Elastomeric high-mineral content hydrogel-hydroxyapatite composites for orthopedic applications. *J. Biomed. Mater. Res. A* **89**, 1098-1107, doi:10.1002/jbm.a.32110 (2009).

41 Reichert, J. C. *et al.* A tissue engineering solution for segmental defect regeneration in load-bearing long bones. *Sci. Transl. Med.* **4**, 141ra193, doi:10.1126/scitranslmed.3003720 (2012).

42 Hwang, N. S., Varghese, S., Lee, H. J., Zhang, Z. & Elisseeff, J. Biomaterials directed in vivo osteogenic differentiation of mesenchymal cells derived from human embryonic stem cells. *Tissue Eng. Part A* **19**, 1723-1732, doi:10.1089/ten.TEA.2013.0064 (2013).

43 Yaylaoğlu, M. B., Korkusuz, P., Ors, U., Korkusuz, F. & Hasirci, V. Development of a calcium phosphate-gelatin composite as a bone substitute and its use in drug release. *Biomaterials* **20**, 711-719 (1999).

44 Urist, M. *et al.* Purification of bovine bone morphogenetic protein by hydroxyapatite chromatography. *Proceedings of the National Academy of Sciences* **81**, 371-375 (1984).

45 Lee, J. S., Suarez-Gonzalez, D. & Murphy, W. L. Mineral coatings for temporally controlled delivery of multiple proteins. *Adv Mater* **23**, 4279-4284 (2011).

46 Liu, Y., Layrolle, P., de Bruijn, J., van Blitterswijk, C. & de Groot, K. Biomimetic coprecipitation of calcium phosphate and bovine serum albumin on titanium alloy. *J. Biomed. Mater. Res.* **57**, 327-335 (2001).

47 Liu, Y., Hunziker, E. B., Layrolle, P., De Bruijn, J. D. & De Groot, K. Bone morphogenetic protein 2 incorporated into biomimetic coatings retains its biological activity. *Tissue engineering* **10**, 101-108 (2004).

48 Suárez-González, D., Lee, J. S., Lan Levengood, S. K., Vanderby Jr, R. & Murphy, W. L. Mineral coatings modulate β-TCP stability and enable growth factor binding and release. *Acta Biomater.* **8**, 1117-1124 (2012).

49 Suarez-Gonzalez, D. *et al.* Controllable mineral coatings on PCL scaffolds as carriers for growth factor release. *Biomaterials* **33**, 713-721, doi:10.1016/j.biomaterials.2011.09.095 (2012).

50 Grayson, W. L., Bhumiratana, S., Grace Chao, P. H., Hung, C. T. & Vunjak-Novakovic, G. Spatial regulation of human mesenchymal stem cell differentiation in engineered osteochondral constructs: effects of pre-differentiation, soluble factors and medium perfusion. *Osteoarthritis Cartilage* **18**, 714-723, doi:10.1016/j.joca.2010.01.008 (2010).

51 ter Brugge, P. J., Wolke, J. G. C. & Jansen, J. A. Effect of calcium phosphate coating crystallinity and implant surface roughness on differentiation of rat bone marrow cells. *J. Biomed. Mater. Res.* **60**, 70-78 (2002).

52 Phadke, A., Shih, Y.-R. V. & Varghese, S. Mineralized synthetic matrices as an instructive microenvironment for osteogenic differentiation of human mesenchymal stem cells. *Macromol. Biosci.* **12**, 1022-1032, doi:10.1002/mabi.201100289 (2012).

53 Kang, H. *et al.* Mineralized gelatin methacrylate-based matrices induce osteogenic differentiation of human induced pluripotent stem cells. *Acta Biomater.* **10**, 4961-4970, doi:10.1016/j.actbio.2014.08.010 (2014).

54 Kang, H. *et al.* Biomineralized matrix-assisted osteogenic differentiation of human embryonic stem cells. *J. Mater. Chem. B Mater. Biol. Med.* **2**, 5676-5688, doi:10.1039/C4TB00714J (2014).

55 Wen, C., Kang, H., Shih, Y.-R. V., Hwang, Y. & Varghese, S. In vivo comparison of biomineralized scaffold-directed osteogenic differentiation of human embryonic and mesenchymal stem cells. *Drug Deliv. Transl. Res.* **6**, 121-131, doi:10.1007/s13346-015-0242-2 (2016).

56 Shih, Y.-R. V. *et al.* Calcium phosphate-bearing matrices induce osteogenic differentiation of stem cells through adenosine signaling. *Proc. Natl. Acad. Sci. U. S. A.* **111**, 990-995, doi:10.1073/pnas.1321717111 (2014).

57 Kang, H., Shih, Y.-R. V. & Varghese, S. Biomineralized Matrices Dominate Soluble Cues To Direct Osteogenic Differentiation of Human Mesenchymal Stem Cells through Adenosine Signaling. *Biomacromolecules* **16**, 1050-1061, doi:10.1021/acs.biomac.5b00099 (2015).

58 Fuchs, E., Tumbar, T. & Guasch, G. Socializing with the neighbors: stem cells and their niche. *Cell* **116**, 769-778 (2004).

59 Gumbiner, B. M. Cell Adhesion: The Molecular Basis of Tissue Architecture and Morphogenesis. *Cell* **84**, 345-357, doi:10.1016/S0092-8674(00)81279-9 (1996).

60 Berrier, A. L. & Yamada, K. M. Cell-matrix adhesion. *J. Cell. Physiol.* **213**, 565-573, doi:10.1002/jcp.21237 (2007).

61 Palecek, S. P., Loftus, J. C., Ginsberg, M. H., Lauffenburger, D. A. & Horwitz, A. F. Integrin-ligand binding properties govern cell migration speed through cell-substratum adhesiveness. *Nature* **385**, 537-540, doi:10.1038/385537a0 (1997).

62 Nelson, C. M. & Bissell, M. J. Of extracellular matrix, scaffolds, and signaling: tissue architecture regulates development, homeostasis, and cancer. *Annu. Rev. Cell Dev. Biol.* **22**, 287-309, doi:10.1146/annurev.cellbio.22.010305.104315 (2006).

63 Friedl, P. & Alexander, S. Cancer invasion and the microenvironment: plasticity and reciprocity. *Cell* **147**, 992-1009, doi:10.1016/j.cell.2011.11.016 (2011).

64 Lu, P., Weaver, V. M. & Werb, Z. The extracellular matrix: a dynamic niche in cancer progression. *J Cell Biol* **196**, 395-406, doi:10.1083/jcb.201102147 (2012).

65 Aung, A. *et al.* 3D traction stresses activate protease-dependent invasion of cancer cells. *Biophys J* **107**, 2528-2537, doi:10.1016/j.bpj.2014.07.078 (2014).

66 Nakasaki, M. *et al.* The matrix protein Fibulin-5 is at the interface of tissue stiffness and inflammation in fibrosis. *Nat Commun* **6**, 8574, doi:10.1038/ncomms9574 (2015).

67 Drumheller, P. D. & Hubbell, J. A. Polymer networks with grafted cell adhesion peptides for highly biospecific cell adhesive substrates. *Anal. Biochem.* **222**, 380-388, doi:10.1006/abio.1994.1506 (1994).

68 Neff, J. A., Tresco, P. A. & Caldwell, K. D. Surface modification for controlled studies of cell–ligand interactions. *Biomaterials* **20**, 2377-2393, doi:10.1016/S0142-9612(99)00166-0 (1999).

69 Mosiewicz, K. A. *et al.* In situ cell manipulation through enzymatic hydrogel photopatterning. *Nat Mater* **12**, 1072-1078, doi:10.1038/nmat3766 (2013).

70 Sridhar, B. V. *et al.* Development of a cellularly degradable PEG hydrogel to promote articular cartilage extracellular matrix deposition. *Adv. Healthc. Mater.* **4**, 702-713, doi:10.1002/adhm.201400695 (2015).

71 Varghese, S. *et al.* Chondroitin sulfate based niches for chondrogenic differentiation of mesenchymal stem cells. *Matrix Biol* **27**, 12-21, doi:10.1016/j.matbio.2007.07.002 (2008).

72 Engler, A. J., Sen, S., Sweeney, H. L. & Discher, D. E. Matrix elasticity directs stem cell lineage specification. *Cell* **126**, 677-689, doi:10.1016/j.cell.2006.06.044 (2006).

73 Huebsch, N. *et al.* Matrix elasticity of void-forming hydrogels controls transplanted-stem-cell-mediated bone formation. *Nat Mater* **14**, 1269-1277, doi:10.1038/nmat4407 (2015).

74 Chaudhuri, O. *et al.* Hydrogels with tunable stress relaxation regulate stem cell fate and activity. *Nat Mater* **15**, 326-334, doi:10.1038/nmat4489 (2016).

75 Burdick, J. A. & Vunjak-Novakovic, G. Engineered microenvironments for controlled stem cell differentiation. *Tissue Eng Part A* **15**, 205-219, doi:10.1089/ten.tea.2008.0131 (2009).

76 Ayala, R. *et al.* Engineering the cell-material interface for controlling stem cell adhesion, migration, and differentiation. *Biomaterials* **32**, 3700-3711, doi:10.1016/j.biomaterials.2011.02.004 (2011).

77 Phadke, A. *et al.* Effect of scaffold microarchitecture on osteogenic differentiation of human mesenchymal stem cells. *Eur. Cell. Mater.* **25**, 114-129 (2013).

78 Dalby, M. J., Gadegaard, N. & Oreffo, R. O. Harnessing nanotopography and integrin-matrix interactions to influence stem cell fate. *Nat Mater* **13**, 558-569, doi:10.1038/nmat3980 (2014).

79 Lutolf, M. P. & Hubbell, J. A. Synthetic biomaterials as instructive extracellular microenvironments for morphogenesis in tissue engineering. *Nat. Biotechnol.* **23**, 47-55, doi:10.1038/nbt1055 (2005).

80 Murphy, S. V. & Atala, A. 3D bioprinting of tissues and organs. *Nat Biotechnol* **32**, 773-785, doi:10.1038/nbt.2958 (2014).

81 Rodin, S. *et al.* Clonal culturing of human embryonic stem cells on laminin-521/E-cadherin matrix in defined and xeno-free environment. *Nat Commun* **5**, 3195, doi:10.1038/ncomms4195 (2014).

82 Kim, H. T., Lee, K. I., Kim, D. W. & Hwang, D. Y. An ECM-based culture system for the generation and maintenance of xeno-free human iPS cells. *Biomaterials* **34**, 1041-1050, doi:10.1016/j.biomaterials.2012.10.064 (2013).

83 Lutolf, M. P. & Hubbell, J. A. Synthesis and physicochemical characterization of end-linked poly(ethylene glycol)-co-peptide hydrogels formed by Michael-type addition. *Biomacromolecules* **4**, 713-722, doi:10.1021/bm025744e (2003).

84 Klim, J. R., Li, L., Wrighton, P. J., Piekarczyk, M. S. & Kiessling, L. L. A defined glycosaminoglycan-binding substratum for human pluripotent stem cells. *Nat. Methods* **7**, 989-994, doi:10.1038/nmeth.1532 (2010).

85 Melkoumian, Z. *et al.* Synthetic peptide-acrylate surfaces for long-term self-renewal and cardiomyocyte differentiation of human embryonic stem cells. *Nat. Biotechnol.* **28**, 606-610, doi:10.1038/nbt.1629 (2010).

86 Mei, Y. *et al.* Combinatorial development of biomaterials for clonal growth of human pluripotent stem cells. *Nat. Mater.* **9**, 768-778, doi:10.1038/nmat2812 (2010).

87 Salinas, C. N. & Anseth, K. S. Decorin moieties tethered into PEG networks induce chondrogenesis of human mesenchymal stem cells. *J. Biomed. Mater. Res. A* **90**, 456-464, doi:10.1002/jbm.a.32112 (2009).

88 Hern, D. L. & Hubbell, J. A. Incorporation of adhesion peptides into nonadhesive hydrogels useful for tissue resurfacing. *J Biomed Mater Res* **39**, 266-276 (1998).

89 Pierschbacher, M. D. & Ruoslahti, E. Influence of stereochemistry of the sequence Arg-Gly-Asp-Xaa on binding specificity in cell adhesion. *J Biol Chem* **262**, 17294-17298 (1987).

90 Santiago, L. Y., Nowak, R. W., Peter Rubin, J. & Marra, K. G. Peptide-surface modification of poly(caprolactone) with laminin-derived sequences for adipose-derived stem cell applications. *Biomaterials* **27**, 2962-2969, doi:10.1016/j.biomaterials.2006.01.011 (2006).

91 Lutolf, M. P. *et al.* Synthetic matrix metalloproteinase-sensitive hydrogels for the conduction of tissue regeneration: engineering cell-invasion characteristics. *Proc Natl Acad Sci U S A* **100**, 5413-5418, doi:10.1073/pnas.0737381100 (2003).

92 Burdick, J. A., Chung, C., Jia, X., Randolph, M. A. & Langer, R. Controlled degradation and mechanical behavior of photopolymerized hyaluronic acid networks. *Biomacromolecules* **6**, 386-391, doi:10.1021/bm049508a (2005).

93 Bian, L., Guvendiren, M., Mauck, R. L. & Burdick, J. A. Hydrogels that mimic developmentally relevant matrix and N-cadherin interactions enhance MSC chondrogenesis. *Proceedings of the National Academy of Sciences of the United States of America* **110**, 10117-10122, doi:10.1073/pnas.1214100110 (2013).

94 Highley, C. B., Prestwich, G. D. & Burdick, J. A. Recent advances in hyaluronic acid hydrogels for biomedical applications. *Current Opinion in Biotechnology* **40**, 35-40 (2016).

95 Cai, S., Liu, Y., Zheng Shu, X. & Prestwich, G. D. Injectable glycosaminoglycan hydrogels for controlled release of human basic fibroblast growth factor. *Biomaterials* **26**, 6054-6067, doi:10.1016/j.biomaterials.2005.03.012 (2005).

96 Chang, C.-W. *et al.* Engineering cell-material interfaces for long-term expansion of human pluripotent stem cells. *Biomaterials* **34**, 912-921, doi:10.1016/j.biomaterials.2012.10.020 (2013).

97 Sangaj, N. *et al.* Heparin mimicking polymer promotes myogenic differentiation of muscle progenitor cells. *Biomacromolecules* **11**, 3294-3300, doi:10.1021/bm101041f (2010).

98 Sakiyama-Elbert, S. E. & Hubbell, J. A. Development of fibrin derivatives for controlled release of heparin-binding growth factors. *J Control Release* **65**, 389-402 (2000).

99 Arai, T., Busby, W., Jr. & Clemmons, D. R. Binding of insulin-like growth factor (IGF) I or II to IGF-binding protein-2 enables it to bind to heparin and

extracellular matrix. *Endocrinology* **137**, 4571-4575, doi:10.1210/endo.137.11.8895319 (1996).

100 Benoit, D. S. W. & Anseth, K. S. Heparin functionalized PEG gels that modulate protein adsorption for hMSC adhesion and differentiation. *Acta Biomater.* **1**, 461-470, doi:10.1016/j.actbio.2005.03.002 (2005).

101 Rouet, V. *et al.* A synthetic glycosaminoglycan mimetic binds vascular endothelial growth factor and modulates angiogenesis. *J Biol Chem* **280**, 32792-32800, doi:10.1074/jbc.M504492200 (2005).

102 Pike, D. B. *et al.* Heparin-regulated release of growth factors in vitro and angiogenic response in vivo to implanted hyaluronan hydrogels containing VEGF and bFGF. *Biomaterials* **27**, 5242-5251, doi:10.1016/j.biomaterials.2006.05.018 (2006).

103 Saksela, O., Moscatelli, D., Sommer, A. & Rifkin, D. B. Endothelial cell-derived heparan sulfate binds basic fibroblast growth factor and protects it from proteolytic degradation. *J Cell Biol* **107**, 743-751, doi:10.1083/jcb.107.2.743 (1988).

104 Prokoph, S. *et al.* Sustained delivery of SDF-1alpha from heparin-based hydrogels to attract circulating pro-angiogenic cells. *Biomaterials* **33**, 4792-4800, doi:10.1016/j.biomaterials.2012.03.039 (2012).

105 Seto, S. P., Miller, T. & Temenoff, J. S. Effect of selective heparin desulfation on preservation of bone morphogenetic protein-2 bioactivity after thermal stress. *Bioconjug Chem* **26**, 286-293, doi:10.1021/bc500565x (2015).

106 Kabra, H. *et al.* Biomimetic Material-Assisted Delivery of Human Embryonic Stem Cell Derivatives for Enhanced In Vivo Survival and Engraftment. *ACS Biomater Sci Eng* **1**, 7-12, doi:10.1021/ab500021a (2015).

107 Jha, A. K. *et al.* Enhanced survival and engraftment of transplanted stem cells using growth factor sequestering hydrogels. *Biomaterials* **47**, 1-12, doi:10.1016/j.biomaterials.2014.12.043 (2015).

108 Curran, J. M., Chen, R. & Hunt, J. A. The guidance of human mesenchymal stem cell differentiation in vitro by controlled modifications to the cell substrate. *Biomaterials* **27**, 4783-4793, doi:10.1016/j.biomaterials.2006.05.001 (2006).

109 Keselowsky, B. G., Collard, D. M. & García, A. J. Integrin binding specificity regulates biomaterial surface chemistry effects on cell differentiation. *Proc. Natl. Acad. Sci. U. S. A.* **102**, 5953-5957, doi:10.1073/pnas.0407356102 (2005).

110 Keselowsky, B. G., Collard, D. M. & García, A. J. Surface chemistry modulates focal adhesion composition and signaling through changes in integrin binding. *Biomaterials* **25**, 5947-5954, doi:10.1016/j.biomaterials.2004.01.062 (2004).

111 Benoit, D. S., Schwartz, M. P., Durney, A. R. & Anseth, K. S. Small functional groups for controlled differentiation of hydrogel-encapsulated human mesenchymal stem cells. *Nat Mater* **7**, 816-823, doi:10.1038/nmat2269 (2008).

112 Mammoto, T. & Ingber, D. E. Mechanical control of tissue and organ development. *Development* **137**, 1407-1420, doi:10.1242/dev.024166 (2010).

113 Wozniak, M. A. & Chen, C. S. Mechanotransduction in development: a growing role for contractility. *Nat. Rev. Mol. Cell Biol.* **10**, 34-43, doi:10.1038/nrm2592 (2009).

114 Paszek, M. J. & Weaver, V. M. The tension mounts: mechanics meets morphogenesis and malignancy. *J. Mammary Gland Biol. Neoplasia* **9**, 325-342, doi:10.1007/s10911-004-1404-x (2004).

115 Ingber, D. E. Cellular mechanotransduction: putting all the pieces together again. *FASEB J.* **20**, 811-827, doi:10.1096/fj.05-5424rev (2006).

116 Balaban, N. Q. *et al.* Force and focal adhesion assembly: a close relationship studied using elastic micropatterned substrates. *Nat Cell Biol* **3**, 466-472, doi:10.1038/35074532 (2001).

117 Galbraith, C. G., Yamada, K. M. & Sheetz, M. P. The relationship between force and focal complex development. *J. Cell Biol.* **159**, 695-705, doi:10.1083/jcb.200204153 (2002).

118 Martinac, B. Mechanosensitive ion channels: molecules of mechanotransduction. *J. Cell Sci.* **117**, 2449-2460, doi:10.1242/jcs.01232 (2004).

119 Wang, N., Butler, J. P. & Ingber, D. E. Mechanotransduction across the cell surface and through the cytoskeleton. *Science* **260**, 1124-1127 (1993).

120 Shih, Y.-R. V., Tseng, K.-F., Lai, H.-Y., Lin, C.-H. & Lee, O. K. Matrix stiffness regulation of integrin-mediated mechanotransduction during osteogenic differentiation of human mesenchymal stem cells. *J. Bone Miner. Res.* **26**, 730-738, doi:10.1002/jbmr.278 (2011).

121 Fu, J. *et al.* Mechanical regulation of cell function with geometrically modulated elastomeric substrates. *Nat. Methods* **7**, 733-736, doi:10.1038/nmeth.1487 (2010).

122 Schlaepfer, D. D., Hauck, C. R. & Sieg, D. J. Signaling through focal adhesion kinase. *Prog. Biophys. Mol. Biol.* **71**, 435-478, doi:10.1016/S0079-6107(98)00052-2 (1999).

123 Kim, I. L., Khetan, S., Baker, B. M., Chen, C. S. & Burdick, J. A. Fibrous hyaluronic acid hydrogels that direct MSC chondrogenesis through mechanical and adhesive cues. *Biomaterials* **34**, 5571-5580, doi:10.1016/j.biomaterials.2013.04.004 (2013).

124 Marklein, R. A. & Burdick, J. A. Spatially controlled hydrogel mechanics to modulate stem cell interactions. *Soft Matter* **6**, 136-143, doi:10.1039/B916933D (2009).

125 Lin, S., Sangaj, N., Razafiarison, T., Zhang, C. & Varghese, S. Influence of physical properties of biomaterials on cellular behavior. *Pharm Res* **28**, 1422-1430, doi:10.1007/s11095-011-0378-9 (2011).

126 Awad, H. A., Wickham, M. Q., Leddy, H. A., Gimble, J. M. & Guilak, F. Chondrogenic differentiation of adipose-derived adult stem cells in agarose, alginate, and gelatin scaffolds. *Biomaterials* **25**, 3211-3222, doi:10.1016/j.biomaterials.2003.10.045 (2004).

127 Zhang, C., Aung, A., Liao, L. & Varghese, S. A novel single precursor-based biodegradable hydrogel with enhanced mechanical properties. *Soft Matter* **5**, 3831-3834, doi:10.1039/B912102A (2009).

128 Gilbert, P. M. *et al.* Substrate elasticity regulates skeletal muscle stem cell self-renewal in culture. *Science* **329**, 1078-1081, doi:10.1126/science.1191035 (2010).

129 Saha, K. *et al.* Substrate modulus directs neural stem cell behavior. *Biophys. J.* **95**, 4426-4438, doi:10.1529/biophysj.108.132217 (2008).

130 Evans, N. D. *et al.* Substrate stiffness affects early differentiation events in embryonic stem cells. *Eur. Cell. Mater.* **18**, 1-13; discussion 13-14 (2009).

131 Huebsch, N. *et al.* Harnessing traction-mediated manipulation of the cell/matrix interface to control stem-cell fate. *Nat. Mater.* **9**, 518-526, doi:10.1038/nmat2732 (2010).

132 Khetan, S. *et al.* Degradation-mediated cellular traction directs stem cell fate in covalently crosslinked three-dimensional hydrogels. *Nat Mater* **12**, 458-465, doi:10.1038/nmat3586 (2013).

133 Her, G. J. *et al.* Control of three-dimensional substrate stiffness to manipulate mesenchymal stem cell fate toward neuronal or glial lineages. *Acta Biomater.* **9**, 5170-5180, doi:10.1016/j.actbio.2012.10.012 (2013).

134 Kloxin, A. M., Kasko, A. M., Salinas, C. N. & Anseth, K. S. Photodegradable hydrogels for dynamic tuning of physical and chemical properties. *Science* **324**, 59-63, doi:10.1126/science.1169494 (2009).

135 Salasznyk, R. M., Klees, R. F., Boskey, A. & Plopper, G. E. Activation of FAK is necessary for the osteogenic differentiation of human mesenchymal stem cells on laminin-5. *J Cell Biochem* **100**, 499-514, doi:10.1002/jcb.21074 (2007).

136 Dupont, S. *et al.* Role of YAP/TAZ in mechanotransduction. *Nature* **474**, 179-183, doi:10.1038/nature10137 (2011).

137 Lian, I. *et al.* The role of YAP transcription coactivator in regulating stem cell self-renewal and differentiation. *Genes Dev* **24**, 1106-1118, doi:10.1101/gad.1903310 (2010).

138 Storm, C., Pastore, J. J., MacKintosh, F. C., Lubensky, T. C. & Janmey, P. A. Nonlinear elasticity in biological gels. *Nature* **435**, 191-194, doi:10.1038/nature03521 (2005).

139 Guvendiren, M. & Burdick, J. A. Stiffening hydrogels to probe short- and long-term cellular responses to dynamic mechanics. *Nat. Commun.* **3**, 792, doi:10.1038/ncomms1792 (2012).

140 Birk, D. E., Zycband, E. I., Winkelmann, D. A. & Trelstad, R. L. Collagen fibrillogenesis in situ: fibril segments are intermediates in matrix assembly. *Proc. Natl. Acad. Sci. U. S. A.* **86**, 4549-4553 (1989).

141 Stevens, M. M. & George, J. H. Exploring and engineering the cell surface interface. *Science* **310**, 1135-1138, doi:10.1126/science.1106587 (2005).

142 Juliano, R. L. & Haskill, S. Signal transduction from the extracellular matrix. *J Cell Biol* **120**, 577-585 (1993).

143 Hahn, M. S., Miller, J. S. & West, J. L. Three-Dimensional Biochemical and Biomechanical Patterning of Hydrogels for Guiding Cell Behavior. *Advanced Materials* **18**, 2679-2684, doi:10.1002/adma.200600647 (2006).

144 DeForest, C. A. & Tirrell, D. A. A photoreversible protein-patterning approach for guiding stem cell fate in three-dimensional gels. *Nat Mater* **14**, 523-531, doi:10.1038/nmat4219 (2015).

145 Théry, M. Micropatterning as a tool to decipher cell morphogenesis and functions. *J. Cell Sci.* **123**, 4201-4213, doi:10.1242/jcs.075150 (2010).

146 Markert, L. D. a. *et al.* Identification of distinct topographical surface microstructures favoring either undifferentiated expansion or differentiation of murine embryonic stem cells. *Stem Cells Dev.* **18**, 1331-1342, doi:10.1089/scd.2009.0114 (2009).

147 Guvendiren, M. & Burdick, J. A. The control of stem cell morphology and differentiation by hydrogel surface wrinkles. *Biomaterials* **31**, 6511-6518, doi:10.1016/j.biomaterials.2010.05.037 (2010).

148 Nur-E-Kamal, A., Ahmed, I., Kamal, J., Schindler, M. & Meiners, S. Three-dimensional nanofibrillar surfaces promote self-renewal in mouse embryonic stem cells. *Stem Cells* **24**, 426-433, doi:10.1634/stemcells.2005-0170 (2006).

149 Ji, L., LaPointe, V. L. S., Evans, N. D. & Stevens, M. M. Changes in embryonic stem cell colony morphology and early differentiation markers driven by colloidal crystal topographical cues. *Eur. Cell. Mater.* **23**, 135-146 (2012).

150 McMurray, R. J. *et al.* Nanoscale surfaces for the long-term maintenance of mesenchymal stem cell phenotype and multipotency. *Nat. Mater.* **10**, 637-644, doi:10.1038/nmat3058 (2011).

151 Dalby, M. J. *et al.* The control of human mesenchymal cell differentiation using nanoscale symmetry and disorder. *Nat. Mater.* **6**, 997-1003, doi:10.1038/nmat2013 (2007).

152 Oh, S. *et al.* Stem cell fate dictated solely by altered nanotube dimension. *Proc. Natl. Acad. Sci. U. S. A.* **106**, 2130-2135, doi:10.1073/pnas.0813200106 (2009).

153 Dang, J. M. & Leong, K. W. Myogenic Induction of Aligned Mesenchymal Stem Cell Sheets by Culture on Thermally Responsive Electrospun Nanofibers. *Adv. Mater.* **19**, 2775-2779, doi:10.1002/adma.200602159 (2007).

154 Muraglia, A., Cancedda, R. & Quarto, R. Clonal mesenchymal progenitors from human bone marrow differentiate in vitro according to a hierarchical model. *J. Cell Sci.* **113 (Pt 7)**, 1161-1166 (2000).

155 Yim, E. K. F., Pang, S. W. & Leong, K. W. Synthetic nanostructures inducing differentiation of human mesenchymal stem cells into neuronal lineage. *Exp. Cell Res.* **313**, 1820-1829, doi:10.1016/j.yexcr.2007.02.031 (2007).

156 Ankam, S. *et al.* Substrate topography and size determine the fate of human embryonic stem cells to neuronal or glial lineage. *Acta Biomater.* **9**, 4535-4545, doi:10.1016/j.actbio.2012.08.018 (2013).

157 Lovmand, J. *et al.* The use of combinatorial topographical libraries for the screening of enhanced osteogenic expression and mineralization. *Biomaterials* **30**, 2015-2022 (2009).

158 Chen, W. *et al.* Nanotopography influences adhesion, spreading, and self-renewal of human embryonic stem cells. *ACS Nano* **6**, 4094-4103, doi:10.1021/nn3004923 (2012).

159 Arnold, M. *et al.* Activation of integrin function by nanopatterned adhesive interfaces. *Chemphyschem* **5**, 383-388, doi:10.1002/cphc.200301014 (2004).

160 Gerecht, S. *et al.* The effect of actin disrupting agents on contact guidance of human embryonic stem cells. *Biomaterials* **28**, 4068-4077, doi:10.1016/j.biomaterials.2007.05.027 (2007).

161 Levingstone, T. J., Matsiko, A., Dickson, G. R., O'Brien, F. J. & Gleeson, J. P. A biomimetic multi-layered collagen-based scaffold for osteochondral repair. *Acta Biomaterialia* **10**, 1996-2004 (2014).

162 O'Keefe, R. J. & Mao, J. Bone Tissue Engineering and Regeneration: From Discovery to the Clinic—An Overview. *Tissue Engineering Part B: Reviews* **17**, 389-392, doi:10.1089/ten.teb.2011.0475 (2011).

163 Lepperdinger, G. *et al.* Changes of the Functional Capacity of Mesenchymal Stem Cells due to Aging or Age-Associated Disease – Implications for Clinical Applications and Donor Recruitment. *Transfusion Medicine and Hemotherapy* **35**, 299-305, doi:10.1159/000142373 (2008).

164 Moerman, E. J., Teng, K., Lipschitz, D. A. & Lecka-Czernik, B. Aging activates adipogenic and suppresses osteogenic programs in mesenchymal marrow stroma/stem cells: the role of PPAR-γ2 transcription factor and TGF-β/BMP signaling pathways. *Aging Cell* **3**, 379-389, doi:10.1111/j.1474-9728.2004.00127.x (2004).

165 Karageorgiou, V. & Kaplan, D. Porosity of 3D biomaterial scaffolds and osteogenesis. *Biomaterials* **26**, 5474-5491, doi:10.1016/j.biomaterials.2005.02.002 (2005).

166 Hollister, S. J. Porous scaffold design for tissue engineering. *Nat. Mater.* **4**, 518-524, doi:10.1038/nmat1421 (2005).

167 Salerno, A., Di Maio, E., Iannace, S. & Netti, P. A. Tailoring the pore structure of PCL scaffolds for tissue engineering prepared via gas foaming of multi-phase blends. *J. Porous Mater.* **19**, 181-188, doi:10.1007/s10934-011-9458-9 (2012).

168 Causa, F., Netti, P. A. & Ambrosio, L. A multi-functional scaffold for tissue regeneration: the need to engineer a tissue analogue. *Biomaterials* **28**, 5093-5099, doi:10.1016/j.biomaterials.2007.07.030 (2007).

169 Kühne, J. H. *et al.* Bone formation in coralline hydroxyapatite. Effects of pore size studied in rabbits. *Acta Orthop. Scand.* **65**, 246-252 (1994).

170 Tsuruga, E., Takita, H., Itoh, H., Wakisaka, Y. & Kuboki, Y. Pore size of porous hydroxyapatite as the cell-substratum controls BMP-induced osteogenesis. *J. Biochem.* **121**, 317-324 (1997).

171 Gauthier, O., Bouler, J. M., Aguado, E., Pilet, P. & Daculsi, G. Macroporous biphasic calcium phosphate ceramics: influence of macropore diameter and macroporosity percentage on bone ingrowth. *Biomaterials* **19**, 133-139 (1998).

172 von Doernberg, M.-C. *et al.* In vivo behavior of calcium phosphate scaffolds with four different pore sizes. *Biomaterials* **27**, 5186-5198, doi:10.1016/j.biomaterials.2006.05.051 (2006).

173 Mastrogiacomo, M. *et al.* Role of scaffold internal structure on in vivo bone formation in macroporous calcium phosphate bioceramics. *Biomaterials* **27**, 3230-3237, doi:10.1016/j.biomaterials.2006.01.031 (2006).

174 Lee, S. J., Lee, I. W., Lee, Y. M., Lee, H. B. & Khang, G. Macroporous biodegradable natural/synthetic hybrid scaffolds as small intestine submucosa impregnated poly (D, L-lactide-co-glycolide) for tissue-engineered bone. *J. Biomater. Sci. Polym. Ed.* **15**, 1003-1017 (2004).

175 Lin, C.-Y. *et al.* Functional bone engineering using ex vivo gene therapy and topology-optimized, biodegradable polymer composite scaffolds. *Tissue Eng.* **11**, 1589-1598, doi:10.1089/ten.2005.11.1589 (2005).

176 Williams, J. M. *et al.* Bone tissue engineering using polycaprolactone scaffolds fabricated via selective laser sintering. *Biomaterials* **26**, 4817-4827, doi:10.1016/j.biomaterials.2004.11.057 (2005).

177 Shor, L., Güçeri, S., Wen, X., Gandhi, M. & Sun, W. Fabrication of three-dimensional polycaprolactone/hydroxyapatite tissue scaffolds and osteoblast-scaffold interactions in vitro. *Biomaterials* **28**, 5291-5297, doi:10.1016/j.biomaterials.2007.08.018 (2007).

178 Zhang, R. & Ma, P. X. Poly(alpha-hydroxyl acids)/hydroxyapatite porous composites for bone-tissue engineering. I. Preparation and morphology. *J. Biomed. Mater. Res.* **44**, 446-455 (1999).

179 Cyster, L. A. *et al.* The influence of dispersant concentration on the pore morphology of hydroxyapatite ceramics for bone tissue engineering. *Biomaterials* **26**, 697-702, doi:10.1016/j.biomaterials.2004.03.017 (2005).

180 Roosa, S. M. M., Kemppainen, J. M., Moffitt, E. N., Krebsbach, P. H. & Hollister, S. J. The pore size of polycaprolactone scaffolds has limited influence on bone regeneration in an in vivo model. *J. Biomed. Mater. Res. A* **92**, 359-368, doi:10.1002/jbm.a.32381 (2010).

181 Yannas, I. V. Tissue regeneration by use of collagen-glycosaminoglycan copolymers. *Clin. Mater.* **9**, 179-187 (1992).

182 Heino, J. The collagen receptor integrins have distinct ligand recognition and signaling functions. *Matrix Biol.* **19**, 319-323 (2000).

183 Rezania, A. & Healy, K. E. Integrin subunits responsible for adhesion of human osteoblast-like cells to biomimetic peptide surfaces. *J. Orthop. Res.* **17**, 615-623, doi:10.1002/jor.1100170423 (1999).

184 Frohbergh, M. E. *et al.* Electrospun hydroxyapatite-containing chitosan nanofibers crosslinked with genipin for bone tissue engineering. *Biomaterials* **33**, 9167-9178, doi:10.1016/j.biomaterials.2012.09.009 (2012).

185 Boyan, B. D., Hummert, T. W., Dean, D. D. & Schwartz, Z. Role of material surfaces in regulating bone and cartilage cell response. *Biomaterials* **17**, 137-146 (1996).

186 Hwang, Y., Sangaj, N. & Varghese, S. Interconnected Macroporous Poly(Ethylene Glycol) Cryogels as a Cell Scaffold for Cartilage Tissue Engineering. *Tissue Engineering Part A* **16**, 3033-3041, doi:10.1089/ten.tea.2010.0045 (2010).

187 Kang, H., Shih, Y. R., Nakasaki, M., Kabra, H. & Varghese, S. Small molecule-driven direct conversion of human pluripotent stem cells into functional osteoblasts. *Sci Adv* **2**, e1600691, doi:10.1126/sciadv.1600691 (2016).

188 Heinonen, J. K. & Lahti, R. J. A new and convenient colorimetric determination of inorganic orthophosphate and its application to the assay of inorganic pyrophosphatase. *Anal Biochem* **113**, 313-317 (1981).

189 Shih, Y. R. *et al.* In vivo engineering of bone tissues with hematopoietic functions and mixed chimerism. *Proc Natl Acad Sci U S A* **114**, 5419-5424, doi:10.1073/pnas.1702576114 (2017).

190 Harley, B. A. C. *et al.* Microarchitecture of three-dimensional scaffolds influences cell migration behavior via junction interactions. *Biophys. J.* **95**, 4013-4024, doi:10.1529/biophysj.107.122598 (2008).

191 O'Brien, F. J., Harley, B. A., Yannas, I. V. & Gibson, L. J. The effect of pore size on cell adhesion in collagen-GAG scaffolds. *Biomaterials* **26**, 433-441, doi:10.1016/j.biomaterials.2004.02.052 (2005).

192 Kasten, P. *et al.* Porosity and pore size of beta-tricalcium phosphate scaffold can influence protein production and osteogenic differentiation of human mesenchymal stem cells: an in vitro and in vivo study. *Acta Biomater* **4**, 1904-1915, doi:10.1016/j.actbio.2008.05.017 (2008).

193 Akay, G., Birch, M. A. & Bokhari, M. A. Microcellular polyHIPE polymer supports osteoblast growth and bone formation in vitro. *Biomaterials* **25**, 3991-4000, doi:10.1016/j.biomaterials.2003.10.086 (2004).

194 Chiu, Y. C. *et al.* The role of pore size on vascularization and tissue remodeling in PEG hydrogels. *Biomaterials* **32**, 6045-6051, doi:10.1016/j.biomaterials.2011.04.066 (2011).

195 Druecke, D. *et al.* Neovascularization of poly(ether ester) block-copolymer scaffolds in vivo: long-term investigations using intravital fluorescent microscopy. *J Biomed Mater Res A* **68**, 10-18, doi:10.1002/jbm.a.20016 (2004).

196 Habibovic, P. *et al.* 3D microenvironment as essential element for osteoinduction by biomaterials. *Biomaterials* **26**, 3565-3575 (2005).

197 Yuan, H., van Blitterswijk, C. A., de Groot, K. & de Bruijn, J. D. A comparison of bone formation in biphasic calcium phosphate (BCP) and hydroxyapatite (HA) implanted in muscle and bone of dogs at different time periods. *Journal of Biomedical Materials Research Part A* **78A**, 139-147, doi:10.1002/jbm.a.30707 (2006).

198 Suzuki, A. *et al.* Enhanced Expression of the Inorganic Phosphate Transporter Pit-1 Is Involved in BMP-2–Induced Matrix Mineralization in Osteoblast-Like Cells. *Journal of Bone and Mineral Research* **21**, 674-683, doi:10.1359/jbmr.020603 (2006).

199 Beck Jr, G. R. Inorganic phosphate as a signaling molecule in osteoblast differentiation. *Journal of Cellular Biochemistry* **90**, 234-243, doi:10.1002/jcb.10622 (2003).

200 Wen, L. *et al.* L-type calcium channels play a crucial role in the proliferation and osteogenic differentiation of bone marrow mesenchymal stem cells. *Biochemical and Biophysical Research Communications* **424**, 439-445 (2012).

201 Zayzafoon, M. Calcium/calmodulin signaling controls osteoblast growth and differentiation. *Journal of Cellular Biochemistry* **97**, 56-70, doi:10.1002/jcb.20675 (2006).

202 Cowan, C. M. *et al.* NELL-1 increases pre-osteoblast mineralization using both phosphate transporter Pit1 and Pit2. *Biochemical and Biophysical Research Communications* **422**, 351-357 (2012).

203 Lacey, D. L. *et al.* Osteoprotegerin Ligand Modulates Murine Osteoclast Survival in Vitro and in Vivo. *The American Journal of Pathology* **157**, 435-448 (2000).

204 Udagawa, N. *et al.* Osteoblasts/stromal cells stimulate osteoclast activation through expression of osteoclast differentiation factor/RANKL but not macrophage colony-stimulating factor. *Bone* **25**, 517-523 (1999).

205 Patel, Z. S. *et al.* Dual delivery of an angiogenic and an osteogenic growth factor for bone regeneration in a critical size defect model. *Bone* **43**, 931-940 (2008).

206 Aronin, C. E. P. *et al.* FTY720 Promotes Local Microvascular Network Formation and Regeneration of Cranial Bone Defects. *Tissue Engineering Part A* **16**, 1801-1809, doi:10.1089/ten.tea.2009.0539 (2009).

207 Furumatsu, T. *et al.* Vascular Endothelial Growth Factor Principally Acts as the Main Angiogenic Factor in the Early Stage of Human Osteoblastogenesis. *The Journal of Biochemistry* **133**, 633-639, doi:10.1093/jb/mvg081 (2003).

208 Steinbrech, D. S. *et al.* Hypoxia Regulates VEGF Expression and Cellular Proliferation by Osteoblasts in Vitro. *Plastic and Reconstructive Surgery* **104** (1999).

209 Huang, W., Yang, S., Shao, J. & Li, Y. P. Signaling and transcriptional regulation in osteoblast commitment and differentiation. *Front Biosci* **12**, 3068-3092 (2007).

210 Wozney, J. M. The potential role of bone morphogenetic proteins in periodontal reconstruction. *J Periodontol* **66**, 506-510, doi:10.1902/jop.1995.66.6.506 (1995).

211 Beck, G. R. Inorganic phosphate as a signaling molecule in osteoblast differentiation. *Journal of Cellular Biochemistry* **90**, 234-243, doi:10.1002/jcb.10266 (2003).

212 Shih, Y.-R. *et al.* Synthetic bone mimetic matrix-mediated in situ bone tissue formation through host cell recruitment. *Acta Biomater.* **19**, 1-9, doi:10.1016/j.actbio.2015.03.017 (2015).

213 Gonzalez Diaz, E., Shih, Y., Nakasaki, M., Liu, M. & Varghese, S. Mineralized biomaterials mediated repair of bone defects through endogenous cells. *Tissue Eng Part A*, doi:10.1089/ten.TEA.2017.0297 (2018).

214 Nieminen, S., Nurmi, M. & Satokari, K. Healing of femoral neck fractures; influence of fracture reduction and age. *Ann Chir Gynaecol* **70**, 26-31 (1981).

215 Lu, C. *et al.* Effect of age on vascularization during fracture repair. *J Orthop Res* **26**, 1384-1389, doi:10.1002/jor.20667 (2008).

216 Desai, B. J., Meyer, M. H., Porter, S., Kellam, J. F. & Meyer, R. A., Jr. The effect of age on gene expression in adult and juvenile rats following femoral fracture. *J Orthop Trauma* **17**, 689-698 (2003).

217 Skak, S. V. & Jensen, T. T. Femoral shaft fracture in 265 children. Log-normal correlation with age of speed of healing. *Acta Orthop Scand* **59**, 704-707 (1988).

218 Zhou, S. *et al.* Age-related intrinsic changes in human bone-marrow-derived mesenchymal stem cells and their differentiation to osteoblasts. *Aging Cell* **7**, 335-343, doi:10.1111/j.1474-9726.2008.00377.x (2008).

219 D'Ippolito, G., Schiller, P. C., Ricordi, C., Roos, B. A. & Howard, G. A. Age-related osteogenic potential of mesenchymal stromal stem cells from human vertebral bone marrow. *J Bone Miner Res* **14**, 1115-1122, doi:10.1359/jbmr.1999.14.7.1115 (1999).

220 O'Driscoll, S. W., Saris, D. B., Ito, Y. & Fitzimmons, J. S. The chondrogenic potential of periosteum decreases with age. *J Orthop Res* **19**, 95-103, doi:10.1016/S0736-0266(00)00014-0 (2001).

221 Fan, W., Crawford R Fau - Xiao, Y. & Xiao, Y. Structural and cellular differences between metaphyseal and diaphyseal periosteum in different aged rats.

222 Meyer, R. A., Jr. *et al.* Young, adult, and old rats have similar changes in mRNA expression of many skeletal genes after fracture despite delayed healing with age. *J Orthop Res* **24**, 1933-1944, doi:10.1002/jor.20124 (2006).

223 Montjovent, M. O. *et al.* Repair of critical size defects in the rat cranium using ceramic-reinforced PLA scaffolds obtained by supercritical gas foaming. *J Biomed Mater Res A* **83a**, 41-51, doi:10.1002/jbm.a.31208 (2007).

224 Chen, Y. *et al.* Enhanced effect of beta-tricalcium phosphate phase on neovascularization of porous calcium phosphate ceramics: in vitro and in vivo evidence. *Acta Biomater* **11**, 435-448, doi:10.1016/j.actbio.2014.09.028 (2015).

225 Bolander, M. E. Regulation of fracture repair by growth factors. *Proc Soc Exp Biol Med* **200**, 165-170, doi:10.3181/00379727-200-43410a (1992).

226 Deckers, M. M. *et al.* Bone morphogenetic proteins stimulate angiogenesis through osteoblast-derived vascular endothelial growth factor A. *Endocrinology* **143**, 1545-1553, doi:10.1210/endo.143.4.8719 (2002).

227 Gerber, H. P. *et al.* VEGF couples hypertrophic cartilage remodeling, ossification and angiogenesis during endochondral bone formation. *Nat Med* **5**, 623-628, doi:10.1038/9467 (1999).

228 Matsuo, K. & Irie, N. Osteoclast–osteoblast communication. *Archives of biochemistry and biophysics* **473**, 201-209 (2008).

229 Sims, N. A. & Martin, T. J. Coupling Signals between the Osteoclast and Osteoblast: How are Messages Transmitted between These Temporary Visitors to the Bone Surface? *Front Endocrinol (Lausanne)* **6**, 41, doi:10.3389/fendo.2015.00041 (2015).

230 Teti, A. Mechanisms of osteoclast-dependent bone formation. *Bonekey Rep* **2**, 449, doi:10.1038/bonekey.2013.183 (2013).

231 Teitelbaum, S. L. Bone resorption by osteoclasts. *Science* **289**, 1504-1508 (2000).

232 Irie, N. *et al.* Bidirectional signaling through ephrinA2-EphA2 enhances osteoclastogenesis and suppresses osteoblastogenesis. *J Biol Chem* **284**, 14637-14644, doi:10.1074/jbc.M807598200 (2009).

233 Zhao, C. *et al.* Bidirectional ephrinB2-EphB4 signaling controls bone homeostasis. *Cell Metab* **4**, 111-121, doi:10.1016/j.cmet.2006.05.012 (2006).

234 Mundy, G. R. Local control of bone formation by osteoblasts. *Clin Orthop Relat Res*, 19-26 (1995).

235 Hayda, R. A., Brighton, C. T. & Esterhai, J. L., Jr. Pathophysiology of delayed healing. *Clin Orthop Relat Res*, S31-40 (1998).

236 Cummings, S. R. & Melton, L. J. Epidemiology and outcomes of osteoporotic fractures. *Lancet* **359**, 1761-1767, doi:10.1016/S0140-6736(02)08657-9 (2002).

237 Gruber, R. *et al.* Fracture healing in the elderly patient. *Exp Gerontol* **41**, 1080-1093, doi:10.1016/j.exger.2006.09.008 (2006).

238 Lu, C. *et al.* Cellular basis for age-related changes in fracture repair. *J Orthop Res* **23**, 1300-1307, doi:10.1016/j.orthres.2005.04.003.1100230610 (2005).

239 Sethe, S., Scutt, A. & Stolzing, A. Aging of mesenchymal stem cells. *Ageing Res Rev* **5**, 91-116, doi:10.1016/j.arr.2005.10.001 (2006).

240 Beane, O. S., Fonseca, V. C., Cooper, L. L., Koren, G. & Darling, E. M. Impact of aging on the regenerative properties of bone marrow-, muscle-, and adipose-derived mesenchymal stem/stromal cells. *PLoS One* **9**, e115963, doi:10.1371/journal.pone.0115963 (2014).

241 Asumda, F. Z. & Chase, P. B. Age-related changes in rat bone-marrow mesenchymal stem cell plasticity. *BMC Cell Biol* **12**, 44, doi:10.1186/1471-2121-12-44 (2011).

242 Baxter, M. A. *et al.* Study of telomere length reveals rapid aging of human marrow stromal cells following in vitro expansion. *Stem Cells* **22**, 675-682, doi:10.1634/stemcells.22-5-675 (2004).

243 Nishida, S., Endo, N., Yamagiwa, H., Tanizawa, T. & Takahashi, H. E. Number of osteoprogenitor cells in human bone marrow markedly decreases after skeletal maturation. *J Bone Miner Metab* **17**, 171-177 (1999).

244 Stenderup, K., Justesen, J., Clausen, C. & Kassem, M. Aging is associated with decreased maximal life span and accelerated senescence of bone marrow stromal cells. *Bone* **33**, 919-926 (2003).

245 Duscher, D. *et al.* Aging disrupts cell subpopulation dynamics and diminishes the function of mesenchymal stem cells. *Sci Rep* **4**, 7144, doi:10.1038/srep07144 (2014).

246 Rosen, C. J., Donahue, L. R. & Hunter, S. J. Insulin-like growth factors and bone: the osteoporosis connection. *Proc Soc Exp Biol Med* **206**, 83-102 (1994).

247 Boonen, S. *et al.* Down-regulation of the serum stimulatory components of the insulin-like growth factor (IGF) system (IGF-I, IGF-II, IGF binding protein [BP]-3, and IGFBP-5) in age-related (type II) femoral neck osteoporosis. *J Bone Miner Res* **14**, 2150-2158, doi:10.1359/jbmr.1999.14.12.2150 (1999).

248 Rivard, A. *et al.* Age-dependent impairment of angiogenesis. *Circulation* **99**, 111-120 (1999).

249 Ramasamy, S. K. *et al.* Blood flow controls bone vascular function and osteogenesis. *Nat Commun* **7**, 13601, doi:10.1038/ncomms13601 (2016).

250 Dutta, S. & Sengupta, P. Men and mice: Relating their ages. *Life Sci* **152**, 244-248, doi:10.1016/j.lfs.2015.10.025 (2016).

251 Choudhery, M. S. *et al.* Bone marrow derived mesenchymal stem cells from aged mice have reduced wound healing, angiogenesis, proliferation and anti-apoptosis capabilities. *Cell Biol Int* **36**, 747-753, doi:10.1042/CBI20110183 (2012).

252 Bruunsgaard, H. & Pedersen, B. K. Age-related inflammatory cytokines and disease. *Immunol Allergy Clin North Am* **23**, 15-39 (2003).

253 Gerstenfeld, L. C. *et al.* Impaired intramembranous bone formation during bone repair in the absence of tumor necrosis factor-alpha signaling. *Cells Tissues Organs* **169**, 285-294, doi:10.1159/000047893 (2001).

254 Ito, H. Chemokines in mesenchymal stem cell therapy for bone repair: a novel concept of recruiting mesenchymal stem cells and the possible cell sources. *Mod Rheumatol* **21**, 113-121, doi:10.1007/s10165-010-0357-8 (2011).

255 Spicer, P. P. *et al.* Evaluation of bone regeneration using the rat critical size calvarial defect. *Nat Protoc* **7**, 1918-1929, doi:10.1038/nprot.2012.113 (2012).

256 Laurencin, C., Khan, Y. & El-Amin, S. F. Bone graft substitutes. *Expert Review of Medical Devices* **3**, 49-57, doi:10.1586/17434440.3.1.49 (2006).

257 Gong, J. P., Katsuyama, Y., Kurokawa, T. & Osada, Y. Double-Network Hydrogels with Extremely High Mechanical Strength. *Advanced Materials* **15**, 1155-1158, doi:10.1002/adma.200304907 (2003).

258 Aouada, F. A., de Moura, M. R., Orts, W. J. & Mattoso, L. H. C. Preparation and Characterization of Novel Micro- and Nanocomposite Hydrogels Containing Cellulosic Fibrils. *Journal of Agricultural and Food Chemistry* **59**, 9433-9442, doi:10.1021/jf202347h (2011).

259 Miyazaki, S., Endo, H., Karino, T., Haraguchi, K. & Shibayama, M. Gelation Mechanism of Poly(N-isopropylacrylamide)−Clay Nanocomposite Gels. *Macromolecules* **40**, 4287-4295, doi:10.1021/ma070104v (2007).

260 Haraguchi, K. Nanocomposite hydrogels. *Current Opinion in Solid State and Materials Science* **11**, 47-54 (2007).

261 Liu, R. *et al.* Tough and highly stretchable graphene oxide/polyacrylamide nanocomposite hydrogels. *Journal of Materials Chemistry* **22**, 14160-14167, doi:10.1039/C2JM32541A (2012).

262 Gao, G., Du, G., Cheng, Y. & Fu, J. Tough nanocomposite double network hydrogels reinforced with clay nanorods through covalent bonding and reversible chain adsorption. *Journal of Materials Chemistry B* **2**, 1539-1548, doi:10.1039/C3TB21554G (2014).

263 Okumura, Y. & Ito, K. The Polyrotaxane Gel: A Topological Gel by Figure-of-Eight Cross-links. *Advanced Materials* **13**, 485-487, doi:10.1002/1521-4095(200104)13:7<485::Aid-adma485>3.0.Co;2-t (2001).

264 Fleury, G., Schlatter, G., Brochon, C. & Hadziioannou, G. From high molecular weight precursor polyrotaxanes to supramolecular sliding networks. The 'sliding gels'. *Polymer* **46**, 8494-8501 (2005).

265 Huang, T. *et al.* A Novel Hydrogel with High Mechanical Strength: A Macromolecular Microsphere Composite Hydrogel. *Advanced Materials* **19**, 1622-1626, doi:10.1002/adma.200602533 (2007).

266 Sakai, T. *et al.* Design and Fabrication of a High-Strength Hydrogel with Ideally Homogeneous Network Structure from Tetrahedron-like Macromonomers. *Macromolecules* **41**, 5379-5384, doi:10.1021/ma800476x (2008).

267 Bai, T. *et al.* Construction of an ultrahigh strength hydrogel with excellent fatigue resistance based on strong dipole–dipole interaction. *Soft Matter* **7**, 2825-2831, doi:10.1039/C0SM01108H (2011).

268 Li, W. *et al.* Hydrophobically associated hydrogels based on acrylamide and anionic surface active monomer with high mechanical strength. *Soft Matter* **8**, 5078-5086, doi:10.1039/C2SM07200A (2012).

269 Tuncaboylu, D. C., Argun, A., Sahin, M., Sari, M. & Okay, O. Structure optimization of self-healing hydrogels formed via hydrophobic interactions. *Polymer* **53**, 5513-5522 (2012).

270 Gong, J. P. Why are double network hydrogels so tough? *Soft Matter* **6**, 2583-2590, doi:10.1039/B924290B (2010).

271 Tominaga, T. *et al.* Thermodynamic Interactions in Double-Network Hydrogels. *The Journal of Physical Chemistry B* **112**, 3903-3909, doi:10.1021/jp710284e (2008).

272 Dobashi, T., Tomita, N., Maki, Y., Chang, C. P. & Yamamoto, T. An analysis of anisotropic gel forming process of chitosan. *Carbohydrate Polymers* **84**, 709-712, doi:10.1016/j.carbpol.2010.07.004 (2011).

273 Furusawa, K., Maki, Y., Yamamoto, T. & Dobashi, T. Rheological study of dialysis of concentrated DNA aqueous solution into multivalent cationic solution. *J. Jpn. Soc. Biorheol.* **21**, 132-138 (2007).

274 Na, G. C., Butz, L. J. & Carroll, R. J. Mechanism of in vitro collagen fibril assembly. Kinetic and morphological studies. *Journal of Biological Chemistry* **261**, 12290-12299 (1986).

275 Zhang, X. *et al.* The effects of different crossing-linking conditions of genipin on type I collagen scaffolds: an in vitro evaluation. *Cell and Tissue Banking* **15**, 531-541, doi:10.1007/s10561-014-9423-3 (2014).

276 Fukui, T. *et al.* Intra-articular administration of hyaluronic acid increases the volume of the hyaline cartilage regenerated in a large osteochondral defect by implantation of a double-network gel. *Journal of Materials Science: Materials in Medicine* **25**, 1173-1182, doi:10.1007/s10856-013-5139-3 (2014).

277 Nonoyama, T. *et al.* Double-Network Hydrogels Strongly Bondable to Bones by Spontaneous Osteogenesis Penetration. *Advanced Materials* **28**, 6740-6745, doi:10.1002/adma.201601030 (2016).

278 Du, Y., Yu, M., Chen, X., Ma, P. X. & Lei, B. Development of Biodegradable Poly(citrate)-Polyhedral Oligomeric Silsesquioxanes Hybrid Elastomers with High Mechanical Properties and Osteogenic Differentiation Activity. *ACS Applied Materials & Interfaces* **8**, 3079-3091, doi:10.1021/acsami.5b10378 (2016).

279 Zhang, Y. *et al.* In situ bone regeneration enabled by a biodegradable hybrid double-network hydrogel. *Biomaterials Science* **7**, 3266-3276, doi:10.1039/C9BM00561G (2019).

280 Liu, M., Nakasaki, M., Shih, Y. V. & Varghese, S. Effect of age on biomaterial-mediated in situ bone tissue regeneration. *Acta Biomater* **78**, 329-340, doi:10.1016/j.actbio.2018.06.035 (2018).

281 Vrana, N. E. *et al.* EDC/NHS cross-linked collagen foams as scaffolds for artificial corneal stroma. *J Biomater Sci Polym Ed* **18**, 1527-1545 (2007).

282 Sannino, A., Madaghiele, M. & Ambrosio, L. Biocompatibility and other properties of hydrogels in regenerative medicine. *Woodhead Publ Mater*, 114-135, doi:Doi 10.1533/9781845695477.1.114 (2009).

283 Temenoff, J. S., Athanasiou, K. A., LeBaron, R. G. & Mikos, A. G. Effect of poly(ethylene glycol) molecular weight on tensile and swelling properties of oligo(poly(ethylene glycol) fumarate) hydrogels for cartilage tissue engineering. *J Biomed Mater Res* **59**, 429-437, doi:10.1002/jbm.1259 (2002).

284 Bryant, S. J., Chowdhury, T. T., Lee, D. A., Bader, D. L. & Anseth, K. S. Crosslinking density influences chondrocyte metabolism in dynamically loaded photocrosslinked poly(ethylene glycol) hydrogels. *Ann Biomed Eng* **32**, 407-417, doi:10.1023/b:abme.0000017535.00602.ca (2004).

285 Schuh, E. *et al.* Chondrocyte redifferentiation in 3D: the effect of adhesion site density and substrate elasticity. *J Biomed Mater Res A* **100**, 38-47, doi:10.1002/jbm.a.33226 (2012).

286 Murat Sen, A. Y., Olgun Guvena. Determination of average molecular weight between cross-links (Mc) from
swelling behaviours of diprotic acid-containing hydrogels. *Polymer* **40**, 2969-2974, doi:10.1016/S0032-3861(98)00251-1 (1999).

287 Hou, Y. *et al.* Photo-cross-linked PDMSstar-PEG hydrogels: synthesis, characterization, and potential application for tissue engineering scaffolds. *Biomacromolecules* **11**, 648-656, doi:10.1021/bm9012293 (2010).

288 Bryant, S. J. & Anseth, K. S. Hydrogel properties influence ECM production by chondrocytes photoencapsulated in poly(ethylene glycol) hydrogels. *J Biomed Mater Res* **59**, 63-72, doi:10.1002/jbm.1217 (2002).

289 Lanasa, S. M., Hoffecker, I. T. & Bryant, S. J. Presence of pores and hydrogel composition influence tensile properties of scaffolds fabricated from well-defined sphere templates. *J Biomed Mater Res B Appl Biomater* **96**, 294-302, doi:10.1002/jbm.b.31765 (2011).

290 Flory, P. J. & Rehner, J., Jr. Statistical Mechanics of Cross-Linked Polymer Networks II. Swelling. *Journal of Chemical Physics* **11**, 521, doi:10.1063/1.1723792 (1943).

291 Peppas, N. A., Bures, P., Leobandung, W. & Ichikawa, H. Hydrogels in pharmaceutical formulations. *Eur J Pharm Biopharm* **50**, 27-46, doi:10.1016/s0939-6411(00)00090-4 (2000).

292 Hing, K. A. Bone repair in the twenty-first century: Biology, chemistry or engineering? *Philosophical Transactions of the Royal Society A: Mathematical, Physical and Engineering Sciences* **362**, 2821-2850, doi:10.1098/rsta.2004.1466 (2004).

293 Hing, K. A. Bioceramic Bone Graft Substitutes: Influence of Porosity and Chemistry. *International Journal of Applied Ceramic Technology* **2**, 184-199, doi:10.1111/j.1744-7402.2005.02020.x (2005).

294 Blokhuis, T. J. *et al.* Properties of Calcium Phosphate Ceramics in Relation to Their In Vivo Behavior. *Journal of Trauma and Acute Care Surgery* **48** (2000).

295 Kang, H., Zeng, Y. & Varghese, S. Functionally graded multilayer scaffolds for in vivo osteochondral tissue engineering. *Acta Biomater* **78**, 365-377, doi:10.1016/j.actbio.2018.07.039 (2018).

296 Kim, M. *et al.* Age-related alterations in mesenchymal stem cells related to shift in differentiation from osteogenic to adipogenic potential: Implication to age-associated bone diseases and defects. *Mechanisms of Ageing and Development* **133**, 215-225 (2012).

297 Singh, L. *et al.* Aging alters bone-fat reciprocity by shifting in vivo mesenchymal precursor cell fate towards an adipogenic lineage. *Bone* **85**, 29-36, doi:10.1016/j.bone.2016.01.014 (2016).

298 Clark, D. *et al.* Age-related changes to macrophages are detrimental to fracture healing in mice. *Aging Cell* **19**, e13112, doi:10.1111/acel.13112 (2020).

299 Vi, L. *et al.* Macrophage cells secrete factors including LRP1 that orchestrate the rejuvenation of bone repair in mice. *Nature Communications* **9**, 5191, doi:10.1038/s41467-018-07666-0 (2018).

300 Baht, G. S. *et al.* Exposure to a youthful circulation rejuvenates bone repair through modulation of β-catenin. *Nature Communications* **6**, 7131, doi:10.1038/ncomms8131 (2015).

301 Lee, J. S., Suarez-Gonzalez, D. & Murphy, W. L. Mineral Coatings for Temporally Controlled Delivery of Multiple Proteins. *Advanced Materials* **23**, 4279-4284, doi:10.1002/adma.201100060 (2011).

302 Urist, M. R. *et al.* Purification of bovine bone morphogenetic protein by hydroxyapatite chromatography. *Proc Natl Acad Sci U S A* **81**, 371-375 (1984).

303 Binkert, C. *et al.* Regulation of osteogenesis by fetuin. *J Biol Chem* **274**, 28514-28520, doi:10.1074/jbc.274.40.28514 (1999).

304 Price, P. A., Toroian, D. & Lim, J. E. Mineralization by inhibitor exclusion: the calcification of collagen with fetuin. *J Biol Chem* **284**, 17092-17101, doi:10.1074/jbc.M109.007013 (2009).

305 Alsberg, E. *et al.* Regulating Bone Formation via Controlled Scaffold Degradation. *Journal of Dental Research* **82**, 903-908, doi:10.1177/154405910308201111 (2003).

306 Bossard, M. J. *et al.* Proteolytic Activity of Human Osteoclast Cathepsin K: EXPRESSION, PURIFICATION, ACTIVATION, AND SUBSTRATE IDENTIFICATION. *Journal of Biological Chemistry* **271**, 12517-12524, doi:10.1074/jbc.271.21.12517 (1996).

307 Patterson, J. & Hubbell, J. A. Enhanced proteolytic degradation of molecularly engineered PEG hydrogels in response to MMP-1 and MMP-2. *Biomaterials* **31**, 7836-7845 (2010).

308 Varma, N. P., Garai, S. & Sinha, A. Synthesis of injectable and cohesive nano hydroxyapatite scaffolds. *Journal of Materials Science: Materials in Medicine* **23**, 913-919, doi:10.1007/s10856-012-4579-5 (2012).

309 Yu, T., Ye, J. & Wang, Y. Synthesis and property of a novel calcium phosphate cement. *Journal of Biomedical Materials Research Part B: Applied Biomaterials* **90B**, 745-751, doi:10.1002/jbm.b.31343 (2009).

310 Smeets, R. *et al.* In Vitro Study of Adhesive Polymethylmethacrylate Bone Cement Bonding to Cortical Bone in Maxillofacial Surgery. *Journal of Oral and Maxillofacial Surgery* **68**, 3028-3033 (2010).

311 Scott, E. A., Nichols, M. D., Kuntz-Willits, R. & Elbert, D. L. Modular scaffolds assembled around living cells using poly(ethylene glycol) microspheres with macroporation via a non-cytotoxic porogen. *Acta Biomaterialia* **6**, 29-38 (2010).

312 Griffin, D. R., Weaver, W. M., Scumpia, P. O., Di Carlo, D. & Segura, T. Accelerated wound healing by injectable microporous gel scaffolds assembled from annealed building blocks. *Nature materials* **14**, 737-744, doi:10.1038/nmat4294 (2015).

313 Caldwell, A. S., Campbell, G. T., Shekiro, K. M. T. & Anseth, K. S. Clickable Microgel Scaffolds as Platforms for 3D Cell Encapsulation. *Advanced Healthcare Materials* **6**, 1700254, doi:10.1002/adhm.201700254 (2017).

Biography

Mengqian Liu received her Bachelor of Science in Materials Science and Engineering and Bioengineering from the University of California Berkeley in December of 2013. Following her undergraduate work, Mengqian continued her study in University of California San Diego in pursuing a Ph.D. in Materials Science and Engineering. After completing of her Master of Science, Mengqian began her Ph.D. study in Mechanical Engineering and Materials Science at Duke University in September of 2017. Mengqian has published and (co-)authored several articles and book chapters; a list of publications and awards is presented below.

- Effects of Age on Biomaterial-Mediated *In Situ* Bone Tissue Regeneration. *Acta Biomaterialia*
- Guided Cell Behavior in Regenerative Engineering. *Regenerative Engineering*
- Dysregulation of Ectonucleotidase-Mediated Extracellular Adenosine during Postmenopausal Bone Loss. *Science Advances*
- Mineralized Biomaterials Promote Repair of Critical-Sized Bone Defects through Endogenous Cells. *Tissue Engineering Part A*
- Continuous Flow Rail-and Trap Microfluidic Processors for Autonomous Bead-Based Mixing and Visualization", *Proceedings of 16th International Conference on Miniaturized Systems or Chemistry and Life Sciences*